

**POLARIZATION-ENABLED MULTIDIMENSIONAL
OPTICAL MICROSCOPY**

by

Changqin Ding

A Dissertation

Submitted to the Faculty of Purdue University

In Partial Fulfillment of the Requirements for the degree of

Doctor of Philosophy



Department of Chemistry

West Lafayette, Indiana

May 2019

THE PURDUE UNIVERSITY GRADUATE SCHOOL
STATEMENT OF COMMITTEE APPROVAL

Dr. Garth J. Simpson, Chair
Department of Chemistry

Dr. Peter T. Kissinger
Department of Chemistry

Dr. Chengde Mao
Department of Chemistry

Dr. Robert G. Cooks
Department of Chemistry

Approved by:

Dr. Christine A. Hrycyna
Head of the Graduate Program

To those who care.

Don't panic.

ACKNOWLEDGMENTS

I am grateful to a vast number of people who have helped me get to this point in my life. I first need to thank my parents, Hongxin Ding and Zhenhua Li, as well as my twin sister Changyu for their endless understanding, comfort, and support for me to try all the things I want. You are always the solid back shields for me.

I want to thank all the advisors in my academic path. Thanks to Dr. Liyan Fan for introducing me into the world of science with great care and patience. Thanks to Dr. Yang Tian for providing me with a great platform and the trust so that I can pursue different directions in the research. A special thanks to Dr. Garth Simpson for being my advisor at Purdue. You are always nice and patient with me. Your compassion in science was a driving force that I can follow. I really appreciate all your challenges, questions, encourage and supports.

My time at Purdue would not be the best without all the group members in Simpson Lab. Great thanks to Fengyuan (Max) Deng for picking me up into the group, working closely with me on most of the research projects, and babysitting me during all the time. I am so honored to have a friend like you. Thanks to Justin Newman, Ximeng Dow, Paul Schmitt, Janny Dinh, and Nikki Scarborough for teaching me the basics of nonlinear optics. I also want to thank Ziyi Cao, Hilary Florian, Andreas Geiger, Scott Griffin, Chen Li, Minghe Li, Youlin Liu, Cody Martin, Jiayue Rong, Sreya Sarkar, Alex Sherman, Casey Smith, Zhengtian Song, Nita Takanti, James Ulcickas, and Shijie Zhang for all the cookies, cakes, marvelous board paintings, and endless discussions on diverse topics. I appreciate the friendly and interesting environment you have built in the lab.

I also want to thank all my fellows at or out of Purdue. Thanks to Aaron Chen, Fan Pu, Pei Su, and Zhuo'er Xie for all the dumpling festivals we have celebrated together. Thanks to Zhe Li, Longfei Liu, Nan Wang, Siyu Wu, Yun Yang, Feifei Zhao, and Yiyang Zhou for all the Saturday game nights we have shared. Thanks to Andy Huang, Mohammad Sasar, Joshua Yu and all my teammates and coaches at Purdue Latin and Ballroom dance team for all the happy time we have gone through on or off the floor. Thanks to Yujie Chen and Pu Su for all your support, trust and comfort. Last and maybe not least, I want to thank all the cats for their companion: Naonao, Jingjing, Qiuqiu, Fanny, Kaya, and Captain. Cats rock.

TABLE OF CONTENTS

LIST OF TABLES	8
LIST OF FIGURES	9
LIST OF ABBREVIATIONS.....	11
ABSTRACT.....	13
CHAPTER 1. INTRODUCTION.....	14
1.1 Polarization dependent nonlinear optical (NLO) microscopy	14
1.2 Jones and Stokes descriptions of polarization	15
1.3 Quantitative phase contrast imaging.....	17
1.4 High throughput multidimensional and multiplexing imaging methods	18
1.5 Dissertation overview	19
1.6 References.....	20
CHAPTER 2. SECOND HARMONIC GENERATION OF UNPOLARIZED LIGHT	26
2.1 Introduction.....	26
2.2 Theoretical foundation	28
2.3 Experimental Methods	38
2.4 Results and discussion	39
2.5 Conclusion	44
2.6 References.....	44
CHAPTER 3. LOCAL-FRAME TENSOR ELEMENTS RECOVERY FOR POLARIZATION DEPENDENT ANALYSIS OF THICK TISSUES.....	47
3.1 Introduction.....	47
3.2 Theoretical foundation	48
3.3 Methods.....	49
3.4 Results.....	51
3.5 Conclusion	54
3.6 References.....	54
CHAPTER 4. SPATIAL ENCODED POLARIZATION DEPENDENT NONLINEAR OPTICAL ANALYSIS.....	56
4.1 Introduction.....	56

4.2	Experimental Methods	58
4.3	Mathematical Foundation	60
4.4	Result and discussion	62
4.5	Conclusion	67
4.6	References.....	68
CHAPTER 5. AXIALLY-OFFSET DIFFERENTIAL INTERFERENCE CONTRAST MICROSCOPY VIA POLARIZATION WAVEFRONT SHAPING.....		70
5.1	Introduction.....	70
5.2	Methods.....	72
5.3	Results.....	79
5.4	Discussion	84
5.5	Conclusion	87
5.6	References.....	87
CHAPTER 6. ADIC CORRELATION SPECTROSCOPY (ADIC-CS).....		90
6.1	Introduction.....	90
6.2	Method	92
6.3	Result and discussion	93
6.4	Conclusion	96
6.5	References.....	97
CHAPTER 7. RAPID VOLUMETRIC IMAGING METHODS		98
7.1	Introduction.....	98
7.2	Theoretical framework.....	99
7.3	Discussion	105
7.4	Conclusion	105
7.5	References.....	106
CHAPTER 8. SPATIAL/SPECTRAL MULTIPLEXING FOR VIDEO-RATE HYPERSPPECTRAL IMAGING.....		107
8.1	Introduction.....	107
8.2	Methods.....	109
8.3	Results and discussion	114
8.4	Conclusion	118

8.5 References.....	119
VITA.....	121
PUBLICATIONS.....	122

LIST OF TABLES

Table 1.1 Jones vectors and Stokes vectors for common optical polarizations.....	16
--	----

LIST OF FIGURES

Figure 2.1 Combination of tensor elements by re-ordering the 0 and 1 entries in the binary number.	31
Figure 2.2 SHG transmittance microscope capable of delivering both a purely polarized and a depolarized fundamental beam.	39
Figure 2.3 Polarization dependent SHG measurements with pure polarized and/or depolarized light with theoretical predictions..	40
Figure 2.4 Orientation images of the azimuthal angle for a single FoV of mouse tail section from the pixel-by-pixel nonlinear fit analysis and <i>OrientationJ</i>	42
Figure 2.5 The laboratory-frame ratio ρ and polar tilt angle a single FoV of mouse tail section from the per-pixel fit analysis..	43
Figure 3.1 Schematic of the polarization-dependent components in the SHG microscope.....	50
Figure 3.2 Flow diagram for tensor recovery in partially depolarizing media.	52
Figure 3.3 The DoP measured in transmission through a $\sim 40 \mu\text{m}$ thick section of rat tail tendon..	53
Figure 3.4 Histogram of the tensor element ratios recovered for SHG imaging of collagen with partially depolarized incident light.	53
Figure 4.1 Schematic for instrumentation of the spatial encoded polarization dependent nonlinear optical analysis.....	59
Figure 4.2 Illustration of the data acquisition and analysis process of the bright-field and SHG images of z-cut quartz.	63
Figure 4.3 Direct linear fit for polynomial coefficients recovery from SHG measurements of z-cut quartz on the reshaped data set..	64
Figure 4.4 Iteration fit for polynomial coefficients recovery from SHG measurements of z-cut quartz on the reshaped data set..	65
Figure 4.5 Translation-based spatially encoded polarization dependent NLO imaging for collagen tissue.....	66
Figure 4.6 The orientation angle and tensor ratio recovered from collagen tissue on the base of each pixel..	67
Figure 5.1 The principles of axial-offset foci generation and design of μRA	74
Figure 5.2. Experiment set-up for QPI with a 10x objective to recover both bright field images and QP images. Blue circled optics: add-in parts for LIA detection.	76
Figure 5.3 Measured point spread functions in the x-z plane with (A) and without (B) the μRA installed in the beam path.	80
Figure 5.4 Several unprocessed images with different HWP rotation angles.....	81

Figure 5.5 Transmittance image and QP images recovered with half wave rotation measurement of a single FoV of mouse tail section.....	82
Figure 5.6 Raw images and recovered transmittance and quantitative phase image from LIA detection for a single FoV of mouse tail section.....	83
Figure 5.7 Transmittance and quantitative phase contrast images recovered from HWP rotation and LIA detection strategies of a single FoV of mouse tail section..	84
Figure 5.8 Quantitative phase contrast images of the same FoV of 8 μm silica beads recovered from both HWP rotation and LIA detection strategies..	86
Figure 6.1 The working principle of ADIC-CS.....	91
Figure 6.2 Instrumentation for ADIC-CS with a 10x objective. Signals were collected in cross polarization states of the linearly polarized incident light with a fast digitizer for digital lock-in analysis.	93
Figure 6.3 Mathematical framework simulation of ADIC-CS.	94
Figure 6.4 Baseline shift induced from the glass slide..	95
Figure 6.5 Intensity and phase change traces as a time of function after digital lock-in analysis..	96
Figure 7.1 Working principles of the rapid multifocal imaging using wavefront shaping.....	100
Figure 7.2 The power distribution and separation distance among the multiple focal planes when using different illumination wavelengths.....	102
Figure 7.3 Schematic for volumetric images stacks recovered from the measured data.	105
Figure 8.1 Instrument schematic of the hyperspectral imaging system.....	110
Figure 8.2 Schematic of the spatial-spectral multiplexing.....	111
Figure 8.3 Spectral window calibration with SHG from a doubling crystal and spectrum recovery.	112
Figure 8.4 Flowchart for the iterative classification algorithm.....	114
Figure 8.5 Fluorescence images and classification results of fluorescent dye droplets with the recovered spectrum..	115
Figure 8.6 Dye mixture with three fluorophores: fluorescein (green) in water, coumarin 6 (blue) and eFluor TM 450 (violet) in chloroform separately..	117
Figure 8.7 Two-photon fluorescence image of gene coded <i>C. elegans</i> analyzed without knowing the emission spectra of the fluorophores as a priori..	118

LIST OF ABBREVIATIONS

ADIC	Axially-offset differential interference contrast
ADIC-CS	Axially-offset differential interference contrast correlation spectroscopy
AIDPC	Asymmetric illumination-based differential phase contrast
API	Active pharmaceutical ingredients
BF	Bright field
CARS	Coherent anti-stokes Raman scattering
CASSI	Coded aperture snapshot spectral imager
DCM	Dichroic mirror
DIC	Differential interference contrast
DLS	Dynamic light scattering
DoP	Degree of polarization
EOM	Electro-optic modulator
FoV	Field of view
GTP	Glan-Taylor polarizer
HWP	half wave plate
IMS	Image mapping spectrometers
LCP	Left circular polarized
LIA	Lock-in amplified
LoD	Limit of detection
MLE	Maximum likelihood estimate
NA	Numerical aperture
NDSSM	Non-de-scan spatial/spectral multiplexing
NIC	Nomarski interference contrast
NLO	Nonlinear optical
PCB	printed circuit board
PD	Photodiode
PEM	Photoelastic modulator
PMT	Photomultiplier tube

QP	Quantitative phase
QPI	Quantitative phase imaging
QWLSI	Quadriwave lateral shearing interferometry
QWP	Quarter waveplate
RCP	Right circular polarized
RMS	Root mean square
SFG	Sum-frequency generation
SHG	Second harmonic generation
SLIM	Spatial light interference microscopy
SRS	Stimulated Raman scattering
SSE	Sum of squared errors of prediction
TPEF	Two-photon excited fluorescence
WP	Wave plate
μ RA	Microretarder array

ABSTRACT

Author: Ding, Changqin. PhD

Institution: Purdue University

Degree Received: May 2019

Title: Polarization-Enabled Multidimensional Optical Microscopy

Committee Chair: Garth J. Simpson

Polarization-dependence provides a unique handle for extending the dimensionality of optical microscopy, with particular benefits in nonlinear optical imaging. Polarization-dependent second order nonlinear optical processes such as second harmonic generation (SHG) provide rich qualitative and quantitative information on local molecular orientation distribution. By bridging Mueller and Jones tensor, a theoretical framework was introduced to experimentally extend the application of polarization-dependent SHG microscopy measurements toward *in vivo* imaging, in which partial polarization or depolarization of the beam can complicate polarization analysis. In addition, polarization wavefront shaping was demonstrated to enable a new quantitative phase contrast imaging strategy for thin transparent samples. The axially-offset differential interference contrast microscopy (ADIC) was achieved as a combination of classic Zernike phase contrast and Nomarski differential interference contrast (DIC) methods. The fundamentally unique manner of this strategy also inspired rapid volumetric analysis in time dimension that is accessible for most existing microscopy systems. Finally, the dimensionality of high speed two-photon fluorescence imaging was extended to the spectral domain by spatial/spectral multiplexing, enabling beam scanning two photon fluorescence microscopy with 17 frames per second rate and over 2000 effective spectral data points.

CHAPTER 1. INTRODUCTION

1.1 Polarization dependent nonlinear optical (NLO) microscopy

Nonlinear optics describes the behavior of light in nonlinear optically active media in which the polarizability of the material responds non-linearly to the electric field of the light. The study of nonlinear optics prospered after the observation of second harmonic generation (SHG) by Peter Franken and his co-workers at the University of Michigan in 1961.¹ Since then, a host of nonlinear optical phenomena has been explored, including two-photon excited fluorescence (TPEF)²⁻⁶, sum-frequency generation (SFG)⁷⁻⁹, coherent anti-stokes Raman scattering (CARS)¹⁰⁻¹², stimulated Raman scattering (SRS)¹³⁻¹⁵, etc. Nonlinear effects from the material can be categorized into parametric and non-parametric effects.¹⁶ The parametric non-linearity means that in the interaction between light and nonlinear material, the quantum state of the nonlinear material is not changed by the interaction with the optical field. As a consequence, the nonlinear optics process is instantaneous, making phase-matching important and enhancing polarization-dependent effects since the energy and momentum are conserved in the optical field during the interaction.

As one of the most common NLO processes, SHG classically arises from the interaction between an intense optical field (i.e. in the focus of a laser beam) and an anharmonic potential energy surface of electrons.^{16, 17} In the SHG process, a new electric field with exactly twice the frequency of the incident fields is generated from the interaction between the incident light and the material. Coherent SHG is selective for noncentrosymmetric media and sensitive to the polarization states of the incident light. Polarization dependent SHG measurements can directly access the hyperpolarizability tensor that describes the second order response of the material to the applied electric field, with up to 18 unique elements in the Cartesian reference frame.¹⁸ Polarization dependent SHG microscopy has been widely used for structural characterization of myosin, collagen¹⁹⁻²⁴, protein crystals²⁵⁻³⁰, and crystalline active pharmaceutical ingredients (API)³¹⁻³⁶. However, as the imaging depth is increased in biological media analysis, interpretation of polarization dependent SHG measurements is complicated due to native turbidity associated with the myriad of solubilized small particles and birefringent protein.³⁷ Since *in vivo* imaging

typically requires passing the beam through tissue to access the focal plane, the structural information recovered by polarization analysis is often lost in live-animal SHG imaging.

1.2 Jones and Stokes descriptions of polarization

To describe the polarization states in nonlinear optical processes, Clark Jones and Henry Hurwitz published a series of papers to establish “a new calculus for the treatment of optical systems”³⁸⁻⁴¹ in the 1940s, now known as the Jones calculus framework. The Jones framework treats the polarization state and intensity of an optical beam with linear algebra notation as a prelude to extending generalization for tensor analysis. By projecting the electric field onto two orthogonal axes, any polarized beam traveling in the positive z -direction can be presented by a two-element Jones vector of the form shown in Eq. (1.1). Thus, the Jones vector describes the amplitude and phase of the electric field in both the x and y directions. The total intensity of the light can be calculated as the squares of the absolute values of the two components of the Jones vector. The Jones calculus addresses the effects of individual polarizing and attenuating optics with simple multiplication of Jones matrices to propagate polarization through complex optical paths.

$$\vec{e} = \begin{bmatrix} e_x \\ e_y \end{bmatrix} = \begin{bmatrix} E_{0x} e^{i\phi_x} \\ E_{0y} e^{i\phi_y} \end{bmatrix} \quad (1.1)$$

Jones vector and Jones matrices provide broad foundation of polarization dependent nonlinear optics description with the application of the nonlinear optical susceptibility, Jones tensor $\chi^{(n)}$ ^{18, 31, 42, 43}. However, Jones framework is limited in describing partially depolarizing reflectivity/transmissivity.

In these cases, Stokes vectors and Mueller tensors provide an alternate linear algebra framework to describe nonlinear optical interactions in assemblies that involve partially or totally polarized fields.^{18, 43-45} As the basic unit of polarization description in the Stokes/Mueller framework, the Stokes vector presents different combinations of intensities recorded for different polarization components of a light beam, as shown in Eq. (1.2). I_H , I_V , $I_{\pm 45^\circ}$, I_R , and I_L are the intensities recorded for horizontally, vertically, $\pm 45^\circ$ linearly, right and left circularly polarized components, respectively.

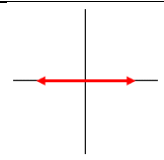
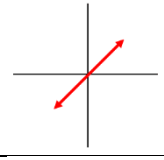
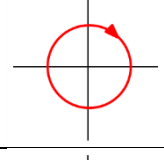
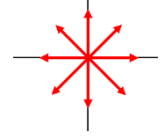
$$\bar{s} = \begin{bmatrix} I_H + I_V \\ I_H - I_V \\ I_{+45^\circ} - I_{-45^\circ} \\ I_R - I_L \end{bmatrix} \quad (1.2)$$

The comparison between Jones vectors and Stokes vectors for several common polarization states are presented in

Table 1.1. Similar with Jones matrices, Mueller matrices are also introduced to describe polarization transfer due to the optics or samples in the beam path. In the absence of any depolarizing interaction, a transformation matrix A connects the Stokes vector with Jones vectors in Eq. (1.3).^{18, 43}

$$\bar{s} = \begin{bmatrix} 1 & 0 & 0 & 1 \\ 1 & 0 & 0 & -1 \\ 0 & 1 & -1 & 0 \\ 0 & i & -i & 0 \end{bmatrix} \cdot \begin{bmatrix} \bar{e}_x^* \bar{e}_x \\ \bar{e}_x^* \bar{e}_y \\ \bar{e}_y^* \bar{e}_x \\ \bar{e}_y^* \bar{e}_y \end{bmatrix} = A \cdot (\bar{e}^* \otimes \bar{e}) \quad (1.3)$$

Table 1.1 Jones vectors and Stokes vectors for common optical polarizations

Polarization	Jones vector	Stokes vector	Illustration
Linearly polarized: horizontal	$[1 \ 0]^T$	$I_0 [1 \ 1 \ 0 \ 0]^T$	
Linearly polarized: +45°	$\frac{1}{\sqrt{2}} [1 \ 1]^T$	$I_0 [1 \ 0 \ 1 \ 0]^T$	
Circular polarized: right	$\frac{1}{\sqrt{2}} [1 \ i]^T$	$I_0 [1 \ 0 \ 0 \ 1]^T$	
Depolarized	Not applied	$I_0 [1 \ 0 \ 0 \ 0]^T$	

In this dissertation, the connection between Jones calculus and Mueller/Stocks framework will be discussed for polarization dependent SHG analysis to extract hyperpolarizability tensor elements from collagen tissues with partial or depolarized light in *CHAPTER 2* and *CHAPTER 3*.

1.3 Quantitative phase contrast imaging

Different with thick or turbid tissue samples, specimens such as living cells, unstained tissues, protein crystals, nanomaterials, and membranes pose challenges to intrinsic contrast imaging when using transmission/back-scattering optical microscopy due to the weak absorption and scattering. Phase-contrast microscopy is a technique that utilizes the phase shifts in light passing through a transparent specimen to produce contrast in the image.⁴⁶⁻⁴⁹ As one of the few label-free methods available to quantify cellular structure and components, phase-contrast microscopy has been actively used in biological research including observing neurons in unstained tissue slices⁵⁰, kinesin-driven movement studies⁵¹, microtubule-related motility visualization in cells⁵², etc.

There are two common ways to increase image contrast from subtle phase shifts when using an intensity detector: i) Zernike phase contrast uses spatial interference between light patterned with annular rings to produce intensity contrast, highlighting phase differences between relatively tightly focused (sample) and relatively gently focused (background) beams;^{46, 47, 53} ii) differential interference contrast (DIC), or Nomarski interference contrast (NIC) measures the interference of two separated orthogonally polarized mutually coherent parts from one polarized light source at the recombination.^{48, 50, 52, 54, 55} Without the halo-effects existing in Zernike phase contrast method, DIC microscopy suffers orientation-dependent “side lighting” artifacts since the two orthogonal polarized components are in the same sample plane.

To achieve artifact-free quantitative phase imaging (QPI), Gabor has suggested using interferometry to split and recombine the beam with an angle, so that an interferogram is recorded to quantitatively recover the complex optical field.⁵⁶⁻⁵⁹ Based on similar principles, many interferometric QPI approaches were developed recently, including asymmetric illumination-based differential phase contrast (AIDPC) microscopy⁶⁰⁻⁶², quadriwave lateral shearing interferometry (QWLSI)⁶³, τ interferometry⁶⁴, spatial light interference microscopy (SLIM)⁶⁵, Fourier ptychography⁶⁶, etc. These methods have low limits of detection for phase changes to detect the phospholipid bilayer, cells or other objects with a dimension below the

diffraction limit⁶⁷. These methods often required dedicated purpose-built instruments with sparse sample image required for interferogram analysis. However, there is no doubt that the development of new type of QPI methods capable of per-pixel analysis compatible with retrofitting into available microscope platform will promote the growth of non-invasive live cell imaging and automated cell culture analysis.

1.4 High throughput multidimensional and multiplexing imaging methods

Optical imaging systems have been widely used in biological structural analysis and *in vivo* pharmaceutical analysis. Different dimensions have been explored in optical imaging for improving the information content from the samples, such as video rate imaging to provide time resolution (x, y, t), volume imaging for z-axis resolution (x, y, z), and spectral imaging for spectroscopic analysis in cells or tissue with wavelength dimension (x, y, λ). Multiple dimensions can be combined, with up to five different dimensions (x, y, z, t, λ) explored in this thesis work.

High frame rate of time-dependent imaging reduces the 1/f noise and motion blur in dynamic imaging. To improve the time resolution, the beam scanning system and high-speed camera are available as replacements for the sample scanning system. Meanwhile, developments in beam scanning mode and image reconstruction modification provide higher video rate imaging methods, such as Lissajous trajectory beam scanning microscopy. For volumetric imaging, the most common approach for three-dimension imaging is depth sampling (z-scanning), in which images are acquired in sequence at different z positions. These methods require movement of the objective or the sample, resulting high 1/f noise and motion blur. Recently, light sheet microscopy and varifocal lens for multi-focus imaging were developed for 3D imaging.^{68, 69} Light sheet microscopy enabled high speed and high-resolution volumetric fluorescence imaging but was limited in turbid media such as biological tissues.⁷⁰ Other fast multi-focus imaging methods were developed, including electrically-controllable liquid-crystal varifocal lens^{69, 71-73} and acoustically driven optofluidic lens^{74, 75}. However, these methods require extra electronical control for the liquid-crystal micro lenses, complicating the manufactory of an existing microscope system.

In multiphoton excited fluorescence imaging of biological systems, the spectral dimension or wavelength dimension provides plenty of information, enabling multi-labeled analysis for

studies of biological processes and clinical diagnoses⁷⁶⁻⁷⁹. Similar with volumetric imaging method, traditional hyperspectral imaging techniques need long requiring time to populate the 3 dimensional data structure (x, y, λ) through spatial scanning or spectral scanning. Several snapshot hyperspectral imaging systems were developed as alternatives to the traditional time-consuming spectral imaging techniques, such as coded aperture snapshot spectral imager (CASSI)⁸⁰, image mapping spectrometers (IMS)⁸¹. However, most of these snapshot methods are not directly compatible with conventional multi-photon excited fluorescence microscopy with trade-offs between spatial and spectral resolution, because both sets of information were encoded on the same fixed number of imaging channels. In this case, a strategy for high speed spectral imaging accessible with existing fluorescence microscope is higher required.

1.5 Dissertation overview

The work described in this dissertation includes instrumentation and methods development for polarization-enabled optical microscopy to extract extended information from different dimensions of the sample. Two types of polarization dependent strategies were used for this purpose: i) polarization dependent SHG measurements were developed to extract microscopic structures from the samples with or without polarization dependent incident light; ii) polarization wavefront shaping was shown as a new type of quantitative phase contrast imaging system with potential applications in heterodyne detected nonlinear optical imaging, particle analysis, and rapid volumetric imaging. Additionally, a hyperspectral two-photon fluorescence imaging system was demonstrated through spatial-spectral multiplexing as a video-rate four-dimensional (x, y, t, λ) imaging method.

In *CHAPTER 2*, a theoretical framework connecting Mueller and Jones frames is introduced and experimentally proven to extract local structure information from the samples with partially or fully depolarized light. The prediction of this framework agreed well with the experimental observations for z-cut quartz as a model system. Microscopic structures of collagen tissue including polar and azimuthal orientation were recovered on a per-pixel basis with a depolarized source. This framework has been used for local-frame tensor element imaging for thick, partially depolarizing tissues, as discussed in *CHAPTER 3*.

In *CHAPTER 4*, spatially encoded polarization dependent SHG measurement was achieved with a patterned microretarder array for local tensor imaging of z-cut quartz and collagenous

tissue. With the combination of ‘snapshot’ and sample translation approaches, these methods showed good agreement with traditional polarization dependent measurements, providing an alternate approach for polarization SHG analysis with minimal modifications on current beam scanning nonlinear optical systems.

As described in *CHAPTER 5*, axially-offset differential interference contrast microscopy (ADIC) was demonstrated via polarization wavefront shaping as a new strategy for quantitative phase contrast imaging. This strategy combined classic Zernike phase contrast and Nomarski differential interference contrast (DIC) methods, with its fundamentally unique manner providing subsequent opportunities that are inherently inaccessible from most recent QPI methods. ADIC correlation spectroscopy has been developed based on this quantitative phase retrieval method for drifting particle analysis of size distribution and refractive index recovery, as detailed in *CHAPTER 6*.

In *CHAPTER 7*, the possibility of using polarization wavefront shaping method to achieve rapid volumetric imaging from multiple focus planes is presented theoretically. With a designed wavefront shaping optics inserted in the beam path, two or three focal planes with different polarization states can be generated simultaneously with the same objective based on the incident light wavelength. Fast modulation of the incident light polarization states is predicted to result in the intensity distribution among these separated focal planes, leading to the potential for rapid volumetric imaging after demultiplexing.

In *CHAPTER 8*, a high speed spatial/spectral multiplexing hyperspectral two-photon fluorescence imaging system is introduced with up to 17 frames per second rate and over 2000 effective spectral channels in a 200 nm wavelength window. An iterative algorithm was developed for spectral retrieval and component classification for fluorophores with similar emission spectra, which were difficult to discriminate by the conventional filter-based fluorescence microscopy.

1.6 References

1. Franken, e. P.; Hill, A. E.; Peters, C. e.; Weinreich, G., Generation of optical harmonics. *Physical Review Letters* **1961**, 7 (4), 118.
2. Kaiser, W.; Garrett, C. G. B., Two-Photon Excitation in Ca²⁺. *Physical Review Letters* **1961**, 7 (6), 229-231.

3. Denk, W.; Strickler, J. H.; Webb, W. W., Two-photon laser scanning fluorescence microscopy. *Science* **1990**, *248* (4951), 73-76.
4. Helmchen, F.; Denk, W., Deep tissue two-photon microscopy. *Nat Methods* **2005**, *2* (12), 932-40.
5. Larson, D. R.; Zipfel, W. R.; Williams, R. M.; Clark, S. W.; Bruchez, M. P.; Wise, F. W.; Webb, W. W., Water-soluble quantum dots for multiphoton fluorescence imaging in vivo. *Science* **2003**, *300* (5624), 1434-1436.
6. Svoboda, K.; Yasuda, R., Principles of two-photon excitation microscopy and its applications to neuroscience. *Neuron* **2006**, *50* (6), 823-839.
7. Shen, Y. J. N., Surface properties probed by second-harmonic and sum-frequency generation. **1989**, *337* (6207), 519.
8. Zhu, X.; Suhr, H.; Shen, Y. J. P. R. B., Surface vibrational spectroscopy by infrared-visible sum frequency generation. **1987**, *35* (6), 3047.
9. Morita, A., *Theory of Sum Frequency Generation Spectroscopy*. Springer: 2018; Vol. 97.
10. Begley, R.; Harvey, A.; Byer, R. L. J. A. P. L., Coherent anti - Stokes Raman spectroscopy. **1974**, *25* (7), 387-390.
11. Duncan, M. D.; Reintjes, J.; Manuccia, T. J. O. I., Scanning coherent anti-Stokes Raman microscope. **1982**, *7* (8), 350-352.
12. Tolles, W. M.; Nibler, J.; McDonald, J.; Harvey, A. J. A. S., A review of the theory and application of coherent anti-Stokes Raman spectroscopy (CARS). **1977**, *31* (4), 253-271.
13. Hellwarth, R. W. J. P. R., Theory of stimulated Raman scattering. **1963**, *130* (5), 1850.
14. Eckhardt, G.; Hellwarth, R.; McClung, F.; Schwarz, S.; Weiner, D.; Woodbury, E. J. P. R. L., Stimulated Raman scattering from organic liquids. **1962**, *9* (11), 455.
15. Maier, M.; Kaiser, W.; Giordmaine, J. J. P. R., Backward stimulated Raman scattering. **1969**, *177* (2), 580.
16. Boyd, R. J. S. D., Calif, *Nonlinear Optics Academic*. **2003**, *19922*, 126-143.
17. Brown, F.; Matsuoka, M. J. P. R., Effect of adsorbed surface layers on second-harmonic light from silver. **1969**, *185* (3), 985.
18. Simpson, G. J., *Nonlinear optical polarization analysis in chemistry and biology*. Cambridge University Press: 2017.
19. Roth, S.; Freund, I., Second harmonic generation in collagen. *The Journal of chemical physics* **1979**, *70* (4), 1637-1643.
20. Fine, S.; Hansen, W., Optical second harmonic generation in biological systems. *Applied optics* **1971**, *10* (10), 2350-2353.

21. Guo, Y.; Ho, P.; Savage, H.; Harris, D.; Sacks, P.; Schantz, S.; Liu, F.; Zhadin, N.; Alfano, R., Second-harmonic tomography of tissues. *Optics Letters* **1997**, *22* (17), 1323-1325.
22. Williams, R. M.; Zipfel, W. R.; Webb, W. W., Interpreting second-harmonic generation images of collagen I fibrils. *Biophysical journal* **2005**, *88* (2), 1377-1386.
23. Dow, X. Y.; DeWalt, E. L.; Sullivan, S. Z.; Schmitt, P. D.; Ulcickas, J. R. W.; Simpson, G. J., Imaging the Nonlinear Susceptibility Tensor of Collagen by Nonlinear Optical Stokes Ellipsometry. *Biophys J* **2016**, *111* (7), 1361-1374.
24. Ding, C. Q.; Ulcickas, J. R. W.; Deng, F. Y.; Simpson, G. J., Second Harmonic Generation of Unpolarized Light. *Phys Rev Lett* **2017**, *119* (19), 193901.
25. Rieckhoff, K. E.; Peticolas, W. L., Optical second-harmonic generation in crystalline amino acids. *Science* **1965**, *147* (3658), 610-611.
26. Gualtieri, E.; Guo, F.; Kissick, D.; Jose, J.; Kuhn, R.; Jiang, W.; Simpson, G., Detection of membrane protein two-dimensional crystals in living cells. *Biophysical journal* **2011**, *100* (1), 207-214.
27. Kissick, D. J.; Wanapun, D.; Simpson, G. J., Second-order nonlinear optical imaging of chiral crystals. *Annual Review of Analytical Chemistry* **2011**, *4*, 419-437.
28. DeWalt, E. L.; Begue, V. J.; Ronau, J. A.; Sullivan, S. Z.; Das, C.; Simpson, G. J., Polarization-resolved second-harmonic generation microscopy as a method to visualize protein-crystal domains. *Acta Crystallographica Section D: Biological Crystallography* **2013**, *69* (1), 74-81.
29. DeWalt, E. L.; Sullivan, S. Z.; Schmitt, P. D.; Muir, R. D.; Simpson, G. J., Polarization-modulated second harmonic generation ellipsometric microscopy at video rate. *Anal Chem* **2014**, *86* (16), 8448-56.
30. Newman, J. A.; Zhang, S.; Sullivan, S. Z.; Dow, X. Y.; Becker, M.; Sheedlo, M. J.; Stepanov, S.; Carlsen, M. S.; Everly, R. M.; Das, C., Guiding synchrotron X-ray diffraction by multimodal video-rate protein crystal imaging. *Journal of synchrotron radiation* **2016**, *23* (4), 959-965.
31. Kestur, U. S.; Wanapun, D.; Toth, S. J.; Wegiel, L. A.; Simpson, G. J.; Taylor, L. S., Nonlinear optical imaging for sensitive detection of crystals in bulk amorphous powders. *Journal of pharmaceutical sciences* **2012**, *101* (11), 4201-4213.
32. Wanapun, D.; Kestur, U.; Taylor, L.; Simpson, G., Single particle nonlinear optical imaging of trace crystallinity in an organic powder. *Analytical chemistry* **2011**, *83* (12), 4745-4751.
33. Wanapun, D.; Kestur, U. S.; Kissick, D. J.; Simpson, G. J.; Taylor, L. S., Selective detection and quantitation of organic molecule crystallization by second harmonic generation microscopy. *Analytical chemistry* **2010**, *82* (13), 5425-5432.
34. Zhu, Q.; Toth, S. J.; Simpson, G. J.; Hsu, H.-Y.; Taylor, L. S.; Harris, M. T., Crystallization and dissolution behavior of naproxen/polyethylene glycol solid dispersions. *The Journal of Physical Chemistry B* **2013**, *117* (5), 1494-1500.

35. Toth, S.; Madden, J.; Taylor, L.; Marsac, P.; Simpson, G., Selective imaging of active pharmaceutical ingredients in powdered blends with common excipients utilizing two-photon excited ultraviolet-fluorescence and ultraviolet-second order nonlinear optical imaging of chiral crystals. *Analytical chemistry* **2012**, *84* (14), 5869-5875.
36. Newman, J. A.; Schmitt, P. D.; Toth, S. J.; Deng, F.; Zhang, S.; Simpson, G. J., Parts per million powder X-ray diffraction. *Analytical chemistry* **2015**, *87* (21), 10950-10955.
37. Nadiarnykh, O.; Campagnola, P. J. J. O. e., Retention of polarization signatures in SHG microscopy of scattering tissues through optical clearing. **2009**, *17* (7), 5794-5806.
38. Jones, R. C. J. J., A new calculus for the treatment of optical systemsi. description and discussion of the calculus. **1941**, *31* (7), 488-493.
39. Hurwitz, H.; Jones, R. C. J. J., A new calculus for the treatment of optical systemsii. proof of three general equivalence theorems. **1941**, *31* (7), 493-499.
40. Jones, R. C. J. J., A new calculus for the treatment of optical systemsIII. The sohncke theory of optical activity. **1941**, *31* (7), 500-503.
41. Jones, R. C. J. J., A new calculus for the treatment of optical systems. IV. **1942**, *32* (8), 486-493.
42. DeWalt, E. L.; Sullivan, S. Z.; Schmitt, P. D.; Muir, R. D.; Simpson, G. J., Polarization-Modulated Second Harmonic Generation Ellipsometric Microscopy at Video Rate. *Anal Chem* **2014**, *86* (16), 8448-8456.
43. Simpson, G. J. J. T. J. o. P. C. B., Connection of Jones and Mueller tensors in second harmonic generation and multi-photon fluorescence measurements. **2016**, *120* (13), 3281-3302.
44. Mahato, K.; Mazumder, N. J. L. i. m. s., Polarization-resolved Stokes-Mueller imaging: a review of technology and applications. **2019**.
45. Hornung, M.; Jain, A.; Frenz, M.; Akarçay, H. G. J. O. E., Interpretation of backscattering polarimetric images recorded from multiply scattering systems: a study on colloidal suspensions. **2019**, *27* (5), 6210-6239.
46. Zernike, F., Phase contrast, a new method for the microscopic observation of transparent objects part II. *Physica* **1942**, *9* (10), 974-986.
47. Zernike, F., How I Discovered Phase Contrast. *Science* **1955**, *121* (3141), 345-349.
48. Georges, N. Interferential polarizing device for study of phase objects. 1960.
49. Zernike, F., Phase contrast, a new method for the microscopic observation of transparent objects *Physica* **1942**, *9* (7), 686-698.
50. Dodt, H.-U.; Ziegler, W., Visualizing unstained neurons in living brain slices by infrared DIC-videomicroscopy. *Brain Research* **1990**, *537* (1), 333-336.
51. Gelles, J.; Schnapp, B. J.; Sheetz, M. P., Tracking kinesin-driven movements with nanometre-scale precision. *Nature* **1988**, *331*, 450-453.

52. Allen, R. D.; Allen, N. S.; Travis, J. L., Video-enhanced contrast, differential interference contrast (AVEC-DIC) microscopy: A new method capable of analyzing microtubule-related motility in the reticulopodial network of *allogromia laticollaris*. *Cell Motility* **1981**, *1* (3), 291-302.
53. Zernike, F. J. P., Phase contrast, a new method for the microscopic observation of transparent objects. **1942**, *9* (7), 686-698.
54. Hartman, J. S.; Gordon, R. L.; Lessor, D. L., Nomarski differential interference contrast microscopy for surface slope measurements: an examination of techniques. *Appl. Opt.* **1981**, *20* (15), 2665-2669.
55. Allen, R.; David, G., The Zeiss-Nomarski differential interference equipment for transmitted-light microscopy. *Zeitschrift fur wissenschaftliche Mikroskopie und mikroskopische Technik* **1969**, *69* (4), 193-221.
56. Zhang, T.; Yamaguchi, I., Three-dimensional microscopy with phase-shifting digital holography. *Opt. Lett.* **1998**, *23* (15), 1221-1223.
57. Mann, C. J.; Yu, L.; Lo, C.-M.; Kim, M. K., High-resolution quantitative phase-contrast microscopy by digital holography. *Opt. Express* **2005**, *13* (22), 8693-8698.
58. Kim, M. K., Digital holographic microscopy. In *Digital Holographic Microscopy*, Springer: 2011; pp 149-190.
59. Miccio, L.; Finizio, A.; Puglisi, R.; Balduzzi, D.; Galli, A.; Ferraro, P., Dynamic DIC by digital holography microscopy for enhancing phase-contrast visualization. *Biomed. Opt. Express* **2011**, *2* (2), 331-344.
60. Mehta, S. B.; Sheppard, C. J., Quantitative phase-gradient imaging at high resolution with asymmetric illumination-based differential phase contrast. *Opt. Lett.* **2009**, *34* (13), 1924-1926.
61. Vellekoop, I. M., Feedback-based wavefront shaping. *Opt. Express* **2015**, *23* (9), 12189-12206.
62. Lin, Y.-Z.; Huang, K.-Y.; Luo, Y., Quantitative differential phase contrast imaging at high resolution with radially asymmetric illumination. *Opt. Lett.* **2018**, *43* (12), 2973-2976.
63. Bon, P.; Maucort, G.; Wattellier, B.; Monneret, S., Quadriwave lateral shearing interferometry for quantitative phase microscopy of living cells. *Opt. Express* **2009**, *17* (15), 13080-13094.
64. Shaked, N. T., Quantitative phase microscopy of biological samples using a portable interferometer. *Opt. Lett.* **2012**, *37* (11), 2016-2018.
65. Wang, Z.; Millet, L.; Mir, M.; Ding, H.; Unarunotai, S.; Rogers, J.; Gillette, M. U.; Popescu, G., Spatial light interference microscopy (SLIM). *Optics express* **2011**, *19* (2), 1016-1026.
66. Zheng, G.; Horstmeyer, R.; Yang, C., Wide-field, high-resolution Fourier ptychographic microscopy. *Nature Photonics* **2013**, *7*, 739.

67. Hamilton, D.; Sheppard, C., Differential phase contrast in scanning optical microscopy. *Journal of microscopy* **1984**, *133* (1), 27-39.
68. Lin, Y.-H.; Wang, Y.-J.; Reshetnyak, V., Liquid crystal lenses with tunable focal length. *Liquid Crystals Reviews* **2017**, *5* (2), 111-143.
69. Suyama, S.; Date, M.; Takada, H. J. J. o. A. P., Three-dimensional display system with dual-frequency liquid-crystal varifocal lens. **2000**, *39* (2R), 480.
70. Chen, B.-C.; Legant, W. R.; Wang, K.; Shao, L.; Milkie, D. E.; Davidson, M. W.; Janetopoulos, C.; Wu, X. S.; Hammer, J. A.; Liu, Z. J. S., Lattice light-sheet microscopy: imaging molecules to embryos at high spatiotemporal resolution. **2014**, *346* (6208), 1257998.
71. Sato, S. J. J. J. o. A. P., Liquid-crystal lens-cells with variable focal length. **1979**, *18* (9), 1679.
72. Wang, B.; Ye, M.; Sato, S. J. A. o., Lens of electrically controllable focal length made by a glass lens and liquid-crystal layers. **2004**, *43* (17), 3420-3425.
73. Purvis, A.; Clark, M. G., Electrically-controllable thin film Fresnel zone device. Google Patents: 1990.
74. Seow, Y.; Lim, S.; Lee, H. J. A. P. L., Tunable optofluidic switch via hydrodynamic control of laminar flow rate. **2009**, *95* (11), 114105.
75. McLeod, E.; Arnold, C. B. J. J. o. A. P., Mechanics and refractive power optimization of tunable acoustic gradient lenses. **2007**, *102* (3), 033104.
76. Lansford, R.; Bearman, G.; Fraser, S. E., Resolution of multiple green fluorescent protein color variants and dyes using two-photon microscopy and imaging spectroscopy. *J Biomed Opt* **2001**, *6* (3), 311-8.
77. Bertani, F. R.; Botti, E.; Ferrari, L.; Mussi, V.; Costanzo, A.; D'Alessandro, M.; Cilloco, F.; Selci, S., Label-free and non-invasive discrimination of HaCaT and melanoma cells in a co-culture model by hyperspectral confocal reflectance microscopy. *J Biophotonics* **2016**, *9* (6), 619-25.
78. Arrigoni, S.; Turra, G.; Signoroni, A., Hyperspectral image analysis for rapid and accurate discrimination of bacterial infections: A benchmark study. *Comput Biol Med* **2017**, *88*, 60-71.
79. Rink, C. L.; Wernke, M. M.; Powell, H. M.; Tornero, M.; Gnyawali, S. C.; Schroeder, R. M.; Kim, J. Y.; Denune, J. A.; Albury, A. W.; Gordillo, G. M.; Colvin, J. M.; Sen, C. K., Standardized Approach to Quantitatively Measure Residual Limb Skin Health in Individuals with Lower Limb Amputation. *Adv Wound Care (New Rochelle)* **2017**, *6* (7), 225-232.
80. Cull, C. F.; Choi, K.; Brady, D. J.; Oliver, T., Identification of fluorescent beads using a coded aperture snapshot spectral imager. *Appl Opt* **2010**, *49* (10), B59-70.
81. Gao, L.; Kester, R. T.; Hagen, N.; Tkaczyk, T. S., Snapshot Image Mapping Spectrometer (IMS) with high sampling density for hyperspectral microscopy. *Opt Express* **2010**, *18* (14), 14330-44.

CHAPTER 2. SECOND HARMONIC GENERATION OF UNPOLARIZED LIGHT

A version of this chapter has been published by *Physical Review Letters*. Reprinted with permission from Changqin Ding, James R. W. Ulcickas, Fengyuan Deng, and Garth J. Simpson. Second harmonic generation of unpolarized light. *Physical Review Letters*. 119(19), 193901, 2017. Copyright (2017) by the American Physical Society.

A Mueller tensor mathematical framework was applied for predicting and interpreting the second harmonic generation (SHG) produced with an unpolarized fundamental beam. In deep tissue imaging through SHG and multiphoton fluorescence, partial or complete depolarization of the incident light complicates polarization analysis. The proposed framework has the distinct advantage of seamlessly merging the purely polarized theory based on the Jones or Cartesian susceptibility tensors with a more general Mueller tensor framework capable of handling partial depolarized fundamental and/or SHG produced. The predictions of the model are in excellent agreement with experimental measurements of z-cut quartz and mouse tail tendon obtained with polarized and depolarized incident light. The polarization-dependent SHG produced with unpolarized fundamental allowed determination of collagen fiber orientation in agreement with orthogonal methods based on image analysis. This method has the distinct advantage of being immune to birefringence or depolarization of the fundamental beam for structural analysis of tissues.

2.1 Introduction

Second harmonic generation (SHG) is a second order nonlinear optical process that is only allowed for structures without an inversion center. Due to these specific symmetry properties, SHG is sensitive to polarization dependent measurement, providing rich information on orientation and arrangement of local structures. Over the last two decades, polarization dependent SHG microscopy has been demonstrated for characterization of biostructures¹⁻⁴, protein crystals⁵, and active pharmaceutical ingredients^{5, 6}. However, the rich structural information inherent in SHG polarization analysis is routinely lost in measurements designed to take advantage of the increased penetration depth of nonlinear optical interactions. SHG scales quadratically with the incident intensity, such that only locations of high intensity contribute to

the detected signal. In beam-scanning instruments, image contrast in SHG is generally retained in turbid media for much greater depths than analogous linear interactions. Though the ubiquitous use near IR incident light exhibits deeper penetration and less damage for thick biological samples⁷⁻⁹, the native turbidity and/or birefringence of biological media has the potential to complicate polarization dependent measurements through partial or complete depolarization of the incident and/or detected light.

Several studies have considered the effects of partial depolarization in polarization-dependent nonlinear optical imaging via the cumulative effects of scattering, birefringence, and linear/circular dichroism^{3, 4, 10}. Optical clearing is one approach to mitigate the effects of scattering by refractive index matching¹¹. Careful bookkeeping of polarization-state changes via experimentally recovered parameterization has been used to great success to remove bias in recovered tensor elements from polarization resolved SHG microscopy at tissue depths of 100 μm ^{3, 4, 10}. However, such methods do not account for the influence of depolarization arising from heterogeneity within the sample during propagation to the object plane. More recently, Mueller tensor methods have been introduced for quantitatively understanding and correcting for depolarization effects in nonlinear optical measurements. Barzda and coworkers have introduced the Stokes-Mueller framework for the theoretical description of nonlinear optical polarimetry based on a “super-Mueller matrix” approach originally developed by McClain and Shi¹²⁻¹⁴. This approach has been used to study crystalline and collagen fibril organization for polarization dependent measurements.^{15, 16} However, a large number of observables with many different incident polarization states are required in order to populate all 36 unique elements of the super-Mueller matrix. In a recent complementary framework,¹⁷ the Mueller tensors in partially depolarizing assemblies were greatly simplified by directly bridging Jones and Mueller tensors. The role of partial depolarization can in principle be incorporated by a single additional adjustable parameter relative to analogous measurements in non-depolarizing assemblies.

In principle, linear optical interactions can be used to describe much of the depolarization effects in nonlinear optics. Giving an example, in SHG microscopy of turbid media, the collective process can be conceptually broken down into three key steps: i) propagation of the fundamental beam through the turbid matrix to the object plane, ii) production of SHG by the object of interest by the Mueller tensor $M^{(2)}$, and iii) propagation of the frequency-doubled light to the far-field detector. In steps i) and iii), partial depolarization of the incident and detected

beams can in principal be handled by conventional linear Mueller matrices. However, step ii) is the key step that cannot be described by either linear Mueller matrix transformations or considerations of conventional nonlinear polarizability based on Jones and/or Cartesian tensors due to the partially depolarized fundamental.

In this chapter, the process of SHG driven by unpolarized light was considered both theoretically and experimentally, and then applied to recover both polar and azimuthal orientation of collagen fibrils. In a model system, predictions from a mathematical framework connecting Jones and Mueller tensors¹⁷ were compared with observations for z-cut quartz. With this framework in place, polarization-dependent SHG from partial depolarization of the incident beam can be quantitatively described using the intuitive Jones tensor.

2.2 Theoretical foundation

2.2.1 Stokes Vector and Jones Tensor for detected SHG

In the most general manner, the rank three Mueller tensor $M^{(2)}$ describing SHG in the presence of partial depolarization can be written as $\bar{s}_{det}^{2\omega} = \mathbf{M}_{det}^{(2)} : \bar{s}^\omega \bar{s}^\omega$, in which the Stokes vector describing the detected SHG is given by the tensor product of the Mueller tensor and the incident Stokes vector \bar{s}^ω . The tensor product can be rewritten using a vectorized form of the Mueller tensor, as described in previous work.¹⁷ It can be rewritten as Eq. (2.1).

$$\bar{s}_{det}^{2\omega} = \left[I_4 \otimes (\bar{s}^\omega)^T \otimes (\bar{s}^\omega)^T \right] \cdot \bar{\mathbf{M}}_{det} \quad (2.1)$$

In Eq. (2.1), I_4 is a 4×4 identity matrix and $\bar{\mathbf{M}}$ is the 64-element ascending vectorized form of the Mueller tensor, and the symbol \otimes indicates a Kronecker product.

In SHG microscopy of a turbid sample, partial depolarization of the incident and detected beams can be in principal handled by conventional linear Mueller matrices.

$$\bar{s}_{det}^{2\omega} = M^{2\omega} \cdot \bar{s}_{obj}^{2\omega} = M^{2\omega} \cdot \mathbf{M}_{obj}^{(2)} : (M^\omega \cdot \bar{s}^\omega) (M^\omega \cdot \bar{s}^\omega) \quad (2.2)$$

The two sets of linear Mueller matrices can be combined with the underlying Mueller tensor of the object $\mathbf{M}_{obj}^{(2)}$ to describe the net observed Mueller tensor.

$$\mathbf{M}_{det}^{(2)} = (M^{2\omega} \cdot \mathbf{M}_{obj}^{(2)} : M^\omega M^\omega) \quad (2.3)$$

In the simplest model for partial depolarization, the fundamental light reaching the object plane as a simple linear combination of a fully depolarized fraction (α) and a residual purely polarized component ($1-\alpha$). For depolarized component of the incident light, s_0 is the only nonzero entry in the Stokes vector for the fundamental. Upon making this substitution, only a subset of 4 elements within the Mueller tensor contribute to the Stokes vector produced from a depolarized source: M_{000} , M_{100} , M_{200} , and M_{300} , respectively corresponding to the decimal positions of 0, 16, 32, and 48 in the vectorized tensor. In this case, the Stokes vector for the SHG maps directly onto those four Mueller tensor elements.

$$\begin{bmatrix} s_0 \\ s_1 \\ s_2 \\ s_3 \end{bmatrix}_{obj}^{2\omega} = \alpha \cdot \bar{s}_{depol}^{2\omega} + (1-\alpha) \cdot \bar{s}_{pol}^{2\omega} = \alpha \cdot \begin{bmatrix} M_{000} \\ M_{100} \\ M_{200} \\ M_{300} \end{bmatrix}_{depol} + (1-\alpha) \cdot \mathbf{M}_{pol}^{(2)} : \bar{s}_{in}^{\omega} \bar{s}_{in}^{\omega} \quad (2.4)$$

The purely polarized component scaled by $(1-\alpha)$ can be handled in the conventional way by switching to a Jones tensor description for SHG with purely polarized inputs, such that $\bar{e}_{obj}^{-2\omega} = \chi_{obj}^{(2)} : \bar{e}_{obj}^{-\omega} \bar{e}_{obj}^{-\omega}$ and $\bar{s}_{pol}^{2\omega} = A \cdot \left(\bar{e}_{obj}^{-2\omega} \otimes \bar{e}_{obj}^{-2\omega} \right)$. It describes the Stokes vector produced by the fully depolarized component of the fundamental beam at the object plane, which raises conceptual and mathematical questions regarding prediction of the anticipated output.

The elements of the Mueller tensor describing SHG driven by partially or fully depolarized incident light were connected back to combinations of simpler Jones tensor elements. The expression bridging the two formalisms was derived in earlier work as shown in Eq. (2.5).¹⁷

$$\mathbf{M}^{(2)} = A \cdot \left(\chi_J^{(2)*} \otimes \chi_J^{(2)} \right) : A^{-1} A^{-1} \quad (2.5)$$

It can be rewritten in vectorized form as below.

$$\bar{\mathbf{M}} = \left[A \otimes (A^{-1})^T \otimes (A^{-1})^T \right] \cdot \overline{\left(\chi_J^{(2)*} \otimes \chi_J^{(2)} \right)} \quad (2.6)$$

The matrix A is the well-established transformation matrix connecting the Jones and Stokes vectors for purely polarized light.^{17, 18}

$$\bar{s} = \begin{bmatrix} 1 & 0 & 0 & 1 \\ 1 & 0 & 0 & -1 \\ 0 & 1 & 1 & 0 \\ 0 & i & -i & 0 \end{bmatrix} \cdot \begin{pmatrix} \bar{e}_0^* \bar{e}_0 \\ \bar{e}_0^* \bar{e}_1 \\ \bar{e}_1^* \bar{e}_0 \\ \bar{e}_1^* \bar{e}_1 \end{pmatrix} = A \cdot \left(\bar{e}^* \otimes \bar{e} \right) \quad (2.7)$$

In linear optics, connecting the Mueller matrices to Jones matrices provides a more intuitive framework for interpreting polarization propagation. Using the preceding relationship bridging the Stokes and Jones vectors allows the 4×4 Mueller matrix M to be written in terms of the 2×2 Jones matrix J : $M = A \cdot (J \otimes J) \cdot A^{-1}$. These connections between Mueller and Jones matrices in linear optics were shown to be directly extendable to nonlinear optics, in which the elements of the $4 \times 4 \times 4$ Mueller tensor describing SHG $M^{(2)}$ driven by partially or fully depolarized incident light are connected back to combinations of simpler $2 \times 2 \times 2$ Jones tensor elements $\chi_J^{(2)}$ with the same transformation matrix A .

$$\bar{s}^{2\omega} = \left[I_4 \otimes (\bar{s}^\omega)^T \otimes (\bar{s}^\omega)^T \right] \cdot \left[A \otimes (A^{-1})^T \otimes (A^{-1})^T \right] \cdot \overline{(\chi_J^{(2)*} \otimes \chi_J^{(2)})} \quad (2.8)$$

Eq. (2.8) allows identification of the nonzero combinations of Jones tensor elements contributing to the SHG produced with unpolarized incident light.

2.2.2 Connecting the Stokes Vector and Jones Tensor for Depolarized Light

Eq. (2.8) can be rewritten in the following form.

$$\bar{s}^{2\omega} = (I_4 \cdot A) \otimes \left[(\bar{s}^\omega)^T \otimes (\bar{s}^\omega)^T \cdot (A^{-1})^T \otimes (A^{-1})^T \right] \cdot \overline{(\chi_J^{(2)*} \otimes \chi_J^{(2)})} \quad (2.9)$$

Since any matrix commutes with the identity matrix, Eq. (2.9) can be rewritten inverting the order of I_4 and A . Regrouping with the associative properties of Kronecker products allows rearrangement to Eq. (2.10).

$$\bar{s}^{2\omega} = A \cdot \left\{ (I_4) \otimes \left[(\bar{s}^\omega)^T \otimes (\bar{s}^\omega)^T \cdot (A^{-1})^T \otimes (A^{-1})^T \right] \right\} \cdot \overline{(\chi_J^{(2)*} \otimes \chi_J^{(2)})} \quad (2.10)$$

The transpose operation can be more conveniently evaluated over the entire set of terms within brackets as shown in Eq. (2.11).

$$\bar{s}^{2\omega} = A \cdot \left\{ I_4 \otimes (A^{-1} \otimes A^{-1}) \cdot (\bar{s}^\omega \otimes \bar{s}^\omega) \right\}^T \cdot \overline{(\chi_J^{(2)*} \otimes \chi_J^{(2)})} \quad (2.11)$$

Using the identity $(A \otimes B) \cdot (C \otimes D) = (A \cdot B) \otimes (C \cdot D)$ allows regrouping of Eq. (2.11).

$$\bar{s}^{2\omega} = A \cdot \left\{ I_4 \otimes (A^{-1} \cdot \bar{s}^\omega) \otimes (A^{-1} \cdot \bar{s}^\omega) \right\}^T \cdot \overline{(\chi_J^{(2)*} \otimes \chi_J^{(2)})} \quad (2.12)$$

The 4-element vector $A^{-1} \cdot \bar{s}^\omega$ contains only two nonzero entries for depolarized light.

$$A^{-1} \cdot \bar{s}^\omega = \frac{1}{2} \begin{bmatrix} 1 \\ 0 \\ 0 \\ 1 \end{bmatrix} \quad (2.13)$$

The Kronecker product of $(A^{-1} \cdot \bar{s}^\omega) \otimes (A^{-1} \cdot \bar{s}^\omega)$ produces a 16-element vector with the following nonzero entries: 0, 3, 12, 15, which in binary correspond to 000000, 000011, 001100, 001111, respectively.

Following an additional Kronecker product by the identity matrix, this same set of four entries exclusively contributes to $s_0^{2\omega}$, the set 010000, 010011, 011100, and 011111 (corresponding to indices 16, 19, 28, and 31, respectively) contribute exclusively to $s_1^{2\omega}$, etc.

The nonzero Jones tensor elements can be regrouped with the first index in each of the χ_{ijk} tensor elements corresponds to the electric field component produced by the nonlinear optical process. In addition to clarifying the underlying patterns, the 0/1 notation has subsequent book-keeping benefits from binary counting. Most notably, only a small subset of the entries within the product $\overline{(\chi_j^{(2)*} \otimes \chi_j^{(2)})}$ contributes to the measured Stokes vector, with binary notation aiding in their identification. As described in previous work¹⁸, the specific combinations of tensor elements within the vector $\overline{(\chi_j^{(2)*} \otimes \chi_j^{(2)})}$ can be generated by re-ordering of the 0 and 1 entries in the binary number.

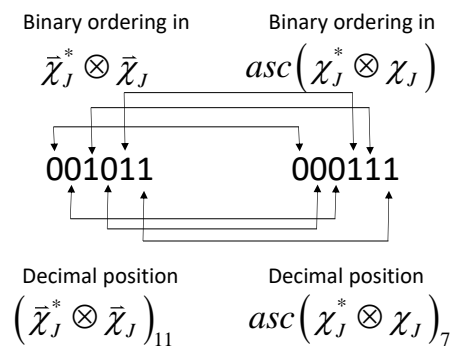


Figure 2.1 Combination of tensor elements by re-ordering the 0 and 1 entries in the binary number.

Using the first four entries to illustrate this process, the binary number 000000 corresponds to the combination of Jones tensor element $\chi_{000}^* \chi_{000}$, the number 000011 corresponds to $\chi_{001}^* \chi_{001}$, the number 001100 corresponds to $\chi_{010}^* \chi_{010}$, and the number 001111 corresponds to $\chi_{011}^* \chi_{011}$, where 0 indicates the laboratory horizontal axis and 1 indicates the laboratory vertical axis. Since only these four elements contribute to $s_0^{2\omega}$, explicit evaluation of the term in curly brackets in Eq. (2.12) multiplied by the vectorized tensor element products yields the first row of the right-most vector in Eq. (2.14). An analogous set of operations allows population of the remaining three rows in that same right-most vector in Eq. (2.14).

$$\begin{bmatrix} s_0 \\ s_1 \\ s_2 \\ s_3 \end{bmatrix}^{2\omega} = \frac{1}{4} \begin{bmatrix} 1 & 0 & 0 & 1 \\ 1 & 0 & 0 & -1 \\ 0 & 1 & 1 & 0 \\ 0 & i & -i & 0 \end{bmatrix} \begin{bmatrix} \chi_{000}^* \chi_{000} + \chi_{001}^* \chi_{001} + \chi_{010}^* \chi_{010} + \chi_{011}^* \chi_{011} \\ \chi_{000}^* \chi_{100} + \chi_{001}^* \chi_{101} + \chi_{010}^* \chi_{110} + \chi_{011}^* \chi_{111} \\ \chi_{100}^* \chi_{000} + \chi_{101}^* \chi_{001} + \chi_{110}^* \chi_{010} + \chi_{111}^* \chi_{011} \\ \chi_{100}^* \chi_{100} + \chi_{101}^* \chi_{101} + \chi_{110}^* \chi_{110} + \chi_{111}^* \chi_{111} \end{bmatrix} \quad (2.14)$$

2.2.3 Connecting Local and Laboratory Frames

Symmetry within the local-frame system can significantly reduce the number of nonzero Jones tensor elements. In the case of collagen (or any uniaxial assembly) aligned along the horizontal laboratory-frame axis, the nonzero elements within the collagen frame are $\chi_{z'z'z'}$, $\chi_{x'x'x'}$, $\chi_{x'x'z'} = \chi_{x'z'x'}$, and $\chi_{x'y'z'} = \chi_{x'z'y'} = -\chi_{y'x'z'} = -\chi_{y'z'x'}$, with the z' -axis defined as the unique fiber axis. From quantum chemical calculations, the chiral terms are predicted to be relatively weak in collagen performed far from resonance, and disappear by symmetry for fibers aligned within the field of view (FoV) in the plane-wave approximation^{4, 19}.

The Jones-Mueller connection provides a means of quantitatively predicting the SHG produced from depolarized light using the knowledge of SHG originating for pure polarization states. If the local-frame z' -axis is coparallel with the laboratory-frame horizontal (0) axis and the x' -axis is coparallel with the laboratory vertical (1) axis, inspection of Eq. (2.14) indicates that only the following four tensor element products will contribute to the detected Stokes vector for the SHG: $|\chi_{000}|^2$, $|\chi_{011}|^2$, $|\chi_{101}|^2$, and $|\chi_{110}|^2$. For the z' -axis oriented coparallel with the laboratory horizontal axis in the laboratory Jones frame, the only two of the four nonzero elements in the Jones tensor describing collagen remained as: $\chi_{000} = \chi_{z'z'z'}$, $\chi_{011} = \chi_{z'x'x'}$, and

$\chi_{110} = \chi_{101} = \chi_{x'x'z'}$. Substitution into Eq. (2.14) yields the following expression for the Stokes vector produced for an unpolarized input beam.

$$\begin{bmatrix} s_0 \\ s_1 \\ s_2 \\ s_3 \end{bmatrix}^{2\omega} = \frac{1}{4} \begin{bmatrix} |\chi_{z'z'z'}|^2 + |\chi_{z'x'x'}|^2 + 2|\chi_{x'x'z'}|^2 \\ |\chi_{z'z'z'}|^2 + |\chi_{z'x'x'}|^2 - 2|\chi_{x'x'z'}|^2 \\ 0 \\ 0 \end{bmatrix}_{\phi=0} \quad (2.15)$$

The subscript $\phi = 0$ indicates a collagen fiber axis coparallel with the horizontal laboratory-frame axis, corresponding to an azimuthal rotation angle ϕ of zero (i.e., in which the local frame and laboratory frame have a specific correspondence). This expression can be generalized to include arbitrary azimuthal rotation by introduction of rotation matrices.

For unpolarized incident light, the net SHG can be considered as arising from the incoherent summation of these three contributions. In general, the collagen principal axis will not be oriented exclusively along either the vertical or horizontal axes. Two equivalent strategies can be taken: i) generate the Mueller tensor for a uniaxial assembly in the local frame, then project onto the laboratory frame coordinates, or ii) generate the Jones tensor for a uniaxial assembly, then project onto the laboratory frame. The equivalence of these two approaches can be demonstrated as follows. The vectorized form for the laboratory frame Mueller tensor is connected to the vectorized local-frame Mueller tensor by a rotation operation.¹⁷

$$\bar{M}_L = (R_\phi \otimes R_\phi \otimes R_\phi) \cdot \bar{M}'_l \quad (2.16)$$

The prime on the local-frame Mueller tensor indicates that all 64 elements are included in the vectorized form, many of which will be zero-valued by the assumption of local uniaxial symmetry. The rotation matrix R_ϕ is given by Eq.(2.17), where R_ϕ is the rotation matrix for a Jones vector described in Eq.(2.18).

$$R_\phi = A \cdot (R_\phi \otimes R_\phi) \cdot A^{-1} \quad (2.17)$$

$$R_\phi = \begin{bmatrix} \cos \phi & \sin \phi \\ -\sin \phi & \cos \phi \end{bmatrix} \quad (2.18)$$

Substitution of the rotated tensor expression in Eq. (2.16) into Eq. (2.1) yields the following expression for the Stokes vector describing SHG.

$$\bar{s}^{2\omega} = \left[I_4 \otimes (\bar{s}^\omega)^T \otimes (\bar{s}^\omega)^T \right] \cdot (R_\phi \otimes R_\phi \otimes R_\phi) \cdot \bar{M}' \quad (2.19)$$

The Stokes vector can be connected back to the elements of the Jones vector by substitution of the relation in Eq. (2.6) using the complete set of local-frame tensor elements.

$$\bar{s}^{2\omega} = \frac{1}{4} \left[I_4 \otimes (\bar{s}^\omega)^T \otimes (\bar{s}^\omega)^T \right] \cdot (R_\phi \otimes R_\phi \otimes R_\phi) \cdot \left[A \otimes (A^{-1})^T \otimes (A^{-1})^T \right] \cdot \overline{(\chi_l^{(2)*} \otimes \chi_l^{(2)})} \quad (2.20)$$

Rearrangement of the middle terms:

$$(R_\phi \otimes R_\phi \otimes R_\phi) \cdot \left[A \otimes (A^{-1})^T \otimes (A^{-1})^T \right] = \left[(R_\phi \cdot A) \otimes (R_\phi \cdot (A^{-1})^T) \otimes (R_\phi \cdot (A^{-1})^T) \right] \quad (2.21)$$

Connecting the Mueller and Jones rotation matrices allows the following substitution.

$$R_\phi A = \left[A \cdot (R_\phi \otimes R_\phi) \cdot A^{-1} \right] A = A \cdot (R_\phi \otimes R_\phi) \quad (2.22)$$

Substitution into Eq. (2.8) yields the following simplification.

$$\begin{aligned} & (R_\phi \otimes R_\phi \otimes R_\phi) \cdot \left[A \otimes (A^{-1})^T \otimes (A^{-1})^T \right] \\ &= \left[A \otimes (A^{-1})^T \otimes (A^{-1})^T \right] \cdot \left[R_\phi \otimes R_\phi \otimes R_\phi \otimes R_\phi \otimes R_\phi \otimes R_\phi \right] \end{aligned} \quad (2.23)$$

For an achiral assembly with local uniaxial symmetry, only four nonzero tensor elements remain for SHG; $\chi_{z'z'z'}$, $\chi_{z'x'x'}$, $\chi_{x'x'z'}$, and $\chi_{x'z'x'}$. These collectively produce 16 nonzero combinations in the Kronecker product in Eq. (2.23), which map to the laboratory frame tensor elements in Eq. (2.14).

$$\begin{aligned} & \begin{bmatrix} \chi_{000}^* \chi_{000} + \chi_{001}^* \chi_{001} + \chi_{010}^* \chi_{010} + \chi_{011}^* \chi_{011} \\ \chi_{000}^* \chi_{100} + \chi_{001}^* \chi_{101} + \chi_{010}^* \chi_{110} + \chi_{011}^* \chi_{111} \\ \chi_{100}^* \chi_{000} + \chi_{101}^* \chi_{001} + \chi_{110}^* \chi_{010} + \chi_{111}^* \chi_{011} \\ \chi_{100}^* \chi_{100} + \chi_{101}^* \chi_{101} + \chi_{110}^* \chi_{110} + \chi_{111}^* \chi_{111} \end{bmatrix} \\ &= \begin{bmatrix} \cos^2 \phi & \cos^2 \phi & \sin^2 \phi & \sin^2 \phi \\ \sin \phi \cos \phi & \sin \phi \cos \phi & -\sin \phi \cos \phi & -\sin \phi \cos \phi \\ \sin \phi \cos \phi & \sin \phi \cos \phi & -\sin \phi \cos \phi & -\sin \phi \cos \phi \\ \sin^2 \phi & \sin^2 \phi & \cos^2 \phi & \cos^2 \phi \end{bmatrix} \cdot \begin{bmatrix} |\chi_{z'z'z'}|^2 \\ |\chi_{z'x'x'}|^2 \\ |\chi_{x'z'x'}|^2 \\ |\chi_{x'x'z'}|^2 \end{bmatrix} \end{aligned} \quad (2.24)$$

Substitution of this equality into Eq. (2.14) and evaluation of the multiplication by A yields Eq. (2.25).

$$\begin{bmatrix} s_0 \\ s_1 \\ s_2 \\ s_3 \end{bmatrix}^{2\omega} = \frac{1}{4} \begin{bmatrix} 1 & 1 & 1 & 1 \\ \cos^2 \phi - \sin^2 \phi & \cos^2 \phi - \sin^2 \phi & \sin^2 \phi - \cos^2 \phi & \sin^2 \phi - \cos^2 \phi \\ 2 \sin \phi \cos \phi & 2 \sin \phi \cos \phi & 2 \sin \phi \cos \phi & 2 \sin \phi \cos \phi \\ 0 & 0 & 0 & 0 \end{bmatrix} \cdot \begin{bmatrix} |\chi_{z'z'z'}|^2 \\ |\chi_{z'x'x'}|^2 \\ |\chi_{x'z'x'}|^2 \\ |\chi_{x'x'z'}|^2 \end{bmatrix} \quad (2.25)$$

Combining trigonometric identities $2 \sin \phi \cos \phi = \sin(2\phi)$ and $\cos^2 \phi - \sin^2 \phi = \cos(2\phi)$ together with the equality $|\chi_{x'x'z'}|^2 = |\chi_{z'x'x'}|^2$ for SHG yields the simplified form of the equation given in Eq. (2.26).

$$\begin{bmatrix} s_0 \\ s_1 \\ s_2 \\ s_3 \end{bmatrix}^{2\omega} = \frac{1}{4} \begin{bmatrix} 1 & 1 & 1 \\ \cos(2\phi) & \cos(2\phi) & -\cos(2\phi) \\ -\sin(2\phi) & -\sin(2\phi) & \sin(2\phi) \\ 0 & 0 & 0 \end{bmatrix} \begin{bmatrix} |\chi_{z'z'z'}|^2 \\ |\chi_{z'x'x'}|^2 \\ 2|\chi_{x'x'z'}|^2 \end{bmatrix} \quad (2.26)$$

Consistent with previous reports^{3-5, 15} for z-cut quartz and collagen far from resonance, Eq. (2.26) can be simplified by making the approximation of $|\chi_{z'x'x'}| \cong |\chi_{x'x'z'}|$ and rewritten with two parameters: the azimuthal rotation angle ϕ and a defined ratio $\rho \equiv \chi_{z'z'z'} / \chi_{z'x'x'}$.

$$\begin{bmatrix} s_0 \\ s_1 \\ s_2 \\ s_3 \end{bmatrix}^{2\omega} = \frac{|\chi_{z'x'x'}|^2}{4} \begin{bmatrix} 1 & 1 & 1 \\ \cos(2\phi) & \cos(2\phi) & -\cos(2\phi) \\ -\sin(2\phi) & -\sin(2\phi) & \sin(2\phi) \\ 0 & 0 & 0 \end{bmatrix} \begin{bmatrix} |\rho|^2 \\ 1 \\ 2 \end{bmatrix} \quad (2.27)$$

Eqs. (2.26) and (2.27) are derived under the assumption that sample is aligned within the FoV with polar tilt angle of $\pi/2$ and ρ equal to the local frame ratio given above. The same tensor elements are also present for collagen with tilt angles other than $\pi/2$ (neglecting relatively weak chiral-specific contributions). In those cases, ρ equals to the ratio of projected $\chi_{z'z'z'}$ and $\chi_{z'x'x'}$ within the FoV, defined as χ_{XXX} / χ_{XYX} . To avoid confusion in the later discussion, ρ_l is defined as the local frame tensor ratio with tilt angle $\theta = \pi/2$, and ρ as the measured laboratory-frame ratio χ_{XXX} / χ_{XYX} for any arbitrary tilt angle θ .

The measured intensity in the laboratory frame can be calculated by combining the first two elements in the laboratory-frame Stoke vector \bar{s}_L using Eq. (2.28).

$$\begin{aligned}
I_H^{2\omega} &= \frac{1}{2} [s_{0,L} + s_{1,L}] \\
s_{0,L} &= I_H + I_V \\
s_{1,L} &= I_H - I_V
\end{aligned} \tag{2.28}$$

The measured intensity for polarizer at an arbitrary angle ϕ_{pol} can similarly be obtained by projecting the laboratory frame Stokes vector \bar{s}_L onto the reference frame of the polarizer given by \bar{s}_{pol} , given in Eq.(2.29).¹⁷

$$\bar{s}_{pol} = \begin{bmatrix} 1 & 0 & 0 & 0 \\ 0 & \cos(2\phi_{pol}) & -\sin(2\phi_{pol}) & 0 \\ 0 & \cos(2\phi_{pol}) & \cos(2\phi_{pol}) & 0 \\ 0 & 0 & 0 & 1 \end{bmatrix} \cdot \bar{s}_L \tag{2.29}$$

Combining Eq. (2.28) and (2.29) yields the Eq. (2.30) for detected SHG intensity after a post sample polarizer at angle ϕ_{pol} , with s_0 normalized to unity through the proportionality constant C .

$$I^{2\omega}(\phi_{pol}) = \frac{C}{2} [s_0 + s_1 \cos(2\phi_{pol}) - s_2 \sin(2\phi_{pol})] \tag{2.30}$$

Combining Eqs. (2.27) and (2.30), the measured laboratory-frame ratio ρ can be determined by a linear fit to the measured intensities based on Eq. (2.31).

$$I^{2\omega}(\phi_{pol}) = \frac{C}{8} [(|\rho|^2 + 3) + (|\rho|^2 - 1) \cos(2\phi_{pol} - 2\phi)] \tag{2.31}$$

2.2.4 Measurements acquired with polarized incident light

The laboratory-frame Jones tensor describing the NLO properties of a uniaxial assembly with the unique axis lying within the field of view is given by Eq. (2.32).²⁰

$$\begin{bmatrix} \chi_{HHH} \\ \chi_{HHV} \\ \chi_{H VH} \\ \chi_{HVV} \\ \chi_{VHH} \\ \chi_{VHV} \\ \chi_{VVH} \\ \chi_{VVV} \end{bmatrix} = \begin{bmatrix} 2g & g & i \\ f-h & -h & h \\ f-h & -h & h \\ -2g & i & g \\ -2h & f & h \\ i-g & -g & g \\ i-g & -g & g \\ 2h & h & f \end{bmatrix} \cdot \begin{bmatrix} \chi_{x'x'z'} \\ \chi_{z'x'x'} \\ \chi_{z'z'z'} \end{bmatrix} ; \begin{cases} f = \sin^3 \phi \\ g = \sin^2 \phi \cos \phi \\ h = \sin \phi \cos^2 \phi \\ i = \cos^3 \phi \end{cases} \tag{2.32}$$

In Eq. (2.32), ϕ is the rotation angle of the primary sample z'-axis relative to the laboratory horizontal axis. The Jones vector describing the polarization-dependent SHG is linked to the Jones tensor and the rotation angle γ of the incident polarization through the following expression.

$$\vec{e}_L^{2\omega} = \begin{bmatrix} \cos^2 \gamma & \sin \gamma \cos \gamma & \sin \gamma \cos \gamma & \sin^2 \gamma & 0 & 0 & 0 & 0 \\ 0 & 0 & 0 & 0 & \cos^2 \gamma & \sin \gamma \cos \gamma & \sin \gamma \cos \gamma & \sin^2 \gamma \end{bmatrix} \cdot \begin{bmatrix} \chi_{HHH} \\ \chi_{HHV} \\ \chi_{HVV} \\ \chi_{VHH} \\ \chi_{VHV} \\ \chi_{VVH} \\ \chi_{VVV} \end{bmatrix} \quad (2.33)$$

The SHG intensity detected through a polarizer rotated an angle ϕ_{pol} is given by Eq. (2.34).

$$I^{2\omega}(\phi_{pol}) \propto \left[\begin{bmatrix} 1 & 0 \\ 0 & 0 \end{bmatrix} \begin{bmatrix} \cos \phi_{pol} & \sin \phi_{pol} \\ -\sin \phi_{pol} & \cos \phi_{pol} \end{bmatrix} \begin{bmatrix} e_H^{2\omega} \\ e_V^{2\omega} \end{bmatrix} \right]^2 \quad (2.34)$$

$$\propto \left| e_H^{2\omega} \cos \phi_{pol} + e_V^{2\omega} \sin \phi_{pol} \right|^2$$

With vertically polarized incident light, the combination of Eqs. (2.33) and (2.34) yields Eq. (2.35).

$$I^{2\omega}(\phi_{pol})^2 \propto \left| \chi_{HVV} \cos \phi_{pol} + \chi_{VVV} \sin \phi_{pol} \right|^2 \quad (2.35)$$

Substitution of the relations in Eq. (2.32) followed by trigonometric simplification yields Eq. (2.36).

$$I^{2\omega}(\phi_{pol}) \propto \left| \chi_{x'x'z'} \sin(2\phi) \cos(\phi - \phi_{pol}) + \sin(\phi - \phi_{pol}) \left[\chi_{z'z'z'} \cos^2 \phi + \chi_{z'z'z'} \sin^2 \phi \right] \right|^2 \quad (2.36)$$

In the specific case of z-cut quartz, the following equalities emerge by symmetry: $\chi_{z'z'z'} = -\chi_{z'x'x'} = -\chi_{x'x'z'}$. Substitution of this equality into Eq. (2.36) yields the simple two-parameter expression for the anticipated SHG produced for a z-cut quartz sample rotated an angle ϕ_0 driven by horizontally polarized incident light given in Eq. (2.37), with the same the proportionality constant C as shown in (2.31).

$$I^{2\omega}(\phi, \phi_{pol}) = C \cdot \sin^2(3\phi - \phi_{pol}) \quad (2.37)$$

2.2.5 Derivation of tilt angle θ

In order to illustrate the effect of polar tilt angle of collagen fiber, a mathematical relation between measured laboratory frame ratio (ρ), local frame ratio (ρ_l) and polar tilt angle (θ) was derived by projecting local tensor element onto the lab frame.²¹ The projected laboratory frame tensors χ_{XXX} and χ_{XYX} are shown in Eqs. (2.38) and (2.39) respectively, where $\chi_{z'z'z'}$ and $\chi_{z'x'x'}$ are local frame tensors.

$$\chi_{XXX} = \chi_{z'z'z'} \cdot \sin^3 \theta + 3\chi_{z'x'x'} \cdot \sin \theta \cdot \cos^2 \theta \quad (2.38)$$

$$\chi_{XYX} = \chi_{z'x'x'} \cdot \sin \theta \quad (2.39)$$

The laboratory frame tensor ratio (ρ) is defined as $\rho \equiv \chi_{XXX} / \chi_{XYX}$, which can be described as Eq. (2.40).

$$\rho = \frac{\chi_{XXX}}{\chi_{XYX}} = \frac{\chi_{z'z'z'} \cdot \sin^3 \theta + 3\chi_{z'x'x'} \cdot \sin \theta \cdot \cos^2 \theta}{\chi_{z'x'x'} \cdot \sin \theta} \quad (2.40)$$

Since the local frame tensor ratio is defined as $\rho_l \equiv \chi_{z'z'z'} / \chi_{z'x'x'}$. Calculations of tilt angle θ for a specific chromophore can be simplified as Eq.(2.41).

$$\sin^2 \theta = \frac{\rho - 3}{\rho_l - 3} \quad (2.41)$$

2.3 Experimental Methods

SHG measurements were performed with a custom-built microscope.⁵ Briefly, an 80 MHz 100 fs MaiTai Ti:sapphire laser (SpectraPhysics) at 800 nm was used as incident light source. The beam was scanned across the sample using a resonant scanning mirror at 8.8 kHz (EOPC) for the fast-scan axis synchronized to the laser, and a galvanometer mirror (CambridgeTech) for the slow-scan. Then the beam was expanded through a pair of lens and focused with various objectives (10 \times , 0.3 NA; and 20 \times , 0.4 NA; Nikon) with average power between 40 - 80 mW on the sample. For depolarized incident light, a depolarizer (DPP-25B, Thorlabs) was placed in the collimated path after the beam expansion and before the excitation objective (*Figure 2.2*). SHG from the sample was collected through a 10 \times , 0.3 NA OPTEM condenser and separated from the fundamental light using a dichroic mirror in the transmitted direction. A Glan-Taylor polarizer was placed in a rotation stage before a photomultiplier tubes (PMT, Hamamatsu H12310-40)

with bandpass filters (HQ 400/20m-2p; Chroma Technology) for the SHG detection. Polarization dependent SHG measurements were conducted via mechanical rotation of the polarizer from 0 to π rad (ϕ_{pol}) with 60 intervals illuminated with both a purely polarized and a depolarized incident beam.

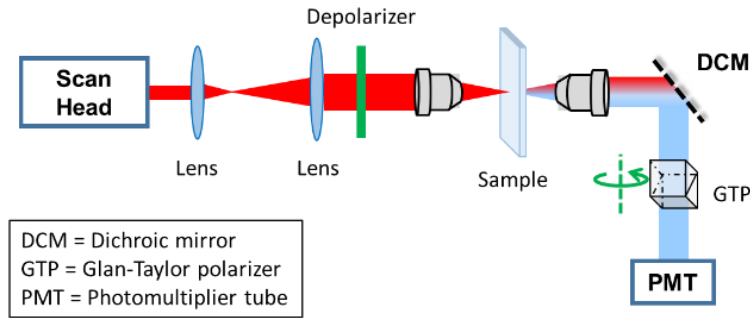


Figure 2.2 SHG transmittance microscope capable of delivering both a purely polarized and a depolarized fundamental beam.

As a prelude to more complex samples, the SHG produced from z-cut quartz (500 μm thick) was measured to assess the predictions for a model system with well-established nonlinear optical properties exhibiting no birefringence for light propagating parallel to the z-axis. Measurements of polarization-dependent SHG from collagen were performed using a 20 \times , 0.4 NA Nikon objective with mouse tails gifted from Prof. Philip Low (Purdue University, West Lafayette, IN). Mouse tails were first decalcified in the solution of 23% formic acid, 4% formalin, and 1% methanol for 2 hours, then sectioned longitudinally to ensure that sections were retrieved from the central region of the tail. For the SHG imaging, the mouse tail section was then fixed in 10% formalin and embedded in paraffin prior to microtoming into 4 μm thick slides.

2.4 Results and discussion

Polarization-dependent SHG produced from purely vertically polarized incident light with z-cut quartz was shown in *Figure 2.3*. The SHG intensities integrated over the whole FoV was fit to Eq. (2.37), relating to the detected polarization angle, ϕ_{pol} in *Figure 2.3(A)*, or the quartz orientation angle, azimuthal angle ϕ , *Figure 2.3(B)*). Good agreement between the fitted curve (green lines) and experiment intensity (blue markers) for the SHG detected was observed, with

the three-fold higher periodicity in azimuthal angle as a direct consequence of the 3-fold rotational symmetry of z-cut quartz with purely polarized incident light.

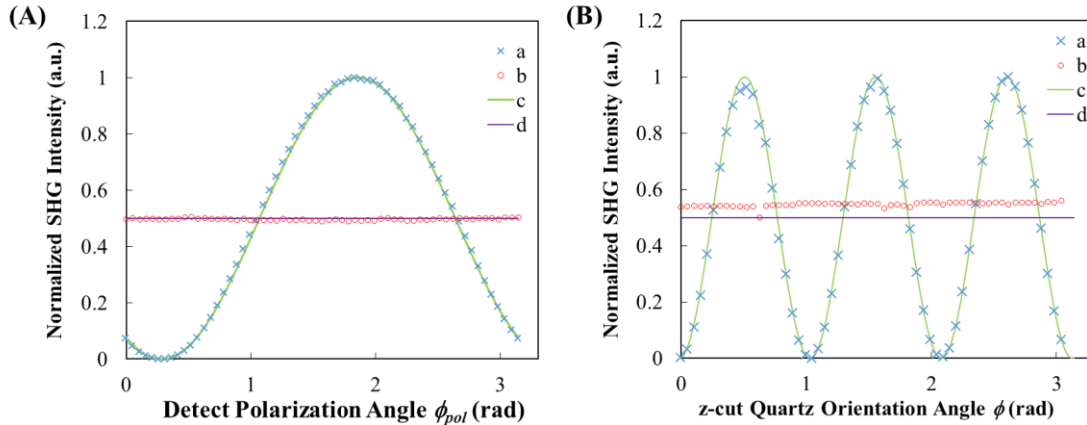


Figure 2.3 Polarization dependent SHG measurements with pure polarized and/or depolarized light with theoretical predictions. (A) Polarization dependent measurement of SHG signal from z-cut quartz at an arbitrary angle under (a) vertically polarized and (b) depolarized incident light overlay with theoretical (c) fitting and (d) prediction. (B) Measurements of horizontally polarization SHG signals from z-cut quartz at different azimuthal angle under (a) vertically polarized and (b) depolarized incident light, with theoretical (c) fitting and (d) prediction.

For SHG produced by z-cut quartz for a depolarized incident beam, the ratio $\rho = -1$ by symmetry, Eq. (2.31) predicts the production of SHG intensity that is completely independent of both the polarizer rotation angle ϕ_{pol} and quartz orientation angle ϕ . The outcome is consistent with the production of entirely unpolarized SHG from z-cut quartz, with intensity equal to half the amplitude observed from the purely polarized source. The prediction result based on the observed trends for the polarized source is shown in purple lines in *Figure 2.3(A)*, together with the experimental observations (red dots) as ϕ_{pol} is varied. As shown in the figure, the measurements are in excellent agreement with the theoretical prediction. Analogous measurements performed as a function of ϕ with a fixed detector polarization rotation angle ϕ_{pol} and z-cut quartz rotation showed similar agreement between theory and experiments, as shown in *Figure 2.3(B)*. Although the depolarized result yields a slight offset from predictions based on the polarized measurements, the overall independence of the SHG measured through a fixed polarizer as a function of the quartz rotation angle was consistent with the expectations from the theoretical predictions. The observed offset was tentatively attributed to uncertainty in the

amplitude determined from the fits of the traces observed with a purely polarized input. The excellent overall agreement between theory and experiments generally supports the validity of the mathematical framework and its approximations for describing the coherent process of SHG driven by partially or wholly depolarized light.

SHG produced from collagen within a longitudinally sectioned mouse tail was analyzed with depolarized incident light. The local fiber orientations (ϕ) and tensor ratios (ρ) were then retrieved for every SHG-active pixel by fitting the intensity trend as a function of ϕ_{pol} described in Eq. (2.31). From the per-pixel fitting, the azimuthal angle of collagen was determined at a per-pixel basis for each location exhibiting sufficient signal to noise to allow statistically significant polarization analysis, shown in *Figure 2.4(A)*. Unlike the case for z-cut quartz, the polarization-dependent SHG produced from a depolarized fundamental beam generally exhibited SHG with strong polarization preferences, consistent with Eq. (2.31) for $|\rho| \neq 1$. A representative fit is shown in *Figure 2.4(D)*.

The local azimuthal orientations of the collagen fibers were also independently determined by *OrientationJ*, a plugin for image directional analysis for *ImageJ*.^{22, 23} *Figure 2.4(A)* demonstrates the intensity-weighted orientation map retrieved via pixel-by-pixel nonlinear fit, contrasted with the orientation map recovered by *OrientationJ* in *Figure 2.4(B)*. Good agreement between the two methods was observed for local azimuthal orientations. *Figure 2.4(C)* shows an overlay of histogram of orientation angles recovered via both methods. It is worth noting that *OrientationJ* assigns orientation based entirely on image analysis relying on context from adjacent pixels. As such, the two methods for determining azimuthal orientation (single pixel polarization analysis and contextual image analysis) are orthogonal methods yielding comparable outcomes.

Several possible explanations may account for the subtle but nonzero deviations between fiber orientation angles determined by polarization analysis versus image analysis (*OrientationJ*). First, the depolarizer functions by imposing a sinusoidal modulation of the polarization state across the physical expanse of the collimated beam. Upon passing this beam through the objective, the spatial Fourier transform of a sinusoidal modulation results in a horizontally offset dual-spot point spread function within the FoV, which in turn produces a double image. The SHG produced from a depolarized source should contain equal contributions from both foci in

order to be considered as genuinely depolarized. Spatial variation across the FoV may significantly influence the validity of this assumption, given that the fiber thickness is generally small relative to the displacement. Polarization analysis performed for both vertically and horizontally aligned collagen regions were compared to assess the potential impact of the double-beam in polarization analysis. Given that the offset is solely along the horizontal axis, perturbations from the double-focus should be significantly more pronounced for vertically oriented fibers. From inspection of the images, comparable deviations were observed for both horizontally and vertically aligned fibers, suggesting the absence of obvious systematic bias from the particular manner in which the beam was rendered unpolarized in the present study.

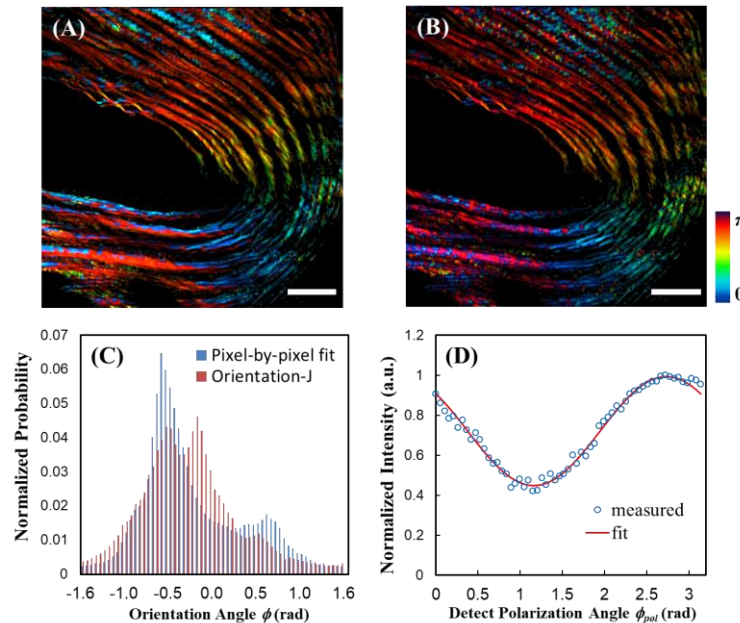


Figure 2.4 Orientation images of the azimuthal angle for a single FoV of mouse tail section from (A) the pixel-by-pixel nonlinear fit analysis and (B) *OrientationJ*. Scale bar: 100 μm . (C) The histogram of the orientation distribution achieved from pixel-by-pixel fit and *OrientationJ*. (D) Nonlinear fitting results of depolarized light excitation SHG for signal random pixel.

In addition to recovering the azimuthal angle, the polarization-dependent SHG generated from an unpolarized source also allows recovery of the measured laboratory-frame ratio ρ through Eq. (2.31), with representative images are shown in *Figure 2.5(A)*. The modal value of $\rho = 1.69$ as marked in *Figure 2.5(C)* is consistent with several other previous reports^{4, 24} for mouse tail and other collagenous assemblies such as chicken wing and human dermis. Deviations

between polarization analysis and image analysis may arise from the implicit assumption that the fibers exhibit polar tilt angles of $\pi/2$, such that the fibers are assumed to align perfectly within the FoV. In practice, any thin section is generally expected to transect a given fiber at a nonzero polar angle θ . Whereas the image analysis methods such as demonstrated using *OrientationJ* can independently inform azimuthal orientation, polar tilt remains a challenge. Fortunately, the polarization-dependent SHG may provide a route for accessing polar tilt angle, provided the value of ρ can be independently measured or assumed.

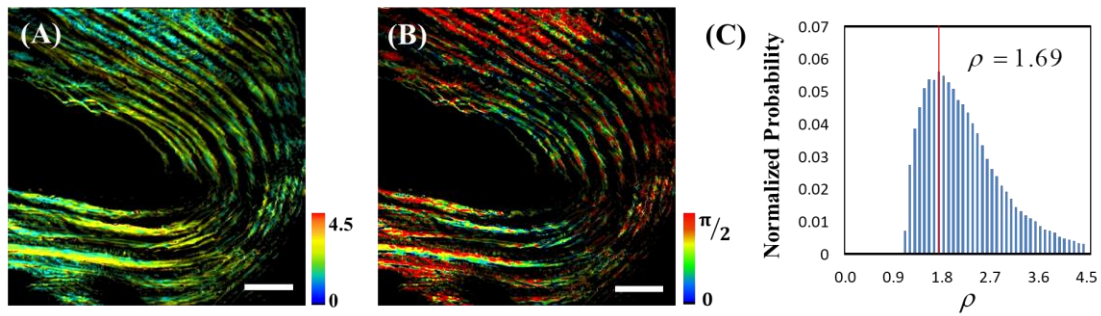


Figure 2.5 The laboratory-frame ratio ρ and polar tilt angle a single FoV of mouse tail section from the per-pixel fit analysis. (A) The measured laboratory-frame ratio ρ images. (B) The polar tilt angle θ image recovered from the measured laboratory-frame ratio ρ for the same FoV with $\rho_l = 1.7$. (C) The distribution of the ratio ρ , with the maximum peak marked at 1.69. Scale bar: 100 μm .

Using literature values for the local-frame ratio ρ_l (i.e., relative to the long-axis of an individual collagen fiber), a mathematical relation between measured laboratory-frame ratio (ρ), the local-frame ratio ρ_l , and the polar tilt angle (θ) can be calculated using Eq. (2.41) by projecting local tensor element onto the lab frame²¹. A per-pixel fit was performed to recover a map of polar tilt angle θ with the assumption of a local-frame hyperpolarizability ratio $\rho_l = 1.7$ based on previously reported values in which the range of polar tilt angle at each pixel was determined experimentally.^{4, 15} This value of the local-frame ratio for collagen fibers is quite similar to the most probable ratio observed experimentally, shown in *Figure 2.5(C)*, consistent with an assembly in which the most probable collagen orientation is lying flat within the field of view. Under this assumption, the observed values of ρ was used to recover the polar tilt angle at

each pixel through Eq. (2.41). The recovered map of polar tilt angle θ was shown in *Figure 2.5(B)*. A significant portion of collagen fibers was tilted out of the detection plane (i.e., $\theta \neq \pi/2$). This phenomenon was more obvious in the region where collagen fibers bend. The measurements likely contain an implicit bias against tilt angles of $\theta \cong 0$, as fibers aligned parallel with the optical access are symmetry-forbidden for production of coherent SHG. The results shown in *Figure 2.5* are largely insensitive to the particular assumed value of ρ_l , yielding qualitatively similar results when assuming $\rho_l = 1.4$, consistent with other reports for the local-frame tensor element ratio^{4, 15}.

2.5 Conclusion

The results of this study have intriguing implications on polarization-analysis of depolarizing systems. A Mueller tensor framework was utilized to predict the polarization of SHG stimulated with depolarized light. This framework has been verified experimentally with z-cut quartz and collagenous tissue under depolarized incident light. From a practical standpoint, the intentional use of depolarized incident light has the distinct advantage of providing measurements that are immune to subsequent depolarization of the fundamental beam. Despite the loss of information from scrambling of the incident polarization, analysis of collagenous tissue with depolarized SHG still allowed determination of both collagen azimuthal and polar orientation from the laboratory-frame tensor elements. The use of unpolarized incident light may significantly simplify polarization analysis in thick tissue sections for measurement in transmission.

2.6 References

1. Campagnola, P. J.; Loew, L. M., Second-harmonic imaging microscopy for visualizing biomolecular arrays in cells, tissues and organisms. *Nature Biotechnology* **2003**, *21* (11), 1356-1360.
2. Stoller, P.; Reiser, K. M.; Celliers, P. M.; Rubenchik, A. M., Polarization-modulated second harmonic generation in collagen. *Biophys J* **2002**, *82* (6), 3330-42.
3. Gusachenko, I.; Tran, V.; Goulam Houssen, Y.; Allain, J. M.; Schanne-Klein, M. C., Polarization-resolved second-harmonic generation in tendon upon mechanical stretching. *Biophys J* **2012**, *102* (9), 2220-9.

4. Dow, X. Y.; DeWalt, E. L.; Sullivan, S. Z.; Schmitt, P. D.; Ulcickas, J. R.; Simpson, G. J., Imaging the Nonlinear Susceptibility Tensor of Collagen by Nonlinear Optical Stokes Ellipsometry. *Biophys J* **2016**, *111* (7), 1361-1374.
5. DeWalt, E. L.; Sullivan, S. Z.; Schmitt, P. D.; Muir, R. D.; Simpson, G. J., Polarization-modulated second harmonic generation ellipsometric microscopy at video rate. *Anal Chem* **2014**, *86* (16), 8448-56.
6. Schmitt, P. D.; DeWalt, E. L.; Dow, X. Y.; Simpson, G. J., Rapid Discrimination of Polymorphic Crystal Forms by Nonlinear Optical Stokes Ellipsometric Microscopy. *Anal Chem* **2016**, *88* (11), 5760-5768.
7. Petralli-Mallow, T.; Wong, T. M.; Byers, J. D.; Yee, H. I., Circular dichroism spectroscopy at interfaces: a surface second harmonic generation study. *Journal of physical ...* **1993**.
8. Tiaho, F.; Recher, G.; Rouede, D., Estimation of helical angles of myosin and collagen by second harmonic generation imaging microscopy. *Opt. Express* **2007**.
9. Amat-Roldan, I.; Psilodimitrakopoulos, S., Fast image analysis in polarization SHG microscopy. *Optics ...* **2010**.
10. Gusachenko, I.; Latour, G.; Schanne-Klein, M. C., Polarization-resolved Second Harmonic microscopy in anisotropic thick tissues. *Opt Express* **2010**, *18* (18), 19339-52.
11. Nadiarnykh, O.; Campagnola, P. J., Retention of polarization signatures in SHG microscopy of scattering tissues through optical clearing. *Optics express* **2009**.
12. Samim, M.; Krouglov, S.; Barzda, V., Nonlinear Stokes-Mueller polarimetry. *Phys Rev A* **2016**.
13. Shi, Y. M.; McClain, W. M.; Harris, R. A., An Extension of the Mueller Scattering Matrix to Nonlinear Light-Scattering. *Chem Phys Lett* **1993**, *205* (1), 91-95.
14. Shi, Y. M.; McClain, W. M.; Harris, R. A., Generalized Stokes-Mueller Formalism for 2-Photon Absorption, Frequency-Doubling, and Hyper-Raman Scattering. *Phys Rev A* **1994**, *49* (3), 1999-2015.
15. Burke, M.; Golaraei, A.; Atkins, A.; Akens, M.; Barzda, V.; Whyne, C., Collagen fibril organization within rat vertebral bone modified with metastatic involvement. *J Struct Biol* **2017**, *199* (2), 153-164.
16. Cisek, R.; Tokarz, D.; Steup, M.; Tetlow, I. J.; Emes, M. J.; Hebelstrup, K. H.; Blennow, A.; Barzda, V., Second harmonic generation microscopy investigation of the crystalline ultrastructure of three barley starch lines affected by hydration. *Biomed. Opt. Express* **2015**, *6* (10), 3694-3700.
17. Simpson, G. J., Connection of Jones and Mueller Tensors in Second Harmonic Generation and Multi-Photon Fluorescence Measurements. *J Phys Chem B* **2016**, *120* (13), 3281-302.
18. Azzam, R. M. A.; Bashara, N. M., *Ellipsometry and Polarized Light*. Elsevier: Amsterdam, 1987.

19. de Wergifosse, M.; de Ruyck, J.; Champagne, B., How the Second-Order Nonlinear Optical Response of the Collagen Triple Helix Appears: A Theoretical Investigation. *J Phys Chem C* **2014**, *118* (16), 8595-8602.
20. Dow, X. Y.; DeWalt, E. L.; Newman, J. A.; Dettmar, C. M.; Simpson, G. J., Unified Theory for Polarization Analysis in Second Harmonic and Sum Frequency Microscopy. *Biophys J* **2016**, *111* (7), 1553-1568.
21. Moad, A. J.; Simpson, G. J., A Unified Treatment of Selection Rules and Symmetry Relations for Sum-Frequency and Second Harmonic Spectroscopies. *The Journal of Physical Chemistry B* **2004**, *108* (11), 3548-3562.
22. Schneider, C. A.; Rasband, W. S.; Eliceiri, K. W., NIH Image to ImageJ: 25 years of image analysis. *Nat Methods* **2012**, *9* (7), 671-5.
23. Puspoki, Z.; Storath, M.; Sage, D.; Unser, M., Transforms and Operators for Directional Bioimage Analysis: A Survey. *Adv Anat Embryol Cell Biol* **2016**, *219*, 69-93.
24. Chen, W.; Li, T.; Su, P.; Chou, C.; Fwu, P. T.; Lin, S.; Kim, D.; So, P. T. C.; Dong, C., Second harmonic generation χ tensor microscopy for tissue imaging. *Applied Physics Letters* **2009**, *94* (18), 183902.

CHAPTER 3. LOCAL-FRAME TENSOR ELEMENTS RECOVERY FOR POLARIZATION DEPENDENT ANALYSIS OF THICK TISSUES

A version of this chapter has been published by International Society for Optics and Photonics, 2019. Reprint permission from James RW Ulcickas, Changqin Ding, Garth J Simpson, *Multiphoton Microscopy in the Biomedical Sciences XIX*, vol. 10882, p. 1088217. International Society for Optics and Photonics, 2019.

The framework demonstrated in CHAPTER 2 was used to reduce the number of potentially unique parameters from 64 in the general Mueller tensor to as few as 2 in polarization dependent second harmonic generation (SHG) analysis of collagen tissue. Local-frame tensor elements in thick, partially depolarized tissues were recovered without substantial increase in mathematical complexity compared to conventional polarization-dependent nonlinear optical imaging. The results proved the ability of this relatively simple but mathematically rigorous framework for studies of integrating partial depolarization effects in biological imaging, supporting polarization analysis in broad classes of samples.

3.1 Introduction

The widespread adoption of SHG as a widespread tool for biological imaging is driven largely by two factors: the ability to produce high-resolution images despite high sample turbidity, and the relative ease of the measurements. The polarization-dependence of the detected SHG is highly sensitive on the incident polarization and the molecular/macromolecular properties of the nonlinear optically active source. Consequently, polarization-dependent SHG microscopy is intrinsically sensitive to local order, as demonstrated for characterization of biostructures¹⁻⁷, protein crystals⁸, and active pharmaceutical ingredients^{8,9}.

The ability to image deeply in turbid biological media is a challenge in accessing the rich molecular-scale structural information from polarization analysis in SHG. In the most common beam-scanning instrumentation, the nonlinear scaling of SHG with incident intensity suppresses nonlinear optical interactions outside the focal plane, in which the beam is unfocused^{10, 11}. As a consequence, scattering losses may attenuate the beam, but still produce high resolution images from the “ballistic” component of light capable of traversing directly to the focal plane. However, the ballistic unscattered light is not generally purely polarized. If different cross sectional regions

of the unfocused beam experience different phase delays or local birefringence prior to arrival at the sample plane, the net sum of these collective contributions may result in partially or wholly depolarized incident light. The partial depolarization routinely raised in tissue imaging is incompatible with standard Jones tensor formulations for polarization analysis of SHG. In CHAPTER 2, a more general Mueller tensor mathematical framework supports compatibility with partially or wholly depolarized incident light is promoted. In this Chapter, polarization dependent SHG analysis was used for thick sample analysis with partial polarization lost in the incident light due to the scattering in the sample. The Mueller/Jones connecting framework recovered the similar local-frame tensor elements relative to the thin sample analysis with pure polarized incident light/driving field.

3.2 Theoretical foundation

As detailed in CHAPTER 2, Eq. (3.1) allows the general Mueller matrix to be fully described and generated from the smaller set of Jones tensor elements. The 64 elements within the general Mueller tensor can be populated from the set of eight nonzero and six unique elements in Jones tensor with either purely polarized or partially polarized incident light.

$$M^{(2)} = A \cdot \left(\chi_J^{(2)*} \otimes \chi_J^{(2)} \right) : A^{-1} A^{-1} \quad (3.1)$$

The number of unique elements in the Jones tensor can be further reduced when considering the symmetry and laboratory-frame orientation of a specific sample. For SHG measurements of collagen tissue with the z' -axis defined along the local collagen fiber axis, only two unique nonzero tensor elements dominate in the local frame of collagen tissue: $\chi_{z'z'z'}$ and $\chi_{z'x'x'} \cong \chi_{x'x'z'} = \chi_{x'z'x'}$ ^{12, 13}, due to the relatively small magnitude of $\chi_{x'y'z'}$ tensor elements by *ab initio* calculations¹²⁻¹⁴. Furthermore, SHG from the $\chi_{x'y'z'}$ contribution is forbidden within the paraxial approximation for fibers lying parallel with the image plane. Given the case of collagen local symmetry, the knowledge of collagen fiber orientation enables recovery of the full 64 element Mueller tensor from only two unique input parameters: $\chi_{z'z'z'}$ and $\chi_{z'x'x'}$.

It is challenging to generate simple form solutions to recover the Jones tensor elements from partially polarized light, since the particular form for the Stokes vector of the fundamental beam may not be trivially described in the most general case. However, if the Stokes vector at the

sample plane is known or can be independently determined. The Stokes vector of the SHG is related to Mueller tensor and connected to the Jones tensor through Eq. (3.1). With the knowledge of the azimuthal (and potentially polar) orientation of the fiber, the laboratory frame Jones tensor $\chi_J^{(2)}$ can be related back to the local-frame tensor $\chi_l^{(2)}$ of the fiber through rotation matrices on a per-pixel basis as shown in Eq. (3.2).

$$\begin{aligned}\chi_J^{(2)} &= R(\phi) \cdot \chi_l^{(2)} : R^{-1}(\phi) R^{-1}(\phi) \\ R(\phi) &= \begin{bmatrix} \cos \phi & \sin \phi \\ -\sin \phi & \cos \phi \end{bmatrix}; R^{-1}(\phi) = R(-\phi)\end{aligned}\quad (3.2)$$

With the equations above and the mathematical framework mentioned in CHAPTER 2, the anticipated Stokes vector of SHG produced by collagen can be predicted for any partially polarized incident field with an assumed set of local-frame tensor elements. With the given collagen azimuthal orientation angle ϕ , the most probable set of nonzero local-frame tensor elements $\hat{\chi}_l^{(2)}$ (e.g., $\hat{\chi}_{z'z'z'}$ and $\hat{\chi}_{z'x'x'}$, with the “hat” indicating a maximum likelihood estimate) can be recovered by minimizing the sum of squared deviations between the predicted and measured Stokes vectors obtained for N ($N \geq 1$) partially polarized input beams. Eq. (3.3) expresses a general form consistent with an arbitrary number (N) of polarization-dependent measurements for generality and compatibility with the experiments.

$$\hat{\chi}_l^{(2)} = \arg \min_{\chi_l^{(2)}} \left[\sum_{i=1}^N \left\| \mathbf{s}_{meas}^{2\omega} - \mathbf{s}_{calc}^{2\omega}(\chi_l^{(2)}, \phi) \right\|_{s_i^\phi}^2 \right] \quad (3.3)$$

3.3 Methods

SHG measurements were performed based on a custom-built beam scan microscope,⁸ with the polarization dependent optical elements depicted schematically in *Figure 3.1*. In brief, an 80 MHz 100 fs MaiTai Ti:sapphire laser (SpectraPhysics) was tuned at 800 nm coupled with an 8 MHz electro-optic modulator (EOM). The EOM was clocked by the laser to generate precisely ten unique polarizations in one period of the EOM. An 8.8 kHz resonant mirror (EOPC) and a galvanometer mirror (CambridgeTech) synchronized to the laser were used for the low and fast-scan axis, respectively. The Stokes vectors for the transmitted fundamental and the generated SHG was detected by passing the beam through a wave plate (WP) with a quarter-wave retardance at 400 nm (eight-wave retardance at 800 nm), followed by a broadband wire grid

polarizer. A dichroic mirror separated the fundamental 800 nm from the SHG so that they were simultaneously detected by a photodiode and photomultiplier tube (PMT), respectively.

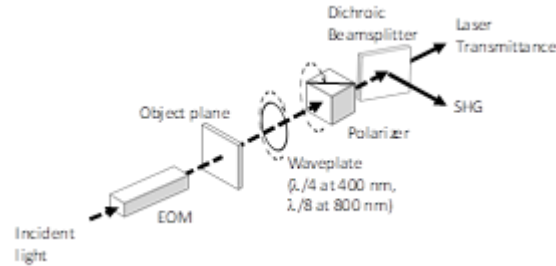


Figure 3.1 Schematic of the polarization-dependent components in the SHG microscope. Stokes vectors for both the laser transmittance and the SHG were measured from the intensities recorded at several combinations of waveplate and polarizer rotation angles. A Stokes vector for each wavelength at each pixel was generated for each of the 10 unique polarization states produced in one period of the EOM.

To recover the precise Stokes vector at the partially depolarized sample plane, twelve sets of the one-period 10 polarization images were acquired with the rotation angle of WP (γ) at 0° , 22.5° , and 45° and 0° , 45° , 90° , and 135° for the polarizer rotation angle (ϕ_{pol}), yielding a total of 120 images per detector, and 240 total (for both transmittance and SHG). For a given combination of WP and polarizer rotation angle, the integration time for acquisition of a complete set of 10 images was 10 s, corresponding to an average single-pixel integration time of $\sim 40 \mu\text{s}$ for a given polarization-dependent frame. This process was repeated for all twelve combinations of WP and polarizer rotation angles to recover the Stokes vectors of the fundamental and SHG for a total per-pixel analysis time of $< 0.5 \text{ ms}$ (~ 2 minutes for total data acquisition time, and an additional ~ 5 minutes for optics rotation).

The Stokes vectors can be generated by directly measuring the elements illustrated in Eq. (3.4), with I_H , I_V , $I_{\pm 45^\circ}$, I_R , and I_L are the intensities recorded for horizontally, vertically, $\pm 45^\circ$ linearly, right and left circularly polarized components, respectively. However, the direct measurements of these elements required separate analyzing optics set for either the SHG or the transmittance. The WP used was optimized for quarter wave retardance of 400 nm, corresponding to eighth wave retardance of the fundamental.

$$\bar{s} = \begin{bmatrix} s_0 \\ s_1 \\ s_2 \\ s_3 \end{bmatrix} = \begin{bmatrix} I_H + I_V \\ I_H - I_V \\ I_{+45^\circ} - I_{-45^\circ} \\ I_R - I_L \end{bmatrix} \quad (3.4)$$

The Stokes vector at the sample plane is presented by casting the Mueller matrix of waveplate and polarizer with a final form as shown in Eq. (3.5), in which i is the i th combination of waveplate and polarizer angle, s_{out} is the exit light from the sample plane, and M_{pol}^0 and M_{WP}^0 are the Mueller matrix of waveplate and polarizer at 0° , respectively. The detected intensity is contained only in the first element of the Stokes vector in the reference frame of the polarizer.

$$I_{det,i} = [1 \ 0 \ 0 \ 0] \cdot [M_{pol}^0 \cdot R(\phi_{pol})_i] \cdot [R(\gamma)_i \cdot M_{WP}^0 \cdot R(\gamma)_i] \cdot s_{out} \quad (3.5)$$

For each pixel in the field of view, the intensity measured with Eq. (3.5) was repeated for all combinations of the WP and polarizer rotation angle to generate a 12-element vector of intensity I_{det} . The maximum likelihood estimate (MLE) for the Stokes vector \hat{s}_{out} at the sample plane was recovered by the fitting to Eq. (3.6) with the assumption that no additional depolarization occurs after the sample. The difference of the 12×4 fit matrix F between the fundamental and SHG images were the retardance difference in the waveplate M_{WP} .

$$I_{det} = F \cdot s_{out} \Rightarrow \hat{s}_{out} = (F^T \cdot F)^{-1} \cdot F^T \cdot I_{det} \quad (3.6)$$

3.4 Results

Collagen-rich tissue sections with $\sim 40 \mu\text{m}$ thickness of rat tail tendon were used as the sample as implementation. The polarization state of both the fundamental and SHG from the focal planes were characterized simultaneously. As described in *Section 3.3*, a set of images were generated under 12 combination of waveplate and polarizer angle for each incident polarization state of the EOM for both transmittance bright field (BF) and SHG, as shown in *Figure 3.2(A)*. The Stocks vector for both BF and SHG were recovered for each incident polarization state. *Figure 3.2(C)* indicated the fiber orientation map of the collagen tissue recovered from the bright field images. The most probable set of local-frame tensor elements in $\hat{\chi}_i^{(2)}$ were retrieved according to the fiber orientation and the recovered Stocks vector for each measurement, as shown in *Figure 3.2(D)* in which $\hat{\chi}_{z'z'z'}$ was marked as red and $\hat{\chi}_{z'x'x'}$ as blue.

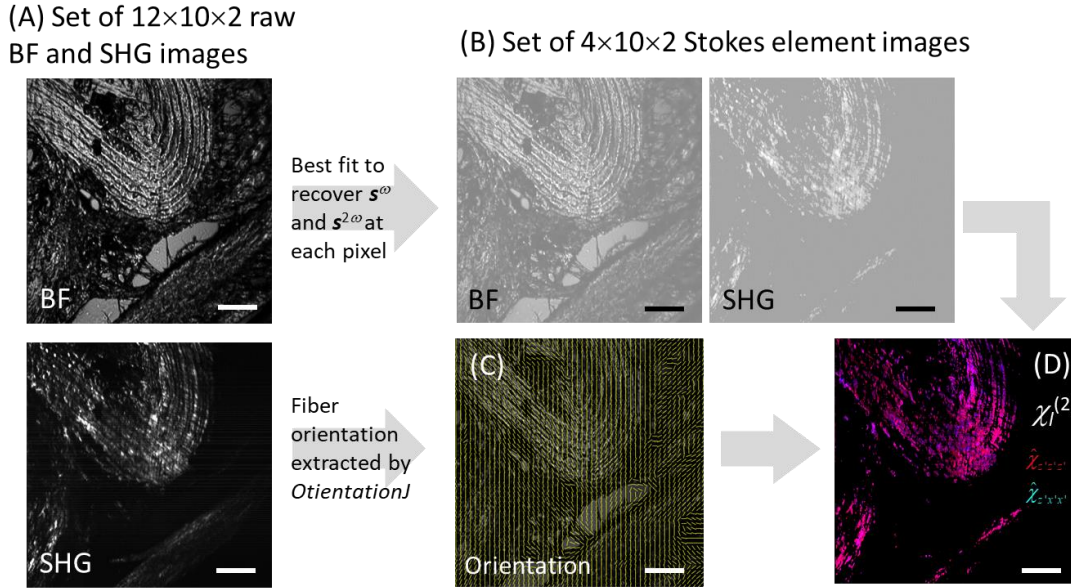


Figure 3.2 Flow diagram for tensor recovery in partially depolarizing media: (A) Initial images from the combined stack of 240 transmittance and SHG raw images. (B) Transmittance and SHG fits of the raw data enable recovery of the Stokes vectors for ω and 2ω at each pixel for each of the 10 incident polarizations in one EOM period. (C) Fiber orientation (azimuthal angle) recovered by using *OrientationJ*. (D) Recovered local-frame tensor elements of collagen by using the azimuthal orientation from (C) and the Stokes vectors from (B) by using Eq. (3.3). Scale bar: 50 μm .

The degree of depolarization (DoP) of the incident driving fields at the sample was defined in Eq. (3.7), so that purely polarized field has the value $\text{DoP} = 1$ and totally depolarized field has the value $\text{DoP} = 0$.¹⁵

$$\text{DoP} = \sqrt{s_1^2 + s_2^2 + s_3^2} / s_0 \quad (3.7)$$

The DoP of the fundamental beam at the sample plane of a $\sim 40 \mu\text{m}$ thick section of rat tail tendon was shown in *Figure 3.3(A)*, with the histograms shown in *Figure 3.3(B)*. The histogram of DoP highlighted the substantial reduction in polarization purity arising by passing through the $\sim 40 \mu\text{m}$ thick tissue section. Partial depolarization of the fundamental beam with $\text{DoP} < 0.9$ arises in the large majority of pixels, with a mean DoP of 0.81 and a standard deviation of 0.14. Compared with the incident field, the SHG signals had more depolarization effects as the average DoP of the SHG was 0.41 with a standard deviation of 0.18, with most pixels exhibiting $\text{DoP} < 0.5$. Because the Stokes vectors for the fundamental field were evaluated within the focal plane, all effects related to birefringence, scattering, and depolarization were implicitly included

through the Stokes vector analysis. In this case, the use of the Jones/Mueller connecting framework provided the comparative simplified description of partially depolarized light.

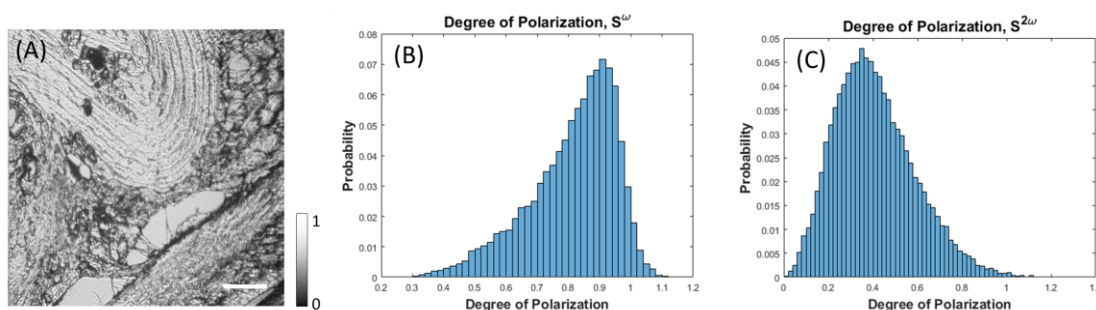


Figure 3.3 The DoP measured in transmission through a ~40 μm thick section of rat tail tendon. (A) is the color map with the histograms for the fundamental transmittance (B) and the SHG (C). Scale bar: 50 μm.

The accuracy of the recovered local-frame tensor elements were compared with the measurements obtained from thin sections with negligible incident polarization. The histogram of tensor element ratios was shown in *Figure 3.4* with reasonably good agreement with the previous reported values ranging from 1.1 to 2.4 for the ratio from thin film sections.^{5, 16-20} The results demonstrated in this Chapter show the potential of routine polarization analysis of thick samples and scattering materials which are currently inaccessible by conventional polarization dependent nonlinear optical methods. The mathematical connections between the Jones and Mueller tensor enabled analyses without increase in complexity in describing the local-frame nonlinear optical response relative to analyses with purely polarized incident light.

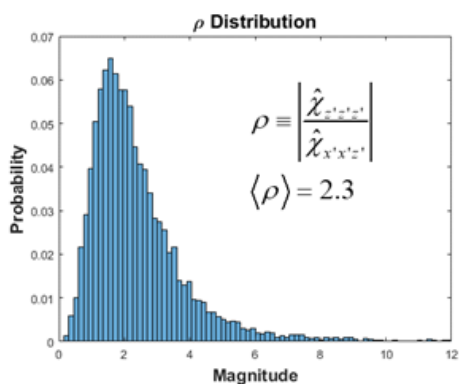


Figure 3.4 Histogram of the tensor element ratios recovered for SHG imaging of collagen with partially depolarized incident light.

3.5 Conclusion

The mathematical framework connecting Mueller and Jones frames was experimentally used in polarization-dependent analyses of thick tissue sections exhibiting partial depolarization. This method required no substantial increases in complexity relative to conventional polarization analysis using purely polarized incident light for thin samples. The polarization-dependent SHG analyses were performed to a relatively thick (40 μm) tissue section with substantial depolarization of the fundamental field prior to arrival at the focal plane. The local-frame tensor elements in the FoV were recovered on per-pixel basis with the similar values to those produced with think tissue section and pure polarized incident field. However, the reduction of the data acquisition time (~ 2 min in total) can further improve the signal to noise ratio of the measurements and improve the application of this analysis, such as polarization-dependent nonlinear optical microscopy in live animal imaging.

3.6 References

1. Campagnola, P. J.; Loew, L. M., Second-harmonic imaging microscopy for visualizing biomolecular arrays in cells, tissues and organisms. *Nature Biotechnology* **2003**, *21* (11), 1356-1360.
2. Stoller, P.; Reiser, K. M.; Celliers, P. M.; Rubenchik, A. M., Polarization-modulated second harmonic generation in collagen. *Biophys J* **2002**, *82* (6), 3330-42.
3. Gusachenko, I.; Tran, V.; Goulam Houssen, Y.; Allain, J. M.; Schanne-Klein, M. C., Polarization-resolved second-harmonic generation in tendon upon mechanical stretching. *Biophys J* **2012**, *102* (9), 2220-9.
4. Dow, X. Y.; DeWalt, E. L.; Sullivan, S. Z.; Schmitt, P. D.; Ulcickas, J. R.; Simpson, G. J., Imaging the Nonlinear Susceptibility Tensor of Collagen by Nonlinear Optical Stokes Ellipsometry. *Biophys J* **2016**, *111* (7), 1361-1374.
5. Mansfield, J. C.; Mandalia, V.; Toms, A.; Winlove, C. P.; Brasselet, S., Collagen reorganization in cartilage under strain probed by polarization sensitive second harmonic generation microscopy. *Journal of the Royal Society Interface* **2019**, *16* (150).
6. Golaraei, A.; Mirsanaye, K.; Ro, Y.; Krouglov, S.; Akens, M. K.; Wilson, B. C.; Barzda, V., Collagen chirality and three-dimensional orientation studied with polarimetric second-harmonic generation microscopy. *Journal of Biophotonics* **2019**, *12* (1).
7. Campbell, K. R.; Chaudhary, R.; Handel, J. M.; Patankar, M. S.; Campagnola, P. J., Polarization-resolved second harmonic generation imaging of human ovarian cancer. *Journal of Biomedical Optics* **2018**, *23* (6).

8. DeWalt, E. L.; Sullivan, S. Z.; Schmitt, P. D.; Muir, R. D.; Simpson, G. J., Polarization-modulated second harmonic generation ellipsometric microscopy at video rate. *Anal Chem* **2014**, *86* (16), 8448-56.
9. Schmitt, P. D.; DeWalt, E. L.; Dow, X. Y.; Simpson, G. J., Rapid Discrimination of Polymorphic Crystal Forms by Nonlinear Optical Stokes Ellipsometric Microscopy. *Anal Chem* **2016**, *88* (11), 5760-5768.
10. Tiaho, F.; Recher, G.; Rouede, D., Estimation of helical angles of myosin and collagen by second harmonic generation imaging microscopy. *Opt. Express* **2007**.
11. Amat-Roldan, I.; Psilodimitrakopoulos, S.; Loza-Alvarez, P.; Artigas, D., Fast image analysis in polarization SHG microscopy. *Optics Express* **2010**, *18* (16), 17209-17219.
12. Dow, X. Y.; DeWalt, E. L.; Newman, J. A.; Dettmar, C. M.; Simpson, G. J., Unified Theory for Polarization Analysis in Second Harmonic and Sum Frequency Microscopy. *Biophysical Journal* **2016**, *111* (7), 1553-1568.
13. Rodriguez, F. J.; Wang, F. X.; Kauranen, M. J. O. e., Calibration of the second-order nonlinear optical susceptibility of surface and bulk of glass. **2008**, *16* (12), 8704-8710.
14. Boyd, R. J. S. D., Calif, Nonlinear Optics Academic. **2003**, *19922*, 126-143.
15. Simpson, G. J. J. T. J. o. P. C. B., Connection of Jones and Mueller tensors in second harmonic generation and multi-photon fluorescence measurements. **2016**, *120* (13), 3281-3302.
16. Burke, M.; Golaraei, A.; Atkins, A.; Akens, M.; Barzda, V.; Whyne, C., Collagen fibril organization within rat vertebral bone modified with metastatic involvement. *J Struct Biol* **2017**, *199* (2), 153-164.
17. Romijn, E. I.; Finnoy, A.; Lilledahl, M. B., Analyzing the feasibility of discriminating between collagen types I and II using polarization-resolved second harmonic generation. *J Biophotonics* **2019**, *12* (1).
18. Dow, X. Y.; DeWalt, E. L.; Sullivan, S. Z.; Schmitt, P. D.; Ulcickas, J. R. W.; Simpson, G. J., Imaging the Nonlinear Susceptibility Tensor of Collagen by Nonlinear Optical Stokes Ellipsometry. *Biophysical Journal* **2016**, *111* (7), 1361-1374.
19. Avila, F. J.; Bueno, J. M., Analysis and quantification of collagen organization with the structure tensor in second harmonic microscopy images of ocular tissues. *Appl. Opt.* **2015**, *54* (33), 9848-9854.
20. Tuer, A. E.; Akens, M. K.; Krouglov, S.; Sandkuijl, D.; Wilson, B. C.; Whyne, C. M.; Barzda, V., Hierarchical Model of Fibrillar Collagen Organization for Interpreting the Second-Order Susceptibility Tensors in Biological Tissue. *Biophysical Journal* **2012**, *103* (10), 2093-2105.

CHAPTER 4. SPATIAL ENCODED POLARIZATION DEPENDENT NONLINEAR OPTICAL ANALYSIS

A version of this chapter has been published by International Society for Optics and Photonics, 2019. Reprint permission from Changqin Ding, James RW Ulcickas, Fengyuan Deng, and Garth J. Simpson, *Three-Dimensional and Multidimensional Microscopy: Image Acquisition and Processing XXVI*, vol. 10883, p. 108831E. International Society for Optics and Photonics, 2019.

Local hyperpolarizability tensor imaging of collagenous tissue was achieved with spatially encoded polarization dependent nonlinear optical measurements. Spatially encoded polarization dependent second harmonic generation (SHG) was used for local hyperpolarizability tensor imaging of z-cut quartz and collagenous tissue by using a single patterned microretarder array (μ RA). The μ RA was designed with a pattern of half-wave retardance varying spatially in the azimuthal orientation of the fast-axis. When placed in the rear conjugate plane of a beam scanning microscope, the μ RA enabled spatial modulation of incident light with polarization states varied at different positions in the field of view. The ‘snapshot’ approach was available for the polarization dependent measurements of a uniform sample so that one image included a complete set of polarization modulation from different pixels. Combining with sample translation, this method was able to recover local hyperpolarizability tensor of non-uniform samples. This strategy was successfully used to extract local nonlinear optical tensors for z-cut quartz and collagenous tissue with good agreements with traditional polarization dependent measurements, providing an alternate approach for fast polarization analysis of collagen tissue with minimal modifications on current beam scanning nonlinear optical systems.

4.1 Introduction

Polarization-dependent nonlinear optical (NLO) processes, such as second harmonic generation (SHG), enable highly selective imaging contrast for biological and pharmaceutical analysis. Polarization dependent SHG provides rich information on orientation and arrangement of local structures on scales of local molecular assembly, which has been widely used in characterizations of biological tissue¹⁻³, protein crystals and active pharmaceutical ingredients^{4,5}. The higher signal to noise of SHG images comes from its unique symmetry properties and the use of long wavelength with deeper penetration. Polarization-dependent SHG microscopy is

commonly used in the analysis of collagen^{2, 3}, cell membranes⁶, musculoskeletal disorders, corneal disorders⁷⁻⁹, etc. Collagen is a ubiquitous tissue fiber and a commonly cited biomarker for several types of cancers due to associated extracellular fibrosis and reduced metabolism of collagen^{7, 8, 10, 11}. Compared with the majority of pathology diagnostics focused on the microscopic image analysis, polarization-dependent SHG measurements provide complementary information at the molecular level in a length scale smaller than the wavelength of light. The local-frame second-order nonlinear susceptibility tensor, $\chi^{(2)}$, is a $3 \times 3 \times 3$ tensor containing 27 elements, in which up to 18 can be unique to describe the polarization-dependent SHG process. The nonzero elements in the local-frame Jones tensor vary from different local crystal or fiber structure based on the local symmetry. Polarization-dependent SHG imaging can directly measure the local Jones tensor elements, providing a greater amount of local structural information compared to conventional optical imaging methods.

Polarization-dependent SHG microscopy can be achieved with fixed optics such as quarter and half waveplates, rotated between each image acquisition to generate a polarization-dependent image stack¹²⁻¹⁴. Despite their common use and conceptual simplicity, these methods have some significant practical limitations, such as high $1/f$ noise due to the long acquirement time. Recently, fast polarization-dependent SHG microscopy has been reported by using electronic optic modulation or photoelastic modulator. However, these fast polarization modulation requires sophisticated electronic polarization modulator and extreme time control among laser, polarization modulator and data digitizer, complicating the instrumentation built and data acquirement process.

In this chapter, a 25.4 mm diameter microretarder array (μ RA) was placed in the rear-conjugate plane of a beam scanning microscope to spatially modulate the polarization state of light in the image plane during beam-scanning imaging. The μ RA consisted of a designed pattern array for orientation angles of the fast axis of liquid crystal with half-wave retardance. When placing the μ RA in the rear-conjugate plane of a beam scanning system, the polarization rotations introduced by each pixel in the μ RA were projected on the sample plane, achieving a spatial polarization modulation across the whole field of view. For uniform samples, a “snapshot” image was sufficient for the polarization dependent nonlinear optics analysis. For samples with spatially heterogeneous structures, sample translation through one period of the modulation pattern allowed a set of polarization-dependent measurements for each pixel. Subsequent image

analysis was conducted via cross-correlation, such that the same pixels in the resulting image stack were overlaid to compensate the sample translation. The projection of each pixel in the image stack direction was a vector of intensity, with each element of the vector corresponding to a different incident polarization and image frame. Retrieval of tensor elements on a single pixel basis was performed through a nonlinear fitting. This strategy has been validated using z-cut as a model sample with excellent agreement with the theoretical prediction. It has been successfully used in the local Jones tensor analysis of collagen tissue to recover local tensors in pixel level, with agreements with other polarization dependent measurements.

4.2 Experimental Methods

4.2.1 Instrumentation setup

The experiment instrument for spatial encoded polarization dependent nonlinear optical analysis was conducted on a custom-built microscope as shown in *Figure 4.1(A)*. A Spectra-Physics MaiTai Ti:sapphire laser (SpectraPhysics) tuned at 800 nm was used as the light source with horizontally polarized incident light. A resonant scanning mirror at 8.8 kHz (EOPC) and a galvanometer mirror (CambridgeTech) synchronized to the laser were used to scan the beam across the sample. The beam was then expanded through a pair of lenses to fill the back aperture of the objective (10 \times , 0.3 NA, Nikon) with average power around 80 mW on the sample. A 10 \times , 0.3 NA condenser (OPTEM) was used to collect signals from the sample. A wire grid polarizer placed in a rotation stage was used for the polarization selected detector, followed with a dichroic mirror and a bandpass filter (HQ 400/20m-2p; Chroma Technology) to separate the SHG signals from the transmittance. The horizontally and vertically polarized SHG signals were acquired sequentially by rotating the polarizer. Bright field images and SHG images are collected by a photodiode (DET-10A, Thorlabs) and a photomultiplier tubes (PMT, Hamamatsu H12310-40), respectively. Signals are remapped into 512 \times 512 images using MATLAB after digitizing with a PCI-E digitizer oscilloscope cards (AlazarTech ATS-9462).

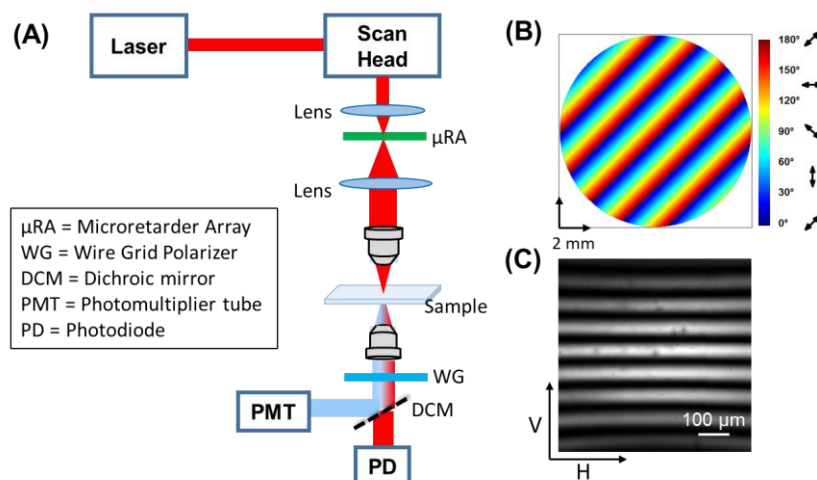


Figure 4.1 Schematic for instrumentation of the spatial encoded polarization dependent nonlinear optical analysis. (A) Placement of the μ RA in the rear-conjugate plane enables polarization encoding across the FoV. (B) The pattern of μ RA with a spatial dependent orientation angle of the retardance, modified according to descriptions from Thorlabs website. (C) Bright field image with the analyzer passing horizontally polarized light in the absence of a sample.

For polarization encoded measurements, a μ RA (DPP-25, Thorlabs) was placed in the rear conjugate plane of the beam scanning microscope to achieve the spatial polarization modulation. The μ RA was designed with an encoded pattern in which the fast axis of retardance for half wave retardance for 800 nm light was rotated linearly across the optics with a 2° increase in the angle of the fast axis across every $25 \mu\text{m}$ strips along a diameter of the array, as shown in *Figure 4.1(B)*. When the μ RA was placed in the rear conjugate plane, a mapped polarization modulation across the field of view (FoV) was achieved with a period of approximately 60 pixels ($\sim 105 \mu\text{m}$ with a 10×0.3 NA objective). *Figure 4.1(C)* shows the acquired image when detecting at horizontally polarized state with the horizontally polarized incident light. The “stripes” in the resulting image contain varying polarization states at different pixels approximately co-parallel with the modulation axis of the μ RA. Translation of the sample through one period of this modulation allows access to SHG detection for the same spot with a whole set of polarization states.

4.2.2 Sample translation

In order to access a whole set of polarization for every single pixel, the samples were translated in the direction roughly parallel with the polarization modulation direction from the μ RA using a sample stage. As shown in *Figure 4.1(C)*, when the polarization modulation is set

approximately along the vertical direction, the sample was translated 18 times along the vertical direction with a step size of 5 μm . The total translation distance was 90 μm , roughly one full period (105 μm) of the modulation period in the μRA in the projection of the sample plane. The translation increment was determined experimentally as around 2 pixels per frame with for the total 19 frames with cross-correlation. It should be noted that due to the uncertainty from the electronic control and motor motion, the translation increment was varied from frame to frame. After overlay all the 512 \times 512 images for 19 frames and removal of edge pixels with incomplete whole polarization modulation, a final data cube was generated with a dimension of 512 \times 476 \times 19. For each pixel, the profile along the third dimension is a vector of SHG intensity from the sample under different incident polarization. The laboratory NLO tensor elements for each specific pixel were then retrieved by fitting the 19-element intensity vector as a function of the polarization modulation. The coordinate transformation from the laboratory to the local frame tensor elements on each pixel was facilitated by the independent determination of the azimuthal angle using *OrientationJ*.

4.2.3 Sample preparation

A piece of z-cut quartz (500 μm thickness) was used to as a proof of concept sample for the spatially encoded polarization-dependent SHG imaging. Collagen tissue used in the polarization-dependent SHG measurements was provided by Prof. Philip Low (Purdue University, West Lafayette, IN). The mouse tails were sectioned longitudinally after decalcification in a solution of 23% formic acid, 4% formalin, and 1% methanol for 2 hours. The mouse tail section was then fixed in 10% formalin and microtomed into 4 μm thick slides before imaging.

4.3 Mathematical Foundation

4.3.1 Polarization modulation in the FoV

As shown in *Figure 4.1(B)*, the polarization modulation generated from the μRA is due to the linearly changing retardance rotation along pixels. When detecting the transmittance signals for horizontally polarized direction in the absence of the sample, the polarization rotation angle γ at each position within the FoV can be determined from a global nonlinear fit from the whole FoV. In the general case, the detected intensity of each pixel in bright field image can be

described as a function of the phase offset δ and the polarization rotation angle γ at each pixel, as shown in Eq. (4.1), in which DC is a constant term so that response from the detector with no signal is zero.

$$I(\gamma, \delta) \propto \cos(\gamma + \delta) + DC \quad (4.1)$$

When the μ RA is not perfectly aligned along either the horizontal (H) or vertical (V) axes, the position-dependent polarization is given by $\gamma(x, y) = ax + by$, in which the peak-to-peak period of modulation c is given by $c = \sqrt{a^2 + b^2}$. In an ideal situation, when the unique axis of the μ RA is placed exactly parallel with the vertical axis, a would equal zero and the modulation would be entirely along the y -coordinate, as shown in *Figure 4.1(C)*.

4.3.2 Jones tensor recovery

Taking z -cut quartz as an example, the laboratory-frame Jones tensor describing the NLO properties of a uniaxial assembly with the unique axis lying in the FoV is given by Eq. (4.2), in which ϕ is the rotation angle of the primary sample axis relative to the laboratory horizontal axis. For the z' -axis oriented coparallel with the laboratory horizontal axis in the laboratory Jones frame, $\chi_{x'x'z'}$, $\chi_{z'x'x'}$, and $\chi_{z'z'z'}$ are nonzero local-frame Jones tensor elements due to the crystal symmetry of z -cut quartz, as detailed in *CHAPTER 1*. For collagen tissue analysis, the nonzero local-frame Jones tensor elements are $\chi_{x'x'z'}$, $\chi_{z'x'x'}$, and $\chi_{z'z'z'}$, with the z' -axis defined as the unique fiber axis..

$$\begin{bmatrix} \chi_{HHH} \\ \chi_{HHV} \\ \chi_{HVV} \\ \chi_{VHH} \\ \chi_{VHV} \\ \chi_{VVH} \\ \chi_{VVV} \end{bmatrix} = \begin{bmatrix} 2g & g & i \\ f-h & -h & h \\ f-h & -h & h \\ -2g & i & g \\ -2h & f & h \\ i-g & -g & g \\ i-g & -g & g \\ 2h & h & f \end{bmatrix} \cdot \begin{bmatrix} \chi_{x'x'z'} \\ \chi_{z'x'x'} \\ \chi_{z'z'z'} \end{bmatrix} ; \begin{cases} f = \sin^3 \phi \\ g = \sin^2 \phi \cos \phi \\ h = \sin \phi \cos^2 \phi \\ i = \cos^3 \phi \end{cases} \quad (4.2)$$

The Jones vector describing the polarization of the second harmonic generation as a function of incident polarization (expressed as rotation angle γ) and the Jones tensor is illustrated in Eq. (4.3).

$$\vec{e}_L^{2\omega} = \begin{bmatrix} e_H^{2\omega} \\ e_V^{2\omega} \end{bmatrix} = \begin{bmatrix} \cos^2 \gamma & \sin \gamma \cos \gamma & \sin \gamma \cos \gamma & \sin^2 \gamma & 0 & 0 & 0 & 0 \\ 0 & 0 & 0 & 0 & \cos^2 \gamma & \sin \gamma \cos \gamma & \sin \gamma \cos \gamma & \sin^2 \gamma \end{bmatrix} \cdot \begin{bmatrix} \chi_{HHH} \\ \chi_{HHV} \\ \chi_{HVV} \\ \chi_{VHH} \\ \chi_{VHV} \\ \chi_{VVH} \\ \chi_{VVV} \end{bmatrix} \quad (4.3)$$

The detected intensity in horizontal polarization ($I_H^{2\omega}$) or vertically polarization ($I_V^{2\omega}$) directions is given by Eq. (4.4).

$$I_H^{2\omega} \propto |e_H^{2\omega}|^2; I_V^{2\omega} \propto |e_V^{2\omega}|^2 \quad (4.4)$$

Combining Eqs. (4.3) and (4.4), five polynomial coefficients of n-polarized SHG from the sample can be recovered from the detected intensity, as given in Eq. (4.5)⁴. The laboratory-frame Jones tensor of the sample can either be recovered directly based on Eqs. (4.2) -(4.4), or expressed by the five polynomial coefficients via Eq. (4.6).

$$I_n = A \cos^4 \gamma + B \cos^3 \gamma \sin \gamma + C \cos^2 \gamma \sin^2 \gamma + D \cos \gamma \sin^3 \gamma + E \sin^4 \gamma \quad (4.5)$$

$$\begin{aligned} A &= |\chi_{nHH}^{(2)}|^2 \\ B &= 4 \cdot \text{Re}(\chi_{nHH}^{(2)*} \cdot \chi_{nHV}^{(2)}) \\ C &= 4 \cdot |\chi_{nHV}^{(2)}|^2 + 2 \cdot \text{Re}(\chi_{nHH}^{(2)*} \cdot \chi_{nVV}^{(2)}) \\ D &= 4 \cdot \text{Re}(\chi_{nVV}^{(2)*} \cdot \chi_{nHV}^{(2)}) \\ E &= |\chi_{nVV}^{(2)}|^2 \end{aligned} \quad (4.6)$$

4.4 Result and discussion

4.4.1 Proof of concept for tensor recovery using z-cut quartz

The z-cut quartz was used as a model nonlinear optical source for spatially encoded polarization dependent nonlinear optical analysis due to its well-established nonlinear optical properties and no linear birefringence for light propagating parallel with the z-axis. The uniform structure of z-cut quartz simplified the data analysis since no sample translation was required. The z-cut quartz was inserted in an automated rotation stage and rotated from 0 to 60 degree with 3-degree increments. The resulting set of 21 images was acquired as shown in *Figure 4.2*. For

each image, intensities were averaged along the horizontal axis to form one vector due to the spatially uniform SHG response from quartz. This set of vectors was reshaped as a 512×21 image with axes corresponding to varied polarization angle (γ) and z-cut quartz rotation angle (ϕ), respectively. It is noted that there was no variation in bright field intensity as a function of quartz rotation angle. However, a shifted modulation pattern was observable for the polarized SHG intensity within the period of 60 degrees of the rotation angle, as predicted by the 3-fold symmetry of the quartz. This polarization rotation angle γ at each pixel was determined from a global fit of the bright field as described in *Section 4.3.1*.

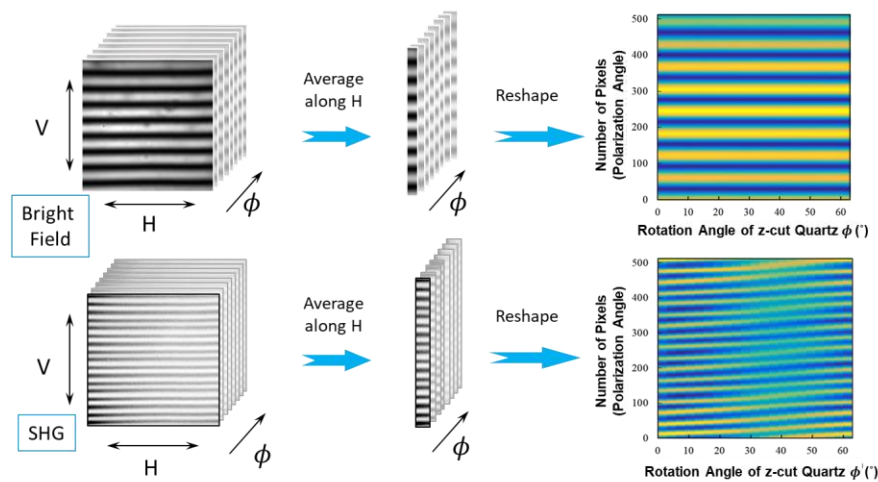


Figure 4.2 Illustration of the data acquisition and analysis process of the bright-field and SHG images of z-cut quartz.

The set of corresponding polynomial coefficients in the laboratory frame for z-cut quartz at different angles were determined from the recovered γ in each pixel using Eq. (4.5). A result of the direct linear fitting was shown in *Figure 4.3*. Great similarity can be seen between the experiment measurement [*Figure 4.3(A)*] and fitted intensity map [*Figure 4.3(B)*]. It was clear that there is a period of 60 degrees of z-cut quartz rotation, which agreed with the prediction from the 3-fold symmetry of z-cut quartz.

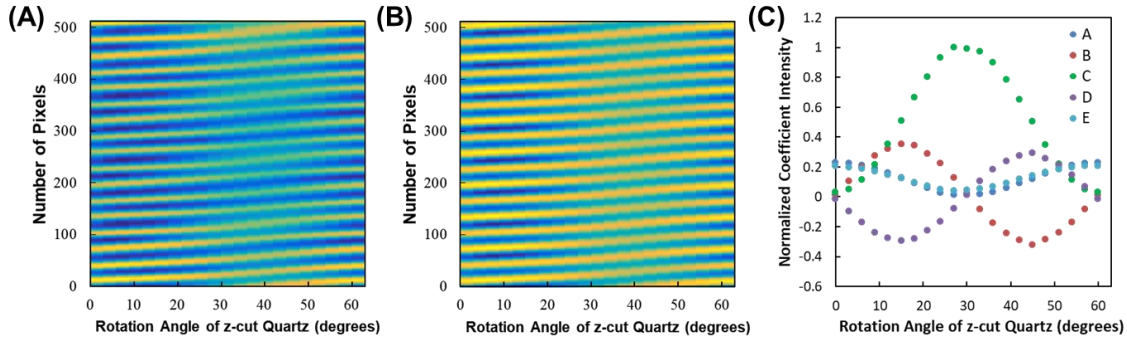


Figure 4.3 Direct linear fit for polynomial coefficients recovery from SHG measurements of z-cut quartz on the reshaped data set. (A) is the experiment measurement data set; (B) is the fitted intensity image, and (C) is the plot for polynomial coefficients recovered from the fitting.

With the prior knowledge of tensor relationship of z-cut quartz that $\chi_{z'z'z} = -\chi_{z'x'x'} = -\chi_{x'x'z'}$, an iteration fit method was applied on the same data set with an initial guess of $[\chi_{x'x'z'}, \chi_{z'z'z}, \chi_{z'x'x'}]$ as $[1, 1, -1]$. After the initial azimuthal angle of quartz was determined from a nonlinear fit based on the initial guess, the fitted intensity map was generated and followed with an iterated linear fit to retrieve the polynomial coefficients. The recovery intensity map is shown in *Figure 4.4(B)* with the retrieved polynomial coefficients plotted as dots in and *Figure 4.4(C)*, with a measured local tensor elements ratio as $\chi_{zzz}/\chi_{zxx} = -1.0 \pm 0.1$. With the same prior knowledge of tensor relationship, a simplified expression of Eq. (4.6) can be used to predict the polynomial coefficients as a function of z-cut quartz rotation angle ϕ as shown in Eq. (4.7).

$$\begin{aligned}
 A &= E = \cos^2(3\phi) \\
 B &= -D = 2 \sin(6\phi) \\
 C &= 6 \sin^2(3\phi) - 2
 \end{aligned} \tag{4.7}$$

The predictions from Eq. (4.7) were plotted as solid lines in *Figure 4.4(C)*, with great agreements with the measurements. The results supported the validity of the mathematical framework of spatially encoded polarization dependent nonlinear optical analysis. The differences between *Figure 4.3(C)* and *Figure 4.4(C)* were probably because of the polarization purity lost due to the unexpected polarization dependent optics in the beam path.

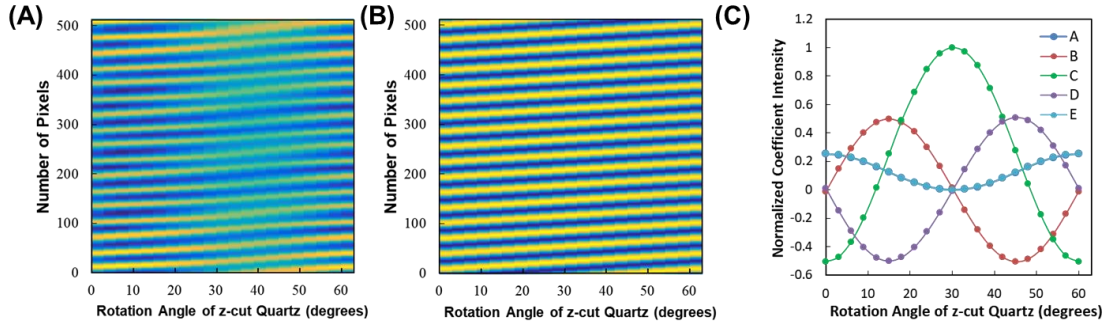


Figure 4.4 Iteration fit for polynomial coefficients recovery from SHG measurements of z-cut quartz on the reshaped data set. (A) is the experiment measurement data set; (B) is the fitted intensity image, and (C) is the plot for polynomial coefficients recovered from the fitting.

4.4.2 Tensor recovery of collagen tissue with sample translation

The use of spatially encoded polarization dependent nonlinear optical analysis for recovery of local tensors in collagenous tissue was achieved using sample translation as detailed in *Section 4.3.2*. The polarization pattern in the FoV was fixed by the μ RA in the rear conjugate plane while the sample was translated within the image plane. For each location in the sample, different polarizations were introduced for different frames. As shown in *Figure 4.5(A)*, polarization modulation generated from the μ RA was set along the y -direction, while the sample was translated in the x -direction with a step size of $5 \mu\text{m}$ from frame to frame. After stacking the images using cross-correlation, a data cube in a dimension of $512 \times 476 \times 19$ was generated. For each pixel, the profile in the third dimension was a function of the frame number/polarization state, same as shown in Eq. (4.5). Tensor elements for collagen tissue at each pixel were recovered directly with a nonlinear fit based on Eqs. (4.2) - (4.4). *Figure 4.5(B)* presents the measured SHG intensity of a representative pixel (dots) detecting in horizontal (green) or horizontal (yellow) polarization states with the nonlinear fit result (lines) with the definition that $\rho \equiv \chi_{z'z'z'}/\chi_{z'x'x'}$. The incomplete modulation period was due to the finite translation of the sample since the total translation distance in the experiment was $90 \mu\text{m}$ compared to $105 \mu\text{m}$ for one polarization modulation period.

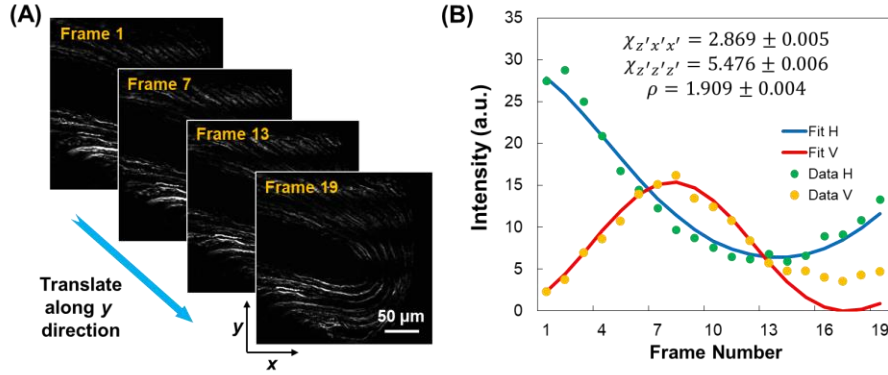


Figure 4.5 Translation-based spatially encoded polarization dependent NLO imaging for collagen tissue. (A) SHG images detected in the horizontally polarized direction of collagenous tissue translating along y-direction with a translate step size of $5\mu\text{m}$ between frames. For each pixel, different polarization incidence was achieved due to the sample translation. (B) Overlay of the measured intensity of a random pixel (dots) detecting in horizontal (green) or horizontal (yellow) polarization states with the linear fit result (lines). Scale bar: $50\mu\text{m}$. Dwell time for each pixel was $1.8\mu\text{s}$.

Unlike z-cut quartz, the nonzero independent local frame tensor elements for collagen are $\chi_{z'z'z'}$, $\chi_{z'x'x'}$, $\chi_{x'x'z'}$, and a chiral element $\chi_{y'z'x'}$. However, the chiral element is relatively smaller in magnitude than the other elements and is completely negligible for collagen fibers orientated with the unique axis flat within the image plane (tilt angle of 90°)¹⁵⁻¹⁷. In this experiment, an estimation of $\chi_{z'x'x'} \cong \chi_{x'x'z'}$ was applied^{4, 18-20} to simplify the calculation. In contrast with the data analysis of z-cut quartz, the orientation of collagen fiber (ϕ) at each pixel was recovered using *OrientationJ*, a plugin in *ImageJ*, as shown in *Figure 4.6(A)*. Then, the local-frame Jones tensor elements were calculated from a direct nonlinear fit based on Eqs. (4.2) - (4.4). *Figure 4.6(B)* presents the measured ρ value for each pixel in the field of view. The histogram of measured ρ is plotted in *Figure 4.6(C)*, with a modal value of 1.2 and the mean value of 1.46 in agreement with previous reports²¹. The broad distribution of the measured ρ value is tentatively attributed primarily to the intrinsic variability in collagen orientation. Although addition variance in ρ may also arise from the distribution in the ratio of two randomly distributed numbers²².

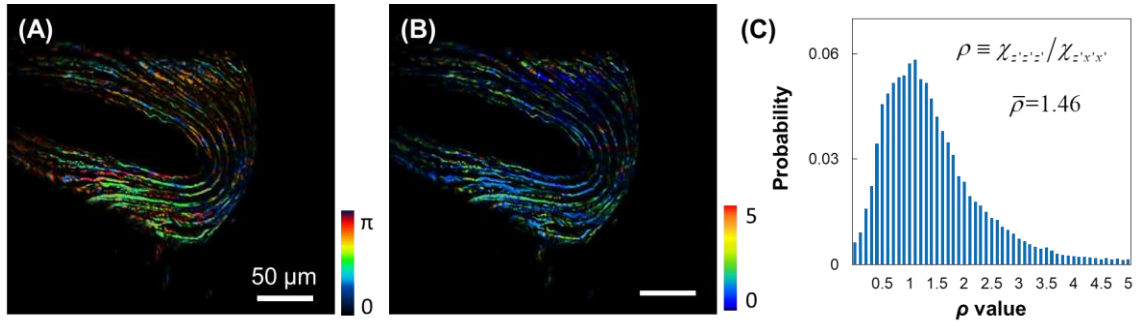


Figure 4.6 The orientation angle and tensor ratio recovered from collagen tissue on the base of each pixel. (A) The orientation angle of collagen fibers for each pixel within the FoV retrieved from *OrientationJ*. (B) Image for the ratio ρ of local Jones tensor elements, with a mean value of 1.46 and modal value of 1.2. (C) Histogram of ρ for the whole field of view.

4.5 Conclusion

Local tensor imaging was achieved with spatially encoded polarization dependent nonlinear optical analysis compatible with commercial multiphoton/nonlinear optical microscopes. The placement of a μ RA in the rear conjugate plane of a beam scanning microscope enabled spatial modulation of incident light with polarization states varied at different positions in the field of view. The ‘snapshot’ approach was successfully used to extract local nonlinear optical tensors for z-cut quartz consistent with the theoretical predictions. The sample translation strategy was used to achieve pixel-level tensor information retrieval for collagenous tissue with a great agreement with traditional polarization dependent measurements, enabling tissue analysis for disease diagnostics with submicron-scale resolution. This work provides an alternate approach for polarization analysis with minimal modifications on existing beam scanning systems. While the imaging speed is limited in this strategy due to the use of sample translation, this spatially encoded approach has the ability to leverage spatial correlations within images for pooling of polarization analysis. In the future work, advanced image segmentation methods coupled with single snapshot measurement is expected to reduce image acquiring time and 1/f noise in the measurements.

4.6 References

1. Campagnola, P. J.; Loew, L. M., Second-harmonic imaging microscopy for visualizing biomolecular arrays in cells, tissues and organisms. *Nat Biotechnol* **2003**, *21* (11), 1356-1360.
2. Stoller, P.; Reiser, K. M.; Celliers, P. M.; Rubenchik, A. M., Polarization-modulated second harmonic generation in collagen. *Biophysical Journal* **2002**, *82* (6), 3330-3342.
3. Gusachenko, I.; Tran, V.; Houssen, Y. G.; Allain, J. M.; Schanne-Klein, M. C., Polarization-Resolved Second-Harmonic Generation in Tendon upon Mechanical Stretching. *Biophysical Journal* **2012**, *102* (9), 2220-2229.
4. DeWalt, E. L.; Sullivan, S. Z.; Schmitt, P. D.; Muir, R. D.; Simpson, G. J., Polarization-Modulated Second Harmonic Generation Ellipsometric Microscopy at Video Rate. *Anal Chem* **2014**, *86* (16), 8448-8456.
5. Schmitt, P. D.; DeWalt, E. L.; Dow, X. Y.; Simpson, G. J., Rapid Discrimination of Polymorphic Crystal Forms by Nonlinear Optical Stokes Ellipsometric Microscopy. *Anal Chem* **2016**, *88* (11), 5760-5768.
6. Moreaux, L.; Sandre, O.; Mertz, J., Membrane imaging by second-harmonic generation microscopy. *J Opt Soc Am B* **2000**, *17* (10), 1685-1694.
7. Plotnikov, S.; Juneja, V.; Isaacson, A. B.; Mohler, W. A.; Campagnola, P. J., Optical clearing for improved contrast in second harmonic generation Imaging of skeletal muscle. *Biophysical Journal* **2006**, *90* (1), 328-339.
8. Plotnikov, S. V.; Millard, A. C.; Campagnola, P. J.; Mohler, W. A., Characterization of the myosin-based source for second-harmonic generation from muscle sarcomeres. *Biophysical Journal* **2006**, *90* (2), 693-703.
9. Latour, G.; Echard, J. P.; Didier, M.; Schanne-Klein, M. C., In situ 3D characterization of historical coatings and wood using multimodal nonlinear optical microscopy. *Opt. Express* **2012**, *20* (22), 24623-24635.
10. Brasselet, S., Polarization-resolved nonlinear microscopy: application to structural molecular and biological imaging. *Adv. Opt. Photon.* **2011**, *3* (3), 205-271.
11. Lin, S. J.; Jee, S. H.; Kuo, C. J.; Wu, R. J.; Lin, W. C.; Chen, J. S.; Liao, Y. H.; Hsu, C. J.; Tsai, T. F.; Chen, Y. F.; Dong, C. Y., Discrimination of basal cell carcinoma from normal dermal stroma by quantitative multiphoton imaging. *Opt. Lett.* **2006**, *31* (18), 2756-2758.
12. Nadiarnykh, O.; Plotnikov, S.; Mohler, W. A.; Kalajzic, I.; Redford-Badwal, D.; Campagnola, P. J., Second harmonic generation imaging microscopy studies of osteogenesis imperfecta. *J Biomed Opt* **2007**, *12* (5), 051805.
13. Psilodimitrakopoulos, S.; Santos, S. I. C. O.; Amat-Roldan, I.; Thayil, A. K. N.; Artigas, D.; Loza-Alvarez, P., In vivo, pixel-resolution mapping of thick filaments' orientation in nonfibrillar muscle using polarization-sensitive second harmonic generation microscopy. *J Biomed Opt* **2009**, *14* (1), 014001.

14. Hu, P. S.; Ghazaryan, A.; Hovhannisyan, V.; Chen, S. J.; Chen, Y. F.; Kim, C. S.; Tsai, T. H.; Dong, C. Y., Imaging of biological tissues with pixel-level analysis of second-order susceptibility. *J Biomed Opt* **2013**, *18* (3), 031102.
15. Rodriguez, F. J.; Wang, F. X.; Kauranen, M. J. O. e., Calibration of the second-order nonlinear optical susceptibility of surface and bulk of glass. **2008**, *16* (12), 8704-8710.
16. Boyd, R. J. S. D., Calif, Nonlinear Optics Academic. **2003**, 19922, 126-143.
17. Dow, X. Y.; DeWalt, E. L.; Newman, J. A.; Dettmar, C. M.; Simpson, G. J., Unified Theory for Polarization Analysis in Second Harmonic and Sum Frequency Microscopy. *Biophysical Journal* **2016**, *111* (7), 1553-1568.
18. Burke, M.; Golaraei, A.; Atkins, A.; Akens, M.; Barzda, V.; Whyne, C., Collagen fibril organization within rat vertebral bone modified with metastatic involvement. *J Struct Biol* **2017**, *199* (2), 153-164.
19. Ding, C. Q.; Ulcickas, J. R. W.; Deng, F. Y.; Simpson, G. J., Second Harmonic Generation of Unpolarized Light. *Phys Rev Lett* **2017**, *119* (19), 193901.
20. Tokarz, D.; Cisek, R.; Golaraei, A.; Krouglov, S.; Navab, R.; Niu, C.; Sakashita, S.; Yasufuku, K.; Tsao, M. S.; Asa, S. L.; Barzda, V.; Wilson, B. C., Tumor tissue characterization using polarization-sensitive second harmonic generation microscopy. *Biophotonics South America* **2015**, *9531*, 95310C.
21. Dow, X. Y.; DeWalt, E. L.; Sullivan, S. Z.; Schmitt, P. D.; Ulcickas, J. R. W.; Simpson, G. J., Imaging the Nonlinear Susceptibility Tensor of Collagen by Nonlinear Optical Stokes Ellipsometry. *Biophysical Journal* **2016**, *111* (7), 1361-1374.
22. Ulcickas, J. R. W.; Ding, C. Q.; Deng, F. Y.; Simpson, G. J., Spatially encoded polarization-dependent nonlinear optics. *Opt. Lett.* **2018**, *43* (24), 5973-5976.

CHAPTER 5. AXIALLY-OFFSET DIFFERENTIAL INTERFERENCE CONTRAST MICROSCOPY VIA POLARIZATION WAVEFRONT SHAPING

A version of this chapter has been published by *Optics Express*. Reprint permission from Changqin Ding, Chen Li, Fengyuan Deng, Garth J. Simpson, Axially-Offset differential interference contrast microscopy via polarization wavefront shaping. *Optics Express*. 2019, 27(4), 3837-3850, copyright © 2019 Optical Society of America under the terms of the OSA Open Access Publishing Agreement.

Sample-scan phase contrast imaging was demonstrated by producing and coherently recombining light from a pair of axially offset focal planes. Placing a homogeneous medium in one of the two focal planes enables quantitative phase imaging using only common-path optics, recovering absolute phase without halo or oblique-illumination artifacts. Axially offset foci separated by 70 μm with a 10 \times objective were produced through polarization wavefront shaping using a matched pair of custom-designed microretarder arrays, compatible with retrofitting into conventional commercial microscopes. Quantitative phase imaging was achieved by two complementary approaches: i) rotation of a half wave plate, and ii) 50 kHz polarization modulation with lock-in amplification for detection.

5.1 Introduction

Phase-sensitive microscopy, including Zernike phase contrast and Nomarski differential interference contrast (DIC), allows visualization of weakly scattered samples with low contrast in conventional bright field microscopy¹⁻³. Zernike phase contrast produces intensity contrast dependent on spatial interference between light patterned with annular rings, effectively highlighting phase differences between relatively tightly focused and relatively gently focused beams. Nomarski DIC instead produces contrast from interference between laterally offset locations within the field of view. In DIC, a Nomarski prism splits linearly polarized incident light to two orthogonally polarized components with a slight angle offset. By recombining the two components using a matched Nomarski prism, the resulting interferogram at a particular position within the field of view scales with the phase difference between that location and an adjacent spatially offset position. DIC microscopy has been actively used in biological research

since the 1970s, including observing neurons in unstained tissue slices⁴, studying kinesin-driven movement⁵, visualizing microtubule-related motility in cells⁶, etc. In both Nomarski and Zernike phase contrast imaging, artifacts related to the interference between locations within the field of view complicate image interpretation. Specifically, Zernike images generally produce orientation-independent “halo” artifacts and Nomarski orientation-dependent “side lighting” artifacts. Furthermore, both phase contrast microscopy and DIC microscopy lack the capability to quantitatively retrieve the absolute phase information from the recorded images without careful calibration⁷.

To achieve artifact-free quantitative phase imaging (QPI), Gabor suggested the use of interferometry to quantitatively recover the complex optical field⁸, in which a beam is split and recombined at an angle such that the focal plane array records an interferogram⁹⁻¹². Based on the same physical principles, many other interferometric QPI approaches were developed recently^{7, 13, 14}. Although the abovementioned QPI methods can provide quantitative phase information with high precision, these dual-path interferometric approaches face the common problem of being vulnerable to environmental perturbations such as mechanical vibrations and temperature changes since the reference beam does not pass through the same optical path as the light coming from the object. In addition, the requirement of a long coherence-length reference beam increases the complexity of these QPI systems making them incompatible with retrofitting into existing microscopy systems. Finally, phase retrieval in dual-path QPI is performed by image analysis relative to a background, which can be challenging in complex samples for which a background reference is not trivially available.

Recent developments have helped address the limitations of dual-path interferometry for QPI. In work by Popescu and coworkers, a diffraction grating and spatial filter were used to produce interference from the 0th and 1st order of diffraction from the same microscope output, suppressing the phase instability in dual-path QPI microscopy¹⁵⁻¹⁷. However, these interference approaches are still inherently underdetermined; both phase and intensity must be inferred by image reconstruction rather than directly and independently measured at each pixel. As an alternative, Fourier ptychography¹⁸, phase retrieval with designed periphery¹⁹, using patterned illumination²⁰ or spatial light modulation for image shifting²¹, and coherent diffraction imaging²² recover the absolute relative phase information from adjacent objects without a reference beam. However, these methods are based on assumptions on the beam passing through the object and

mathematically inferred a reference wavefront, complicating both the image acquisition and the post-processing. Therefore, an approach capable of independently recovering absolute phase at every pixel using common path optics may have distinct advantages in phase recovery for complex objects with low spatial correlation. Additionally, architectures that are compatible with retrofitting into existing microscopes rather than requiring custom designs have the potential to greatly expand the broader use and access to artifact-free QPI.

In the present work, axially-offset differential interference contrast (ADIC) microscopy for QPI was developed via polarization wavefront shaping using a matched pair of micro-retarder arrays (μ RAs). The μ RA is a custom optic enabling patterning of the retardance and fast axis orientation of a liquid crystal on a per-pixel basis. Polarization wavefront shaping using the μ RA to produce a polarization-dependent pattern expected from the combination of orthogonally polarized divergent and convergent beams. For linearly polarized incident light and half-wave retardance in every pixel in the μ RA, the polarization wavefront is identical to that produced by the interference between a slightly diverging right circularly polarized (RCP) plane wave and a slightly converging left circularly polarized (LCP) plane wave. After passing through a 10x objective, each of the orthogonal polarization components focus to separate focal planes separated by 70 μm (~ 5.6 times the depth of field), serving as sample and reference planes. Two strategies, including half wave plate (HWP) rotation and lock-in amplified (LIA) detection, were adopted in ADIC microscopy for simultaneous retrieval of transmittance (real component of the image) and quantitative phase (imaginary component) images. The recovered quantitative phase (QP) images agreed well between the two strategies with a phase range from $-\pi$ to π and a detection limit of 0.033 radians. Silica microbeads were used to investigate the refractive index with an agreement between the measurement and the refractive index of amorphous bulk silica. QP images in tissue section samples were measured by using ADIC microscopy.

5.2 Methods

5.2.1 Principles of polarization wavefront shaping by μ RA

A linearly polarized incident beam can be viewed as a coherent combination of two orthogonally polarized components. In standard DIC, linearly polarized incident light is split into horizontally polarized and vertically polarized light using Nomarski prism²³, In the more general

case, the polarization state of light at any position on the Poincaré sphere can also be defined by a coherent combination of two orthogonally polarized components, such as RCP and LCP light.

While most conventional optics affect the polarization state of the entire beam identically, waveplate arrays, such as liquid crystal polymer waveplates, allow the tailoring of the polarization state of light on a per pixel basis. The geometrical phase modulation can be achieved by orientation modulation of liquid crystal polymers on thin polymer substrates. Waveplate arrays have been developed for adaptable lenses^{24,25}, grating prisms^{26,27}, spiral phase retarders²⁸⁻³⁰, etc. Wavefront shaping has been used to split beam into beamlets of orthogonally polarized light focused or defocused depending on the handedness of polarization of the beam³¹. In the present work, a retardance pattern of concentric rings with a quadratic spacing was designed to produce an orthogonally polarized pair of converging and diverging beams.

The pattern necessary to produce this beam pair is most intuitively understood by first considering the anticipated polarization-dependent pattern produced by the interference of orthogonally polarized converging and diverging plane waves. The overlay of converging right circular and diverging left circularly polarized beams produces linearly polarized light with the axis of polarization rotated in a radial pattern as shown in *Figure 5.1(A)*, which has similarities to a Fresnel zone plate. Designing a μ RA to produce this pattern for a linearly polarized incident beam therefore generates diverging and converging components, which can be recombined using a paired μ RA in transmission. For linearly polarized incident light with the plane of polarization given by the angle γ , decomposition into the RCP and LCP contributions yields the expression shown in Eq. (5.1).

$$\begin{pmatrix} \cos(\gamma) \\ \sin(\gamma) \end{pmatrix} = \frac{1}{2} \cdot e^{-i\gamma} \cdot \begin{pmatrix} 1 \\ i \end{pmatrix} + \frac{1}{2} \cdot e^{i\gamma} \cdot \begin{pmatrix} 1 \\ -i \end{pmatrix} \quad (5.1)$$

In this work, μ RAs were designed with the pattern of half-wave retardance of 532 nm light at every position varying spatially in the azimuthal orientation of the fast-axis with a $60 \mu\text{m} \times 60 \mu\text{m}$ pixel size per entry and an active radius of 12 mm. The azimuthal orientation θ as a function of x, y position agrees to the relationship: $\theta(x, y) = 2\pi[(x-r)^2 + (y-r)^2]/4f\lambda$, in which r is the active radius, f is focal length designed as 6.28 m and λ is the targeting wavelength as 532 nm. The azimuthal orientation was then wrapped in the range of $[0, \pi]$. The designed μ RA was then custom produced by Thorlabs. No artifacts from the periodicity inherent in the μ RA design were detectable in either the measured intensity patterns shown in *Figure 5.1(A)* or in the resulting QP

images. Unlike Nomarski DIC, in which the split beams are offset laterally within the sample plane [Figure 5.1(B)], the decomposed converging LCP and diverging RCP light after the μ RA were offset axially after the same objective, such that the reference beam was defocused within the sample plane [Figure 5.1(C)]. Axially offsetting the two focal planes allowed the use of a homogeneous medium (e.g, glass, solvent, air) as a reference. In the absence of a sample, a paired identical μ RA in transmittance coherently recombined the two orthogonal components to recover a plane wave with the original polarization state of the incident light. Phase contrast imaging can be performed by placing a polarizer in the quadrature position, with shifts in phase between the sample and reference planes resulting in changes in polarization states, and correspondingly, changes in detected intensity. Modulating the polarization states of the incident light allows for signal to noise enhancement through LIA detection.

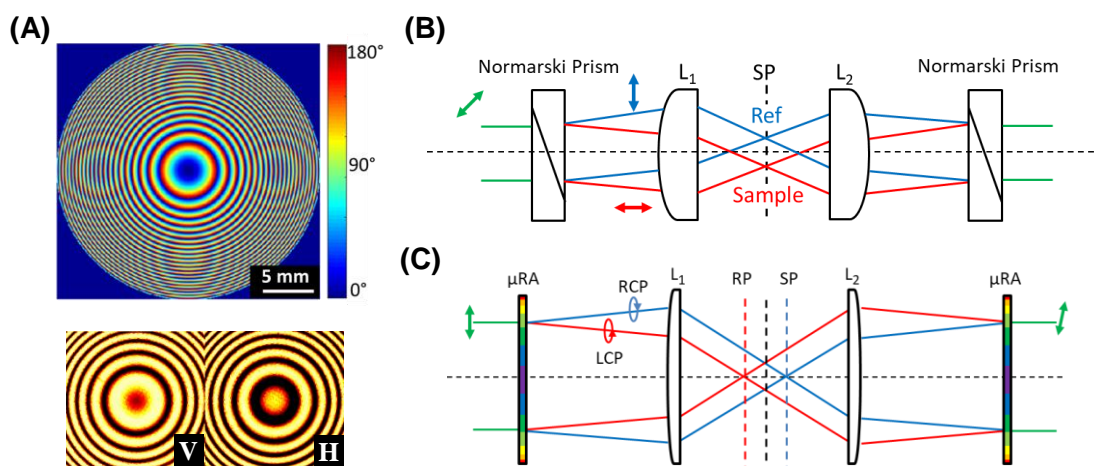


Figure 5.1 The principles of axial-offset foci generation and design of μ RA. (A) The design of μ RA as half-wave retardance with spatially varied azimuthal orientation of the fast-axis targeted for 532 nm light. Scale bar: 500 μ m. Bottom: part of the measured different intensity distribution with horizontal (H) and vertical (V) polarization detection when horizontally polarized light passing through the μ RA. (B) The working principle of traditional Nomarski phase contrast microscope. (C) The working principle of ADIC microscope. L1 and L2: lens; RP: reference plane; SP: sample plane.

5.2.2 Instrumentation for ADIC microscopy

The ADIC microscope was constructed based on a bright field microscope frame with the addition of several polarizing optics (Figure 5.2). In brief, a 532 nm continuous laser (Millenia Vs J) was used for illumination with initial horizontal polarization, followed with a half wave

plate (HWP) inserted in a rotation stage for linearly polarization modulation of the incident light. The beam was expanded to 15 mm in diameter to fill approximately half the area of the μ RA and the full aperture of a 10x objective (0.3 NA, Nikon). The average laser power on the sample was around 5 mW. An identical 10x 0.3 NA objective was used as a condenser in transmittance, followed by passage through a paired μ RA, positioned and oriented to recover an identically polarized plane wave in the absence of a sample. A sample scanning stage (Mad city labs Nano-Bio300) was driven by two phase-locked function generators (Tektronix AFG2021 and Agilent 33220A) for image acquisition with a frame rate of 20 s with a field of view (FoV) of $250 \mu\text{m} \times 250 \mu\text{m}$. Horizontally polarized transmittance was detected by passing the beam through a polarizer (LPNIRE100-B, Thorlabs) and a photodiode (DET-10A, Thorlabs). Signals were digitized at 20 kHz using a PCI-E digitizer oscilloscope cards (AlazarTech ATS-9462) and remapped into 200×200 pixel images via custom software (MATLAB), giving a pixel size of $1.25 \mu\text{m}/\text{pixel}$. Polarization modulation measurements were conducted via mechanical rotation of the HWP from 0 to 90 degrees with 3-degree intervals. For the fast polarization modulation coupled with LIA (Stanford Research Systems SR810) detection, a photoelastic modulator (PEM, Hinds instrument PEM-90M) was inserted between HWP and a quarter waveplate (QWP). PEM is made of isotropic optical materials and introduce retardance $[\Delta(\tau)]$ to the incident light as a function of time when driven at a resonant frequency. It has two electric TTL outputs with one has the modulation frequency ($1f$) and the other has the doubled frequency ($2f$) of the sinusoidal driven electric field. The fast axis of the HWP, PEM and QWP were rotated to 22.5° , 0° and 45° , respectively, for modulation of the linearly polarized light before entering the μ RA, as detailed in Eqs. (7) and (8) (*Section 2.4*). The PEM was operating at its resonance frequency of 50 kHz, with both $1f$ (50 kHz) and $2f$ (100 kHz) outputs delivered as the reference signals to the LIA. Both the quadrature and in-phase components of the LIA output were acquired simultaneously. The per-pixel integration time of the LIA was 30 μs . The same setup was used for both the investigation experiment of the dual-foci and the later QPI experiments.

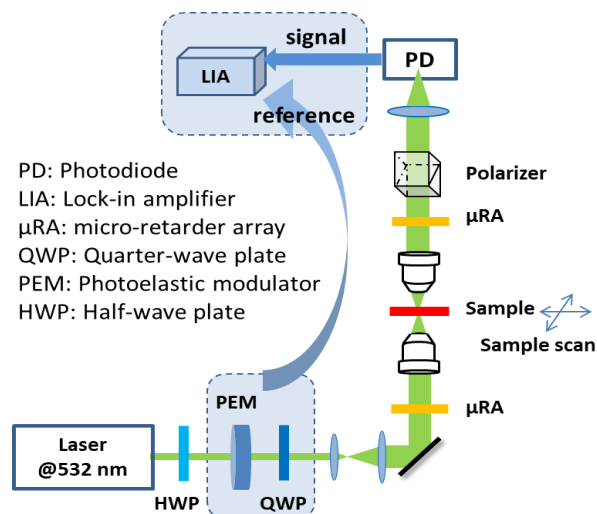


Figure 5.2. Experiment set-up for QPI with a 10x objective to recover both bright field images and QP images. Blue circled optics: add-in parts for LIA detection.

5.2.3 Sample preparation

Two separate samples were prepared for analysis by ADIC: silica beads and mouse tail sections. Silica beads sized in diameter of 8 μm were donated by Prof. Mary Wirth (Purdue University, West Lafayette, IN). For quantitative phase imaging, the silica beads were dispersed by ultrasonication in a commercially available nitrocellulose matrix with a high vapor pressure solvent plasticizer (Sally Hanson nail polish, Hardener) before sealing between a cover slip and a glass slide, followed by solvent evaporation. Mouse tail sections were provided by Prof. Philip Low (Purdue University, West Lafayette, IN). Mouse tails were first decalcified in the solution of 23% formic acid, 4% formalin, and 1% methanol for 2 hours, followed by sectioning longitudinally to ensure that sections were retrieved from the central region of the tail. The mouse tail section was then fixed in 10% formalin and embedded in paraffin prior to microtoming into 4 μm thick slides. After sectioning, the mouse tail was stained by hematoxylin and eosin.

5.2.4 QP image recovery

In the absence of a sample, the identity matrix produced by the sequential combination of the matched ADIC optics can be decomposed as a linear combination of Hermitian Pauli

matrices as shown in Eq. (5.2). The decomposed matrices can describe the Jones matrices corresponding to the two foci with orthogonally polarized components.

$$\overline{e^0} = \begin{pmatrix} 1 & 0 \\ 0 & 1 \end{pmatrix} \cdot \overline{e^0} = \frac{1}{2} \left\{ \left[\begin{pmatrix} 1 & 0 \\ 0 & 1 \end{pmatrix} + \begin{pmatrix} 0 & i \\ -i & 0 \end{pmatrix} \right] + \left[\begin{pmatrix} 1 & 0 \\ 0 & 1 \end{pmatrix} + \begin{pmatrix} 0 & -i \\ i & 0 \end{pmatrix} \right] \right\} \cdot \overline{e^0} \quad (5.2)$$

When a sample-induced phase shift is introduced in either focal plane, the Jones vector describing the signal electric field ($\overline{e^{det}}$) after the sample can be expressed by Eq. (5.3). The complex-valued amplitude transmittances t^+ and t^- describe the field detected following interaction in the two foci separately. The phase change δ induced by the sample at a given location is defined to be the phase shift between the two orthogonally polarized focal planes (sample and reference planes). In the absence of a sample, $|t^+| = |t^-| = 1$ and $\delta = 0$, resulting in $\overline{e^{tot}} = \overline{e^0}$, such that the detecting signals are identical to the incident light.

$$\overline{e^{tot}} = \frac{1}{2} \left(|t^+| \cdot \begin{bmatrix} 1 & i \\ -i & 1 \end{bmatrix} \cdot e^{i\frac{\delta}{2}} + |t^-| \cdot \begin{bmatrix} 1 & -i \\ i & 1 \end{bmatrix} \cdot e^{-i\frac{\delta}{2}} \right) \cdot \overline{e^0} \quad (5.3)$$

The (+) and (-) focal planes produced by the μ RA are orthogonally polarized relative to each other and 90 degrees phase-shifted relative to the incident polarization state [e.g., for linearly polarized light, the polarization states of the (+) and (-) focal planes are RCP and LCP, respectively]. In the case of half wave plate rotation strategy describing horizontally polarized light passing through a half wave plate with fast axis rotated to angle γ , the Jones vector describing the incident light is given by the following expression:

$$\overline{e^0(\gamma)} = \begin{bmatrix} \cos 2\gamma & \sin 2\gamma \\ \sin 2\gamma & -\cos 2\gamma \end{bmatrix} \cdot \begin{bmatrix} 1 \\ 0 \end{bmatrix} \quad (5.4)$$

The detected intensity through a polarizer rotated to angle ϕ_{pol} is given by Eq. (5.5).

$$\overline{e^{det}(\gamma)} = \begin{bmatrix} \cos \phi_{pol} & -\sin \phi_{pol} \\ \sin \phi_{pol} & \cos \phi_{pol} \end{bmatrix} \begin{bmatrix} 1 & 0 \\ 0 & 0 \end{bmatrix} \begin{bmatrix} \cos \phi_{pol} & \sin \phi_{pol} \\ -\sin \phi_{pol} & \cos \phi_{pol} \end{bmatrix} \cdot \overline{e^{tot}(\gamma)} \quad (5.5)$$

$$I(\phi_{pol}, \gamma) \propto \left| \overline{e^{det}(\gamma)} \right|^2 \quad (5.6)$$

When detecting the horizontally polarized component ($\phi_{pol} = 0$), combining the expressions in Eqs. (5.3) - (5.6) followed by simplification yields Eq. (5.7), in which γ is the rotated angle of the incident HWP.

$$I(\gamma) \propto |t^+|^2 + |t^-|^2 + 2|t^+||t^-| \cdot \cos(\delta + 4\gamma) \quad (5.7)$$

For the LIA detection, the PEM and the QWP were placed between the HWP and pair of lenses for beam expansion, and the fast axis of HWP and QWP were rotated to 22.5° and 45° , respectively, as shown in *Figure 5.2*. The Jones vector describing the incident light is given by the following Eq. (5.8), in which $\Delta(\tau)$ is the retardance modulation introduced by the PEM as a function of time (τ) with a modulation amplitude of $2A$, as defined in Eq. (5.9). It can be seen that with a horizontally polarized incident light, linearly polarized light was generated after the HWP, PEM and QWP to pass through the μ RA. The retardance modulation frequency for the PEM was $f = 50$ kHz.

$$\overline{e^0(\tau)} \propto \begin{bmatrix} 1 & -i \\ -i & 1 \end{bmatrix} \cdot \begin{bmatrix} e^{-i\Delta(\tau)/2} & 0 \\ 0 & e^{i\Delta(\tau)/2} \end{bmatrix} \cdot \begin{bmatrix} 1 & 1 \\ 1 & -1 \end{bmatrix} \cdot \begin{bmatrix} 1 \\ 0 \end{bmatrix} = \sqrt{2}(1-i) \begin{bmatrix} \sin\left(\frac{\Delta(\tau)}{2} + \frac{\pi}{4}\right) \\ \cos\left(\frac{\Delta(\tau)}{2} + \frac{\pi}{4}\right) \end{bmatrix} \quad (5.8)$$

$$\Delta(\tau) = 2A \cdot \sin(2\pi f \tau) \quad (5.9)$$

The time-dependent detected intensity of the horizontally polarized component measured in transmission is given by combining Eqs. (5.3), (5.5), (5.8) and (5.9).

$$I(\tau) \propto |t^+|^2 + |t^-|^2 + 2|t^+||t^-| \cdot \sin(\Delta(\tau) - \delta) \quad (5.10)$$

When A is relatively small, a Taylor series expansion of Eq. (5.10) with respect to τ shown in Eq. (5.11) converges rapidly.

$$I(\tau) \propto 2(|t^+|^2 + |t^-|^2) + 2|t^+||t^-| \cdot \left\{ \begin{array}{l} \left[\begin{array}{l} \left(2A - A^3 + \frac{A^5}{6} - \frac{A^7}{72} + \dots \right) \cdot \sin(2\pi f \tau) \\ + \left(\frac{A^3}{3} - \frac{A^5}{12} + \frac{A^7}{120} + \dots \right) \cdot \sin(3 \cdot 2\pi f \tau) + \dots \end{array} \right] \cdot \cos \delta \\ \left[\begin{array}{l} \left(1 - A^2 + \frac{A^4}{4} - \frac{A^6}{36} + \dots \right) \\ + \left(A^2 - \frac{A^4}{3} + \frac{A^6}{24} + \dots \right) \cdot \cos(2 \cdot 2\pi f \tau) \\ + \left(\frac{A^4}{12} - \frac{A^6}{60} + \dots \right) \cdot \cos(4 \cdot 2\pi f \tau) + \dots \end{array} \right] \cdot \sin \delta \end{array} \right\} \quad (5.11)$$

According to Eq. (5.11), the quadrature components (sine) only map to the odd harmonics of the Taylor series, while the in-phase components (cosine) terms are only present in the even harmonics. The proportionality in Eq. (5.11) evaluated at seventh order will result in negligible errors for the PEM modulation for $A < \pi/2$. In our experiments, the modulation amplitude of the PEM was set as $A = 0.3\pi$, consistent with the range indicated. Retaining the first seven terms of the expansion, the quadrature components (sine, Y) of the first harmonic ($1f$) and the in-phase components (cosine, X) of the second harmonic ($2f$) LIA detection are written as Eqs. (5.12) and (5.13), respectively.

$$1f_Y \approx 2|t^+||t^-| \cdot \left(2A - A^3 + \frac{A^5}{6} - \frac{A^7}{72} \right) \cdot \cos \delta \quad (5.12)$$

$$2f_X \approx -2|t^+||t^-| \cdot \left(A^2 - \frac{A^4}{3} + \frac{A^6}{24} \right) \cdot \sin \delta \quad (5.13)$$

Combining Eqs. (5.12) and (5.13), one can recover values of $\cos \delta$ and $\sin \delta$ from $1f_Y$, $2f_X$, and the PEM modulation amplitude A . Then, δ can be achieved through Eq. (5.14) in a range of $[-\pi, \pi]$.

$$\delta = \text{Im}[\ln(\cos \delta + i \sin \delta)] \quad (5.14)$$

Unlike the HWP rotation strategy, the transmittance image recovered from the LIA detection is defined as $|t^+||t^-|$. It is noteworthy that both the HWP and PEM polarization rotation strategies recover phase values in the range of $[-\pi, \pi]$.

5.3 Results

5.3.1 QP image recovery

Experimental measurements of a 1951 USAF resolution test chart were performed to assess the change in the 3D point spread function induced by the μRA , the results of which are shown in *Figure 5.3*. From the images, the radial extent of the point spread function was evaluated based on edge analysis, in which the derivative of the intensity profile was fit to a Gaussian function to recover the RMS (root mean square) beam width. Plots of the recovered Gaussian beam cross-section are shown in *Figure 5.3* for multiple z-positions of the test grid in order to map the beam profile in all three dimensions assuming cylindrical symmetry. For an object (e.g.,

the test grid) initially in the focal plane of the microscope, addition of the μ RA resulted in a slight blurring. However, crisp images were recoverable upon axial translation of either $\pm 35 \mu\text{m}$. Consistent with this observation, analysis of the images shown in *Figure 5.3(A)* generated by the wavefront shaping of the μ RA produced two foci separate by $70 \mu\text{m}$ symmetrically distributed about the original focal plane [*Figure 5.3(B)*]. Due to analysis of the results summarized in *Figure 5.3*, the cross-sections of the axially offset foci are statistically indistinguishable from the original focus, indicating no substantial perturbation to the point spread function upon addition of the μ RA. Comparison of the point-spread functions between *Figure 5.3(A)* and *Figure 5.3(B)* indicates that the spatial resolution ($\sim 2 \mu\text{m}$) is unchanged by the addition of the μ RAs. The introduction of the large spatial offset between the two foci (roughly $1/4$ of the $250 \mu\text{m} \times 250 \mu\text{m}$ FoV) makes it possible to create a stable and uniform reference plane positioned within a homogeneous medium (e.g., glass, air, or solution) immediately adjacent to the sample plane, removing imaging artifacts arising from the use of sample and reference locations cohabitating in the focal plane as in Nomarski and Zernike phase contrast microscopy.

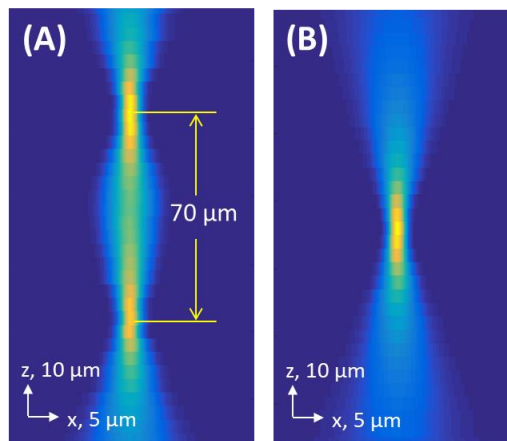


Figure 5.3 Measured point spread functions in the x-z plane with (A) and without (B) the μ RA installed in the beam path.

5.3.2 QPI through HWP rotation

To retrieve the QP images from ADIC imaging using the HWP rotation strategy, a whole set of images was collected with the HWP rotating through a 90-degree range, with the

horizontally polarized transmitted beam detected using a photodiode. The unprocessed images with HWP at different rotation angles showed different contrast as indicated in *Figure 5.4*.

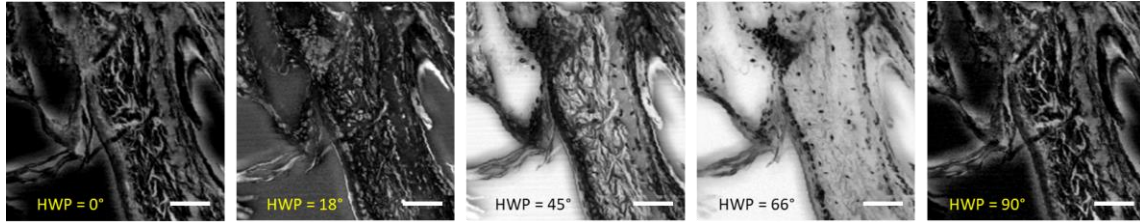


Figure 5.4 Several unprocessed images with different HWP rotation angles.

A pixel-by-pixel nonlinear fit was applied to the intensity trace as a function of the HWP rotation angle γ using Eq. (5.3) to recover images of phase (δ) and transmittance $[\left(|t^+| + |t^-|\right)^2]$. *Figure 5.5(A)* and *Figure 5.5(B)* show the recovered transmittance and QP image from a stained mouse tail section. The areas with larger magnitude phase shift [red and blue areas in *Figure 5.5(B)*] highlight the detailed spatial distribution of the fibrils in mouse tail tissues, which produced low contrast in the retrieved transmittance image. The average intensities of the blank (no sample) areas in the raw ADIC image were used to calibrate the detector sensitivity and the HWP rotation angle used in Eq. (5.3) as shown in *Figure 5.5(C)*. The measured intensity trace and fitted results show excellent agreement, supporting the validity of this calibration strategy. The $\sim 6^\circ$ phase shift in the HWP rotation angle corresponding to the minimum transmitted intensity of the blank is attributed to uncertainty in the μ RA orientations, which were not in precision rotation stages. Fits for quantitative phase retrieval for two representative pixels in the image are shown in *Figure 5.5(D)*, with good agreement between the measurements (dots and stars) and fits (lines). The mean of the sum of squared errors of prediction (SSE) and the coefficient of determination (R^2) for the nonlinear fit for the whole FoV were 0.0018 and 0.9164, respectively. These results indicate the degree of statistical confidence with which the phase angle can be recovered by nonlinear fitting.

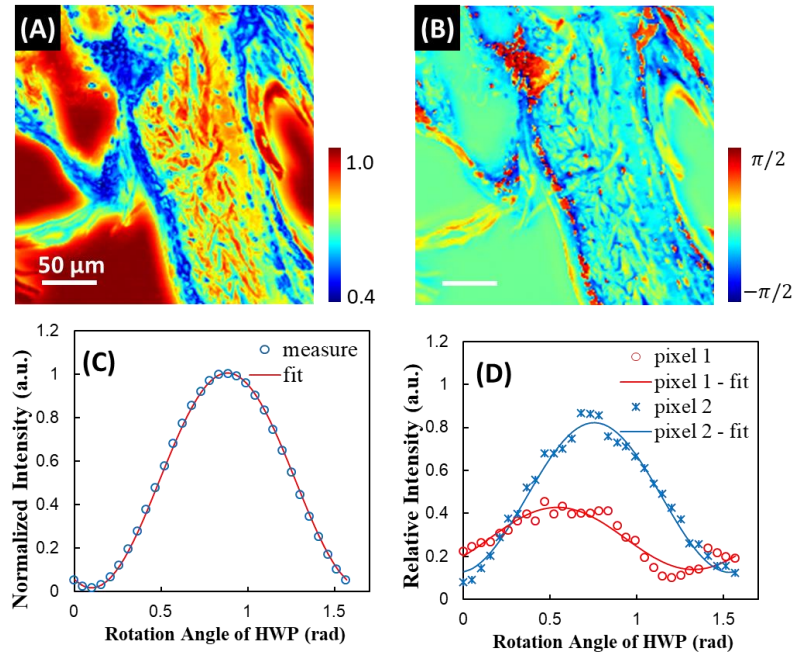


Figure 5.5 Transmittance image (A) and QP images (B) recovered with half wave rotation measurement of a single FoV of mouse tail section. (C) Overlay of the measured intensity of background (dots) with its nonlinear fit result (solid line). (D) Overlay of the measured intensity of random pixels (dots) with its nonlinear fit result (solid line) to recover transmittance image and phase contrast image. Scale bar: 50 μm .

5.3.3 QPI through LIA detection

For LIA detection, both the pure-tone $1f$ (50 kHz) and $2f$ (100 kHz) signals generated by the PEM were used as references for the LIA. The raw images (cosine components and sine components) collected from $1f$ and $2f$ LIA measurements were shown in *Figure 5.6(A) - Figure 5.6(D)* for the same FoV of a mouse tail section. *Figure 5.6(A)* and *Figure 5.6(B)* share the same image contrast settings, as did *Figure 5.6(C)* and *Figure 5.6(D)*. Consistent with the predictions from Eq. (5.11), the cosine components of $1f$ and the sine components of $2f$ produced negligible contrast. The transmittance bright field image [*Figure 5.6(E)*] and QP image [*Figure 5.6(F)*] were calculated using Eqs. (5.12) - (5.14). Similarities were qualitatively clear between the transmittance bright field image and the sine components of $1f$ LIA detection, as well as between the QP image and cosine components of $2f$ LIA detection. According to Eqs. (5.12) and (5.13), the sine components from $1f$ and the cosine components from $2f$ converge to the bright field image and QP image, respectively, in the limit of low phase shifts δ . It can also be seen that the

QP image revealed more detailed structures and exhibited higher contrast for those areas with higher transmittance, such as the fibrils shown in *Figure 5.6(E)* and *Figure 5.6(F)*.

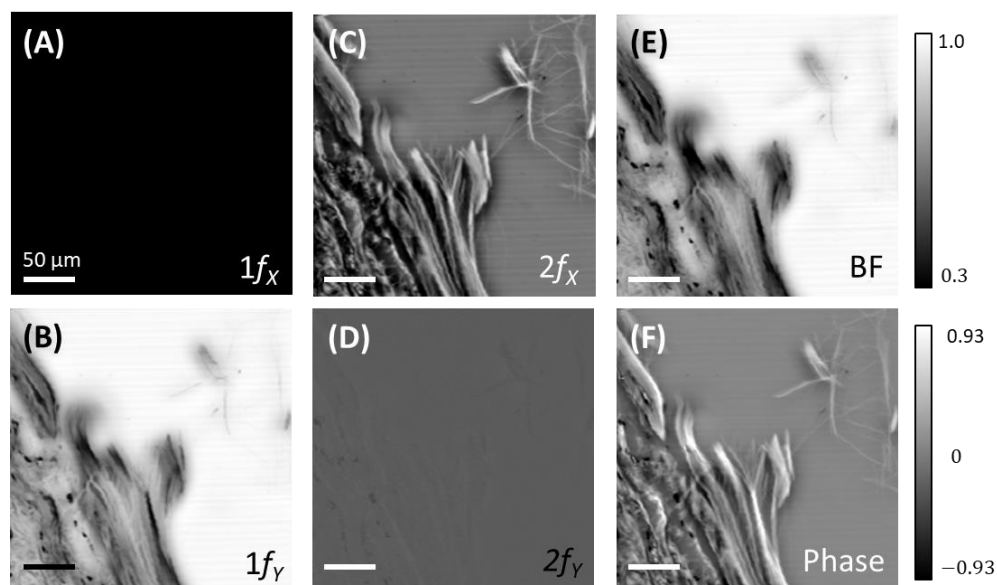


Figure 5.6 Raw images and recovered transmittance and quantitative phase image from LIA detection for a single FoV of mouse tail section. (A, B) and (C, D) are raw images with $1f_x$ and $1f_y$ as reference, respectively. (E) is the recovered transmittance bright field image and (F) is the quantitative phase contrast image. Color bar unit: (E) transmittance percentage, (F) phase shift in radian. Scale bar: $50 \mu\text{m}$.

The agreement between the two QPI strategies applied to the ADIC microscopy, HWP rotation and LIA detection were tested by imaging the same FoV of a mouse tail section as shown in *Figure 5.7*. The transmittance bright field images [*Figure 5.7(A)*] was recovered by nonlinear fitting through the HWP rotation strategy. To compare the retrieved QP images with different approaches [*Figure 5.7(B)* and *Figure 5.7(C)*], same image contrast settings were applied. Agreement between the retrieved results from the two strategies provides cross-validation of both approaches. The difference image in phase shift obtained from the two strategies was shown in *Figure 5.7(D)*. It can be seen that most differences between the two methods arise at the pixels with larger absolute phase shift values. These differences could be attributed to the phase wrapping issue that is sensitive to spherical structures and phase retrieval strategies.

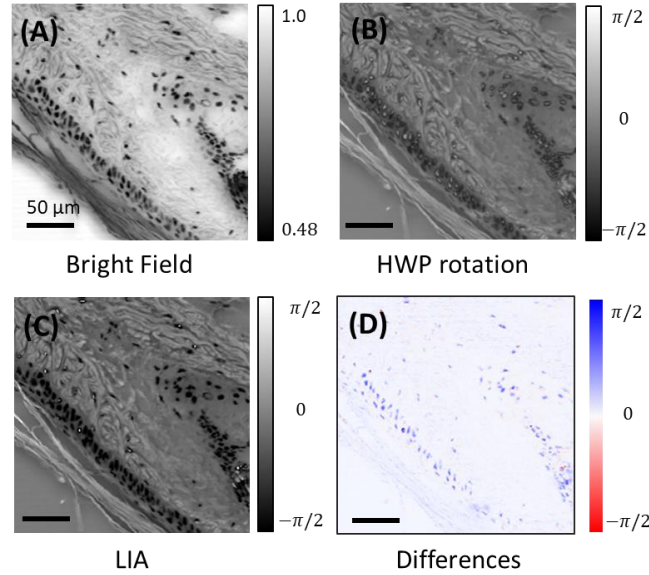


Figure 5.7 Transmittance and quantitative phase contrast images recovered from HWP rotation (A, B) and LIA detection (C) strategies of a single FoV of mouse tail section. (D) Differences images of the phase shift calculated from the two strategies. Color bar unit: (A) transmittance percentage, (B-D) phase shift in radian. Scale bar: 50 μm .

5.4 Discussion

5.4.1 Separation distance between the dual-foci for QPI

The separation distance between the two foci depends on the designed periods of the centric polarization rotation pattern of our μRAs . With smaller periods of the centric modulation pattern in μRA , larger separation is expected. When the separation distance is much smaller, the setup converges to a result qualitatively analogous to Zernike phase contrast, in which only a single ring is included, and the reference plane is so close to the sample plane that the contrast is simply a halo (i.e., the negligible displacement limit). The upper limit for separating the two foci is ultimately dictated by the manufacturing precision of the μRAs ; a higher density of fringes at the extrema of the array corresponds to a larger separation between foci. Manufacture with the maximum stated manufacturing resolution of 30 μm corresponds to a maximum fringe period of 60 μm (with Nyquist sampling), producing a theoretical separation distance of 360 μm for a 10x objective. In this work, a longer maximum period was used to reduce the potential for artifacts from the discretization effects at the extrema, giving a separation distance of 70 μm . By enabling such a large axial offset between the two focal planes, the reference beam is significantly

defocused in the sample plane to a spot size of $\sim 44 \mu\text{m}$ in diameter. As such, the phase shift induced at a given $\sim 3 \mu\text{m}^2$ location within the sample plane is interfered with the average phase within a $\sim 1500 \mu\text{m}^2$ area comprising the cross-sectional area of the reference beam within the sample plane. While not serving as an entirely independent reference as in dual-path QPI, the reference effectively spans the optical phase averaged over an area in the field of view ~ 500 -fold larger than the focal volume using common-path optics. For sparse, well-separated objects such as recorded herein, the phase-bias in the reference path induced by the sample is negligible and two conditions converge.

5.4.2 *Limit of detection (LoD) of ADIC-QPI*

The images produced by ADIC are free of halo and side-lighting artifacts routinely encountered in Zernike and Nomarski phase contrast methods, respectively. The absence of these artifacts arises from the spherical symmetry of the interference condition coupled with the relatively large area within the field of view serving as a phase reference for the sample plane. The limits of detection for the phase shift calculation from the two strategies were investigated by analyzing the QP images obtained from ADIC microscopy in absence of samples. The measured standard deviation (σ) of each phase image retrieved by the HWP rotation and LIA detection strategies was 0.003 rad and 0.011 rad, respectively. Thus the LoD (3σ) of each QPI approach was deduced to be 0.009 rad and 0.033 rad. Considering a thin film of lipid ($n = 1.50$)³²⁻³⁴ in an aqueous environment ($n = 1.33$) measured using ADIC microscopy, the smallest optical path length that could be determined with the two strategies is 4.5 nm and 16.4 nm, respectively. Note the self-calibration of the nonlinear fitting could reduce the $1/f$ noise arising from the long acquisition time in the HWP rotation strategy (about 10 min for a whole set of 90-degree rotation with 6-degree intervals, corresponding to integration time of 480 μs for each pixel). However, the pixel-by-pixel nonlinear fitting leads to the time-consuming data analysis process. Due to the limit capability of the LIA used in our experiments, the $1f$ and $2f$ ADIC raw images were acquired separately with different reference signals. In addition, the LIA integration time used in our experiments were limited to 30 μs (3 modulation periods). The ~ 3 -fold improvement in the phase uncertainty using HWP rotation is attributed to the ~ 16 -fold increase in per-pixel measurement time relative to the PEM measurement. Significant improvements are

reasonable to expect using longer integration times with simultaneous LIA detection of the $1f$ and $2f$ signals.

5.4.3 Recovery of refractive index of microspheres

Silica beads $8\ \mu\text{m}$ in diameter were used for quantitative phase imaging and to calculate the refractive index of the silica beads. *Figure 5.8* shows the QP images for the same FoV of $8\ \mu\text{m}$ silica beads retrieved from both HWP rotation and LIA strategies. Great agreement can be seen between the results of the two strategies [*Figure 5.8(A)* and (*B*)]. The refractive index of silica microbeads was calculated based on the measured phase shift and bead size. The phase shift line profile of a single bead [insets of *Figure 5.8(A)* and (*B*)] obtained from both strategies are plotted in *Figure 5.8(C)*. The phase shift (δ) in the center of the measured $7.3\ \mu\text{m}$ silica bead was 2.53 radian. Statistical analysis of silica microspheres in *Figure 5.8* allows us to calculate the difference between the refractive indices of silica bead and nitrocellulose matrix: $\Delta n = \delta\lambda/2\pi D = 0.0293 \pm 0.0007$. Given the refractive index of nitrocellulose is 1.505 at $543.5\ \text{nm}$ ³⁵, the refractive index of silica bead is calculated as 1.4757 ± 0.0007 at $532\ \text{nm}$. Although there is no report on the optical constants of silica microparticles, the result is consistent with the refractive index of amorphous bulk silica as 1.461 ³⁶.

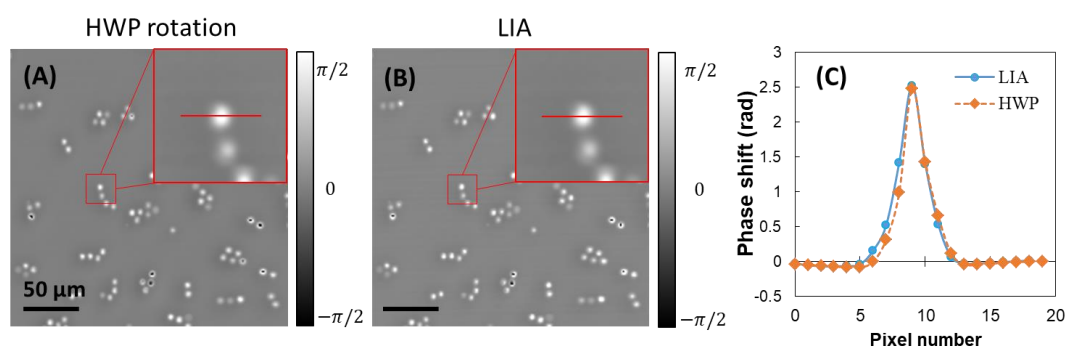


Figure 5.8 Quantitative phase contrast images of the same FoV of $8\ \mu\text{m}$ silica beads recovered from both HWP rotation (A) and LIA detection (B) strategies. Color bar unit: phase shift in radian. Scale bar: $50\ \mu\text{m}$. Inserts: zoom-in for one single bead. (C) Phase shift line profiles of the cross line in the insets retrieved from the HWP rotation (blue dots) and LIA detection (orange squares) approach.

5.5 Conclusion

A quantitative phase contrast microscope was developed by ADIC imaging through polarization wavefront shaping via a matched pair of μ RAs. HWP rotation and LIA detection strategies enabled simultaneous recovery of both transmittance and QP images, with good agreement observed between the recovered QP images from both the strategies. The smallest detectable phase shift was determined to be 0.009 radians in HWP rotation strategy with integration time of 480 μ s for each pixel and 0.033 radians in LIA detection strategy with an integration time of 30 μ s for each pixel. Proof of concept studies with tissue samples and silica beads indicated excellent agreements between the quantitative phase shift analysis by both HWP rotation and LIA detection strategies, as well as with the theoretical predictions. The μ RAs can be customized for particular wavelengths and axial offsets between foci, supporting design for application-specific imaging. ADIC was enabled by the addition of two fixed thin optics within an otherwise standard optical path, suggesting broad compatibility for retrofitting into existing commercial microscopes. For the future work, the ADIC has the potential to be extended into a wide field quantitative phase contrast imaging using a broadband and spatially incoherent LED illumination source. In addition, ADIC autocorrelation method was also developed and is described in *CHAPTER 6*.

5.6 References

1. Zernike, F., Phase contrast, a new method for the microscopic observation of transparent objects part II. *Physica* **1942**, 9 (10), 974-986.
2. Zernike, F., How I Discovered Phase Contrast. *Science* **1955**, 121 (3141), 345-349.
3. Georges, N. Interferential polarizing device for study of phase objects. 1960.
4. Dodt, H.-U.; Ziegglänsberger, W., Visualizing unstained neurons in living brain slices by infrared DIC-videomicroscopy. *Brain Research* **1990**, 537 (1), 333-336.
5. Gelles, J.; Schnapp, B. J.; Sheetz, M. P., Tracking kinesin-driven movements with nanometre-scale precision. *Nature* **1988**, 331, 450-453.
6. Allen, R. D.; Allen, N. S.; Travis, J. L., Video-enhanced contrast, differential interference contrast (AVEC-DIC) microscopy: A new method capable of analyzing microtubule-related motility in the reticulopodial network of *allogromia laticollaris*. *Cell Motility* **1981**, 1 (3), 291-302.

7. Ikeda, T.; Popescu, G.; Dasari, R. R.; Feld, M. S., Hilbert phase microscopy for investigating fast dynamics in transparent systems. *Opt. Lett.* **2005**, *30* (10), 1165-1167.
8. D. Gabor, D.-I., Microscopy by reconstructed wave-fronts. *Proceedings of the Royal Society of London. Series A. Mathematical and Physical Sciences* **1949**, *197* (1051), 454.
9. Zhang, T.; Yamaguchi, I., Three-dimensional microscopy with phase-shifting digital holography. *Opt. Lett.* **1998**, *23* (15), 1221-1223.
10. Mann, C. J.; Yu, L.; Lo, C.-M.; Kim, M. K., High-resolution quantitative phase-contrast microscopy by digital holography. *Opt. Express* **2005**, *13* (22), 8693-8698.
11. Kim, M. K., Digital holographic microscopy. In *Digital Holographic Microscopy*, Springer: 2011; pp 149-190.
12. Miccio, L.; Finizio, A.; Puglisi, R.; Balduzzi, D.; Galli, A.; Ferraro, P., Dynamic DIC by digital holography microscopy for enhancing phase-contrast visualization. *Biomed. Opt. Express* **2011**, *2* (2), 331-344.
13. Goodman, J. W.; Lawrence, R. W., DIGITAL IMAGE FORMATION FROM ELECTRONICALLY DETECTED HOLOGRAMS. **1967**, *11* (3), 77-79.
14. Wang, Z.; Millet, L.; Mir, M.; Ding, H.; Unarunotai, S.; Rogers, J.; Gillette, M. U.; Popescu, G., Spatial light interference microscopy (SLIM). *Opt. Express* **2011**, *19* (2), 1016-1026.
15. Popescu, G.; Ikeda, T.; Dasari, R. R.; Feld, M. S., Diffraction phase microscopy for quantifying cell structure and dynamics. *Opt. Lett.* **2006**, *31* (6), 775-777.
16. Bhaduri, B.; Pham, H.; Mir, M.; Popescu, G., Diffraction phase microscopy with white light. *Opt. Lett.* **2012**, *37* (6), 1094-1096.
17. Bhaduri, B.; Edwards, C.; Pham, H.; Zhou, R.; Nguyen, T. H.; Goddard, L. L.; Popescu, G., Diffraction phase microscopy: principles and applications in materials and life sciences. *Adv. Opt. Photon.* **2014**, *6* (1), 57-119.
18. Zheng, G.; Horstmeyer, R.; Yang, C., Wide-field, high-resolution Fourier ptychographic microscopy. *Nature Photonics* **2013**, *7*, 739.
19. Jesacher, A.; Harm, W.; Bernet, S.; Ritsch-Marte, M., Quantitative single-shot imaging of complex objects using phase retrieval with a designed periphery. *Opt. Express* **2012**, *20* (5), 5470-5480.
20. Tian, L.; Waller, L., 3D intensity and phase imaging from light field measurements in an LED array microscope. *Optica* **2015**, *2* (2), 104-111.
21. McIntyre, T. J.; Maurer, C.; Fassel, S.; Khan, S.; Bernet, S.; Ritsch-Marte, M., Quantitative SLM-based differential interference contrast imaging. *Opt. Express* **2010**, *18* (13), 14063-14078.
22. Chapman, H. N.; Nugent, K. A., Coherent lensless X-ray imaging. *Nature Photonics* **2010**, *4*, 833.

23. Hartman, J. S.; Gordon, R. L.; Lessor, D. L., Nomarski differential interference contrast microscopy for surface slope measurements: an examination of techniques. *Appl. Opt.* **1981**, *20* (15), 2665-2669.
24. Susumu, S., Liquid-Crystal Lens-Cells with Variable Focal Length. *Japanese Journal of Applied Physics* **1979**, *18* (9), 1679-1684.
25. Ren, H.; Fox, D. W.; Wu, B.; Wu, S.-T., Liquid crystal lens with large focal length tunability and low operating voltage. *Opt. Express* **2007**, *15* (18), 11328-11335.
26. Ren, H.; Fan, Y.-H.; Wu, S.-T., Prism grating using polymer stabilized nematic liquid crystal. **2003**, *82* (19), 3168-3170.
27. Sun, J.; Xu, S.; Ren, H.; Wu, S.-T., Reconfigurable fabrication of scattering-free polymer network liquid crystal prism/grating/lens. **2013**, *102* (16), 161106.
28. Rumiko, Y.; Toshiaki, N.; Susumu, S., Liquid Crystal Polarizers with Axially Symmetrical Properties. *Japanese Journal of Applied Physics* **1989**, *28* (9R), 1730-1731.
29. Yoriko Morita; Jay, E. S.; Kristina, M. J.; Eckhard Hanelt; Frank Sandmeyer, Active Liquid Crystal Devices Incorporating Liquid Crystal Polymer Thin Film Waveplates. *Japanese Journal of Applied Physics* **1999**, *38* (1R), 95-100.
30. Woltman, S. J.; Jay, G. D.; Crawford, G. P., Liquid-crystal materials find a new order in biomedical applications. *Nature Materials* **2007**, *6*, 929-938.
31. Serak, S. V.; Roberts, D. E.; Hwang, J.-Y.; Nersisyan, S. R.; Tabiryan, N. V.; Bunning, T. J.; Steeves, D. M.; Kimball, B. R., Diffractive waveplate arrays [Invited]. *J. Opt. Soc. Am. B* **2017**, *34* (5), B56-B63.
32. Ohki, S., Dielectric constant and refractive index of lipid bilayers. *Journal of Theoretical Biology* **1968**, *19* (1), 97-115.
33. Huang, W.; Levitt, D. G., Theoretical calculation of the dielectric constant of a bilayer membrane. *Biophysical Journal* **1977**, *17* (2), 111-128.
34. Tiffany, J. M., Refractive index of meibomian and other lipids. *Current Eye Research* **1986**, *5* (11), 887-889.
35. Cui, Y.; Azzam, R. M. A., Determination of the refractive index and thickness of transparent pellicles by use of the polarization-independent absentee-layer condition. *Appl. Opt.* **1996**, *35* (25), 5040-5043.
36. Malitson, I. H., Interspecimen Comparison of the Refractive Index of Fused Silica. *J. Opt. Soc. Am.* **1965**, *55* (10), 1205-1209.

CHAPTER 6. ADIC CORRELATION SPECTROSCOPY (ADIC-CS)

Axially-offset differential interference contrast correlation spectroscopy (ADIC-CS) was developed for analysis of particle size distribution and quantitative phase retrieval by producing and coherently recombining light from a pair of axially-offset focal planes. ADIC presented in CHAPTER 5 was used to generate and recombined two axially-offset foci with orthogonal polarizations. Particles drifting through one of the foci led to signal changes at the detector. Fast digitization enabled digital lock-in analysis to recover the quantitative phase changes and intensities fluctuations as a function of time. Autocorrelograms were generated through correlation spectroscopy similar as the dynamic light scattering (DLS) methods to extract particle size information.

6.1 Introduction

Macromolecular structure determination is the foundation of rational drug design through atomistic understanding of structure and function relationship.¹⁻⁴ However, the difficulties of obtaining large protein single crystals for diffraction analysis result in the rising trend of using smaller and smaller protein crystals in serial crystallography. Meanwhile, protein aggregation plagues delivery of therapeutic biological macromolecules and protein structure determination by crystallography. Early detection of aggregation can help reduce overall analysis time by reducing pre-screening to discriminate ordered protein nanocrystals from disordered aggregates. Dynamic light scattering (DLS) is commonly used for particle size analysis and aggregation detection in suspensions or solution by recoding the time-dependent intensity fluctuations followed by autocorrelation analysis.^{5,6} Since only scattering intensity is recorded, DLS lacks the sensitivity for early stages of aggregation, given the subtle refractive index difference between proteins and water. In this chapter, axially-offset differential interference contrast correlation spectroscopy (ADIC-CS) is introduced as an alternative approach for particle analysis in fluidic medium via polarization wavefront shaping for quantitative phase retrieval as detailed in CHAPTER 5.

The ADIC-CS simultaneously recovers particle size distributions and refractive index information from the nanocrystal suspensions by producing and coherently recombining light from a pair of axially-offset focal planes. The same μ RAs as detailed in CHAPTER 5 were used

for producing and coherently recombining light from the paired axially-offset focal planes.⁷ With linearly polarized incident light, the polarization pattern resulting from the μ RA was identical to that produced by the interference between a slightly diverging RCP plane wave and a slightly converging LCP plane wave, as demonstrated in *Figure 6.1(A)*. When focusing through the same objective, two axially offset foci were generated from the two circular polarized components along the optical axis (z -axis). For quantitative phase retrieval, the two focal planes serve as the sample and reference planes, respectively. After passing through another matched μ RA, the two orthogonal polarized components were coherently recombined as one collimated beam. In absence of the sample, the recombined collimated beam had the same linearly polarized plane wavefront as the incident light, corresponding to a minimum in the intensity detected through a polarizer crossed with the incident polarization.

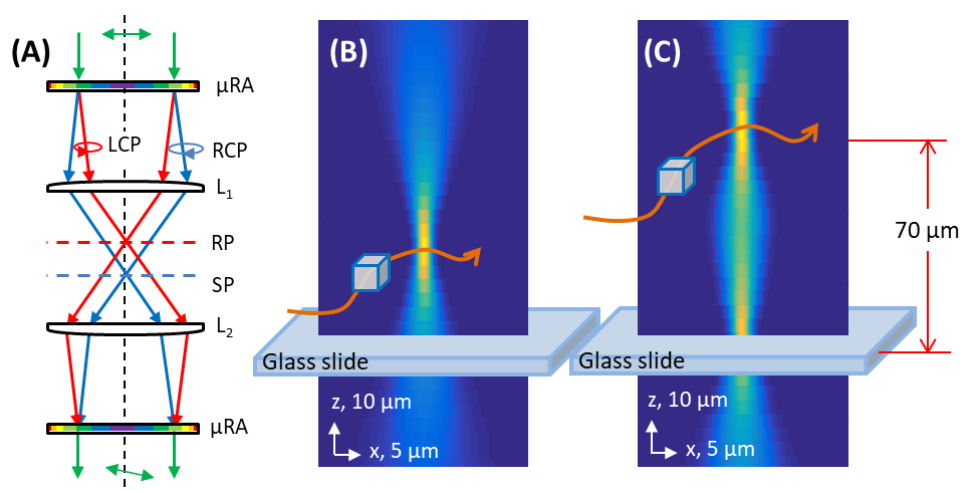


Figure 6.1 The working principle of ADIC-CS. (A) Two focus planes were generated and recombined by two μ RA. L1 and L2: lens; RP: reference plane; SP: sample plane; Black dash line: optic axis (z -axis). Modified measured point spread functions in the x - z plane without (B) and with (C) the μ RA in the beam path.

As shown in *Figure 6.1(C)*, the two axially-offset focus planes distributed symmetrically about the original one *Figure 6.1(B)* when the μ RA was out of the optic path. In the current design of μ RA, the reference plane and sample plane were separated in a distance of 70 μ m with a 10x objective. For ADIC-CS measurement, the bottom focus plane was placed in a uniform medium (a glass slide) serving as reference. When particles (protein crystals or aggregates) translated through the sample plane, the polarization state and intensity of the recombined beam

changed, producing intensity modulation at the detector. By rapid polarization modulation of the incident light, digital lock-in detection of the harmonics of the transmitted beam enabled absolute phase determination of the diffusing particle through the sample focal volume. Autocorrelograms of both quantitative phase and intensity change from the sample were generated after the digital lock-in analysis to retrieve the particle size distribution. The ability to utilize the intrinsic phase contrast mechanism arising from differences in refractive index provided this method with label-free sensitive particle analysis.

6.2 Method

6.2.1 Instrumentation for ADIC-CS

ADIC-CS microscope was constructed based on a bright field microscope with the addition of several polarizing optics as described in *CHAPTER 5*, coupled with a fast digital lock-in detector. As shown in *Figure 6.2*, a 532 nm continuous laser (Millenia Vs J) was used for illumination with horizontally polarization incident light, followed with a half wave plate (HWP), a photoelastic modulator (PEM, Hinds instrument PEM-90M) and a quarter wave plate (QWP). The beam was expanded to 15 mm in diameter to fill the full aperture of a 10x objective (0.3 NA, Nikon). A 3-dimension translational stage was used for sample positioning. An identical 10x objective was used as a condenser in transmittance, followed by a paired μ RA positioned and oriented to recover the incident polarization state.

For recovery of both intensity and phase changes with digital lock-in amplification, HWP, PEM, and QWP were rotated at 22.5° , 0° and 45° , respectively, to deliver linearly polarized light modulated in the rotation angle to the μ RA. Crossed (vertically) polarized transmittance was detected by passing the beam through a polarizer and a photodiode (Thorlabs DET-10A). Signals from the photodiode, $1f$ (50 kHz) and $2f$ (100 kHz) reference signals from the PEM were digitized simultaneously at 2 MHz using a PCI-E digitizer oscilloscope cards (AlazarTech ATS-9416) with different duration times varied from 1 min to 15 min. The quantitative phase and intensity fluctuations as a function of time were then recovered with a digital lock-in with a custom program (MATLAB) with an integration time of 5 ms per time-point.

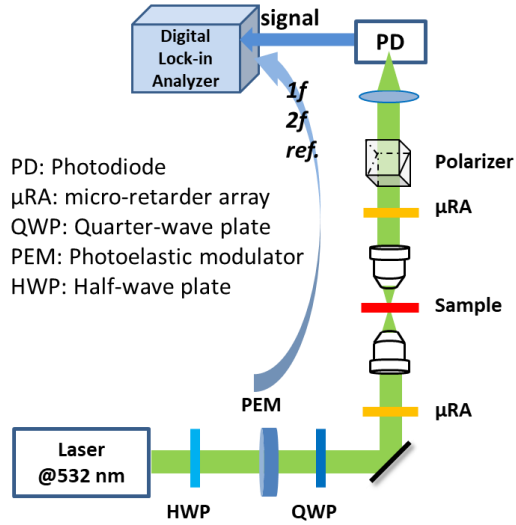


Figure 6.2 Instrumentation for ADIC-CS with a 10x objective. Signals were collected in cross polarization states of the linearly polarized incident light with a fast digitizer for digital lock-in analysis.

6.2.2 Sample preparation

Silica microbeads (donated by Prof. Mary Wirth, Purdue University, West Lafayette, IN) with different diameters were dispersed by ultrasonication in deionized water. For correlation spectroscopy, 50 μ L of beads suspension was sealed between a hydrophobic glass slide and a conventional coverslip.

6.3 Result and discussion

6.3.1 Mathematical simulation and baseline drifting

Simultaneous autocorrelograms of both intensity and phase were acquired with digital lock-in detection, as detailed in *CHAPTER 5*. When detecting the crossed polarized transmittance, the signal intensity from photodiode as a function of time is described by Eq. (6.1). The t^+ and t^- describe the field detected following interaction in the two foci separately, with the phase change δ induced by the sample.⁷ The retardance modulation $\Delta(\tau)$ introduced by the PEM is defined in Eq. (6.2) as a function of time (τ) and a modulation amplitude of $2A$ while $A = 0.3\pi$, and the modulation frequency $f = 50$ kHz.

$$I(\tau) \propto |t^+|^2 + |t^-|^2 - 2|t^+||t^-| \cdot \sin(\Delta(\tau) - \delta) \quad (6.1)$$

$$\Delta(\tau) = 2A \cdot \sin(2\pi f \tau) \quad (6.2)$$

The phase and transmittance (defined as $|t^+||t^-|$) changes at the sample can be recovered through digitized lock-in with the $1f$ and $2f$ signals from PEM as the reference, as shown in Eqs. (6.3) - (6.5), in which $1f_Y$ is the quadrature components of the first harmonic and $2f_X$ is the in-phase components of the second harmonic.

$$1f_Y \approx 2|t^+||t^-| \cdot \left(2A - A^3 + \frac{A^5}{6} - \frac{A^7}{72} \right) \cdot \cos \delta \quad (6.3)$$

$$2f_X \approx -2|t^+||t^-| \cdot \left(A^2 - \frac{A^4}{3} + \frac{A^6}{24} \right) \cdot \sin \delta \quad (6.4)$$

$$\delta = \text{Im}[\ln(\cos \delta + i \sin \delta)] \quad (6.5)$$

Figure 6.3(B) shows a mathematical simulation of the detected intensity from the photodiode with assumed phase and intensity changes induced by the sample as functions of time, as shown in Figure 6.3(A). The detected intensity time trace can be calculated as shown in Figure 6.3(B). When an integration time of 5 ms was applied for the demodulation, the recovery phase and intensity change introduced by the sample were plot in Figure 6.3(C), with a great agreement with the theoretical ones. It should be noticed that the recovered and theoretical intensity had the same trace shape as a function of time but with different values.

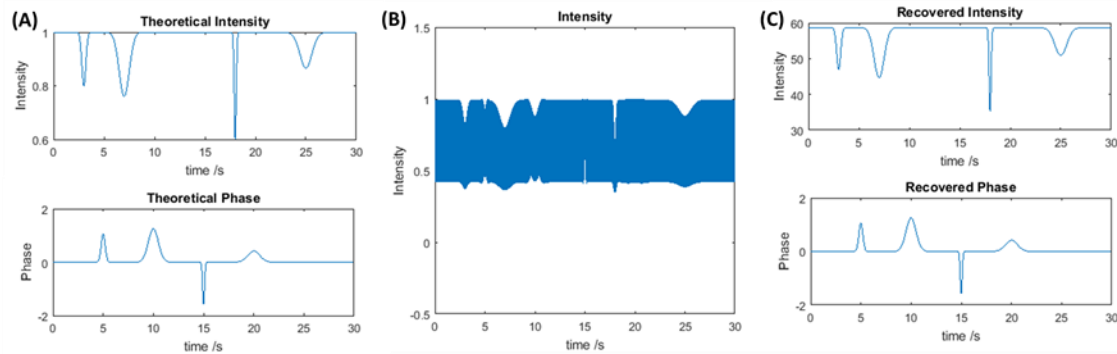


Figure 6.3 Mathematical framework simulation of ADIC-CS. (A) An arbitrary trace of phase changes introduced by sample as a function time. (B) Simulated detected intensity as a function of time. (C) Recovered phase trace from simulated digitized lock-in demodulation.

A nonzero baseline phase difference between the (+) and (-) focal planes was observed in the absence of a sample. One possible explanation is that the two orthogonal polarized beams have a subtle difference in angle upon passing through the glass substrate, leading to a phase shift due to the optical path difference. Considering the maximum acceptance angle as an upper limit for describing the wavefront propagation, the phase shift for a 1 mm glass slide is as significant as 3π as shown in *Figure 6.4*. The baseline phase shift $\Delta\delta$ was calculated from the different optical path lengths for the two polarized components. In practice, subtle manufacturing and sample preparation disparities result in constant or slowly varying phase shift.

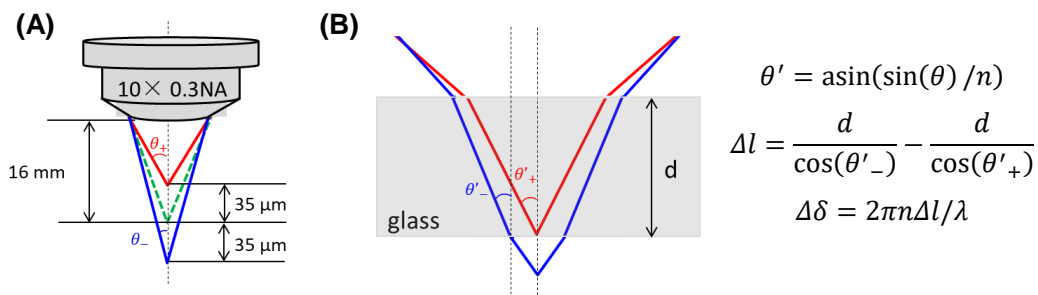


Figure 6.4 Baseline shift induced from the glass slide. (A) Generation of two foci without sample or glass slide. Red/blue solid lines: RCP and LCP components, separately. Green lines: original focal point without μ RA in the beam path. (B) Beam path change induced by insert of a glass slide with a thickness of d , with n as the refractive index of glass as 1.5 and λ as the applied wavelength.

6.3.2 Particle size analysis using correlation spectroscopy

Silica beads with different sizes were used for assessment of ADIC-CS. Recovered quantitative phase and transmittance intensity fluctuation traces of silica beads with 680 nm and 1.5 μm in diameter are shown in *Figure 6.5*. The normalized autocorrelograms calculated from quantitative phase and transmittance intensity tracks are plotted in solid lines in *Figure 6.5(E)* and *Figure 6.5(F)*, respectively. It can be noticed that the decay coefficient is larger for smaller beads as a prediction based Eq. (6.6). The temporal autocorrelogram of the three-dimensional free diffusion suspension is a function of time τ and characteristic diffusion time τ_d .⁸

$$G(\tau, \tau_d) = A \cdot \left(1 + \frac{\tau}{\tau_d}\right)^{-1} \cdot \left[1 + \left(\frac{w_0}{w_z}\right)^2 \frac{\tau}{\tau_d}\right]^{-1/2} + B \quad (6.6)$$

$$\tau_d = \frac{3\pi\eta w_0^2 d}{4k_B T} \quad (6.7)$$

To recover the particle size, the autocorrelograms were normalized with the form that $A = 1$ and $B = 0$. Then the value of τ_d is related to the particle diameter d as described in Eq. (6.7), in which the w_0 and w_z are the beam waist in the radial and axial directions, respectively. For theoretical predictions, w_0 and w_z were set as $0.5 \mu\text{m}$ and $2 \mu\text{m}$ based on prediction of the focal volume of a 10×0.3 NA objective for 532 nm incident light. Viscosity (η) of water at $25 \text{ }^\circ\text{C}$ (temperature, T) are used as $10^{-2} \text{ N}\cdot\text{s}/\text{m}^2$. The predicted results are plotted in *Figure 6.5* as dash lines, which have an agreement with the measurements. The fluctuation for the asymptotic value in measurement results is tentatively attributed to electronic noise.

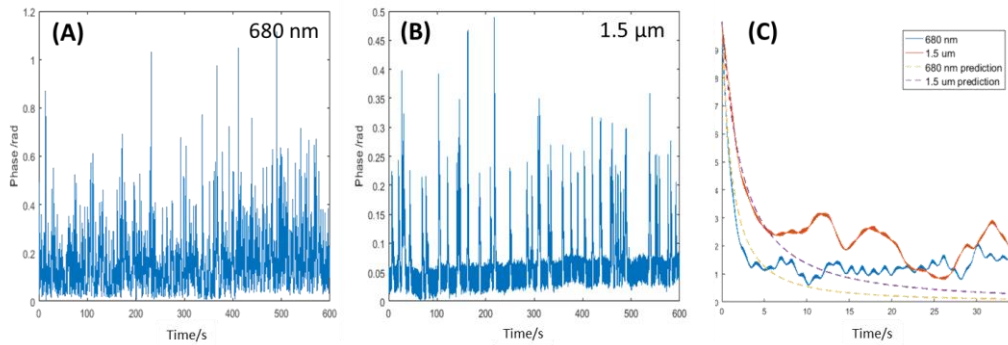


Figure 6.5 Intensity and phase change traces as a time of function after digital lock-in analysis. Phase shifting traces with 10 min duration are plotted for both 680 nm (A) and $1.5 \mu\text{m}$ (B) silica beads. (C) Autocorrelograms for 680 nm and $1.5 \mu\text{m}$ silica beads drifting with the theoretical predictions.

6.4 Conclusion

ADIC-CS was developed for analysis of particle size and refractive index distribution and quantitative phase retrieval by producing and coherently recombining light from a pair of axially-offset focal planes. The two foci separated by $70 \mu\text{m}$ with a $10\times$ objective were produced through polarization wavefront shaping using a matched pair of μRAs . The autocorrelogram were retrieved from both intensity and quantitative phase tracks from the digital lock-in analysis with a fast incident polarization modulation. Future study will focus on retrieval of quantitative

phase information from the ununiformed autocorrelogram. Recovery of refractive index of the diffusing particles is theoretically feasible and will be experimentally tested in the future continuous studies. Compared with DLS providing only particle size distribution analysis, this strategy can provide extra dimension information as phase shift or refractive index of the diffusing particles, making it more suitable for dynamic analysis of protein aggregation or crystallization.

6.5 References

1. Newman, J. A.; Zhang, S.; Sullivan, S. Z.; Dow, X. Y.; Becker, M.; Sheedlo, M. J.; Stepanov, S.; Carlsen, M. S.; Everly, R. M.; Das, C., Guiding synchrotron X-ray diffraction by multimodal video-rate protein crystal imaging. *Journal of synchrotron radiation* **2016**, *23* (4), 959-965.
2. McPherson, A., Preparation and analysis of protein crystals. **1982**.
3. Chapman, H. N.; Nugent, K. A., Coherent lensless X-ray imaging. *Nature Photonics* **2010**, *4*, 833.
4. Chapman, H. N.; Fromme, P.; Barty, A.; White, T. A.; Kirian, R. A.; Aquila, A.; Hunter, M. S.; Schulz, J.; DePonte, D. P.; Weierstall, U. J. N., Femtosecond X-ray protein nanocrystallography. **2011**, *470* (7332), 73.
5. Berne, B. J.; Pecora, R., *Dynamic light scattering: with applications to chemistry, biology, and physics*. Courier Corporation: 2000.
6. Wardell, K.; Jakobsson, A.; Nilsson, G. E. J. I. T. o. b. E., Laser Doppler perfusion imaging by dynamic light scattering. **1993**, *40* (4), 309-316.
7. Ding, C.; Li, C.; Deng, F.; Simpson, G. J., Axially-offset differential interference contrast microscopy via polarization wavefront shaping. *Opt. Express* **2019**.
8. Dow, X. Y.; Dettmar, C. M.; DeWalt, E. L.; Newman, J. A.; Dow, A. R.; Roy-Chowdhury, S.; Coe, J. D.; Kupitz, C.; Fromme, P.; Simpson, G. J., Second harmonic generation correlation spectroscopy for characterizing translationally diffusing protein nanocrystals. *Acta Crystallographica Section D-Structural Biology* **2016**, *72*, 849-859.

CHAPTER 7. POLARIZATION-WAVEFRONT SHAPING FOR RAPID VOLUMETRIC IMAGING

The possibility of using polarization wavefront shaping method to achieve rapid volumetric imaging from multiple focus planes was presented theoretically. Two or three focal planes are generated simultaneously with a designed wavefront shaping optics inserted in the beam path with the same objective based on the incident light wavelength. The polarization states among these focal planes are different and related with the incident light. Fast modulation of the incident polarization states is predicted to result in the intensity distribution among these separated focal planes, leading to the potential for rapid volumetric imaging after demultiplexing.

7.1 Introduction

Volumetric imaging enables measurements of the biologics distribution in animal models, which serve as predictors for *in vivo* performance in humans. Diffusion and transport measurements often require repeated characterization of different parts of the same sample section with precise timing control. Simultaneous image acquisition from multiple focal planes followed by de-multiplexing to form a volumetric intensity map is largely immune to motion-driven artifacts in *in vivo* assays of mobility and bioavailability within animal models.

The most common approach for volume imaging is achieved through *z*-scan, in which images are acquired at different *z* positions by moving the objective or the sample. As a result, *z*-scan generally does not have enough temporal resolution to overcome *in vivo* motion blur. Recently, electrically-controllable liquid-crystal varifocal lens and acoustically driven optofluidic lens have been used for volume imaging.^{1, 2} The use of electrically or acoustically driven lens results to a volume imaging in a range of several micrometers in the sample along the *z*-direction.

In this Chapter, the possibility for rapid volumetric imaging from multifocal imaging using polarization wavefront shaping method is presented theoretically. According to the theoretical prediction, two or three focal planes with different polarization states can be generated simultaneously with a designed wavefront shaping optics inserted in the beam path and tunable incident wavelength. Under fast polarization modulation of the incident light, the intensity

distribution among the separated focal planes varied as a function of time, leading to the potential application for rapid volumetric imaging.

7.2 Theoretical framework

7.2.1 Polarization wavefront shaping and multiple focal planes generation

Polarization wavefront shaping provides a handle often neglected in previous multifocal microscopy methods. The rapid development of waveplate arrays, such as liquid crystal polymer waveplates, allows the tailoring of the polarization state of light on a per pixel basis. As a result, the geometrical phase modulation can be accurately controlled by designing the orientation of liquid crystal polymers on thin polymer substrates. The microretarder array (μ RA) provides the possibilities for accurate design and manufactory of wavefront shaping. As mentioned in *CHAPTER 5*, a linearly polarized incident beam can be viewed as a coherent combination of two orthogonally polarized components. The overlay of the wavefront generated from a converging LCP and diverging RCP light is identical to the wavefront that generated from a linear polarized plane wave through a μ RA with a Fresnel lens pattern. The generation of two axially off-set foci as described in *CHAPTER 5* provides inspiration for simultaneously 3D imaging with two or more axially off-set foci.

To generate multiple foci, a spatially modulated μ RA (similar with a custom designed waveplate) is needed. Considering the most general case, given a general waveplate inserted in the beam path before the objective, the Jones vector describing the light delivered into the objective can be expressed as Eq. (7.1), in which δ is the retardance of the waveplate and γ is the fast axis rotation angle of the waveplate.

$$\bar{e}_{obj} = \begin{bmatrix} \cos \gamma & -\sin \gamma \\ \sin \gamma & \cos \gamma \end{bmatrix} \begin{bmatrix} e^{-i\delta/2} & 0 \\ 0 & e^{i\delta/2} \end{bmatrix} \begin{bmatrix} \cos \gamma & \sin \gamma \\ -\sin \gamma & \cos \gamma \end{bmatrix} \cdot \bar{e}_{in} \quad (7.1)$$

With the Jones vector for incident light is described as $\bar{e}_{in} = [a \ b]^T$, Eq. (7.1) can be rewritten in the form as shown in Eq. (7.2) by simplification with the Euler's formula. With a purely polarized incident light, three components with different polarization states can be addressed: left circular polarized (LCP) component, right circular polarized (RCP) component and the residue component of the exact same polarization state with incident light.

$$\begin{aligned}
\bar{e}_{obj} = & -i \cdot \sin \frac{\delta}{2} \cdot (a + bi) \frac{e^{i2\gamma}}{2} \begin{bmatrix} 1 \\ i \end{bmatrix} \\
& + \cos \frac{\delta}{2} \begin{bmatrix} a \\ b \end{bmatrix} \\
& -i \cdot \sin \frac{\delta}{2} \cdot (a - bi) \frac{e^{-i2\gamma}}{2} \begin{bmatrix} 1 \\ -i \end{bmatrix}
\end{aligned} \tag{7.2}$$

With a μ RA with a spatially varied orientation, different effects are applied on the three components due to the different overall phase terms ($e^{i2\gamma}$ and $e^{-i2\gamma}$). As shown in *Figure 7.1(A)*, the μ RA designed with a Fresnel lens pattern serves as a concave lens for LCP component and a convex lens for RCP component at the same time. When focused with the same objective, the three components will be separated and focused onto different positions in z-axis as shown in *Figure 7.1(B)*. Focus (+) and (-) are RCP and LCP components, respectively, while focus (0) is the one with the same polarization states as the incident light.

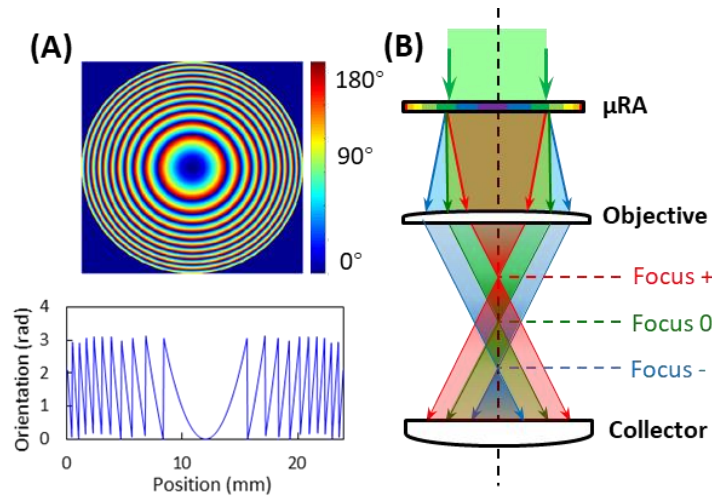


Figure 7.1 Working principles of the rapid multifocal imaging using wavefront shaping. (A) Designed μ RA with the different orientation of the fast axis of half retardance at each pixel. Bottom: cross profile of the μ RA. (B) Three foci were generated after the objective with a specific incident wavelength.

The Jones vector describing the electric fields at the three focal planes can be expressed in Eq. (7.3), so that the intensity distribution among the three focal planes is related to the incident light polarization and the relative retardance (δ) of the μ RA to the applied incident wavelength. For a linearly polarized incident light, a and b are both real, and the (+) and (-) focal planes

have the same intensity but with different ratio compared to the (0) focal plane based on the different value of δ .

$$\begin{aligned}\bar{e}_+ &= -i \cdot \sin \frac{\delta}{2} \cdot (a + bi) \frac{e^{i2\gamma}}{2} \cdot \begin{bmatrix} 1 \\ i \end{bmatrix} \\ \bar{e}_0 &= \cos \frac{\delta}{2} \cdot \begin{bmatrix} a \\ b \end{bmatrix} \\ \bar{e}_- &= -i \cdot \sin \frac{\delta}{2} \cdot (a - bi) \frac{e^{-i2\gamma}}{2} \cdot \begin{bmatrix} 1 \\ -i \end{bmatrix}\end{aligned}\quad (7.3)$$

7.2.2 Separation distance and power distribution among the multiple focal planes

The μ RA with a zero-order half-wave retardance of 1064 nm light was used with a wavelength tunable Spectra-Physics MaiTai Ti:sapphire laser (SpectraPhysics). When tuning the applied wavelength (λ), the relative retardance (δ) of the μ RA agrees with Eq. (7.4).

$$\delta = \frac{1064nm}{2} \cdot \frac{2\pi}{\lambda} \quad (7.4)$$

The azimuthal orientation map of the μ RA was designed as a function of x, y position as shown in Eq. (7.5), in which r is the active radius 12 mm, f is the focal length as 6.28 m and λ is the wavelength as 1064 nm. For RCP components with the overall phase terms as $e^{i2\gamma}$, the μ RA worked equally as a convex lens with a positive f . For LCP components with the overall phase terms as $e^{-i2\gamma}$, the μ RA worked equally as a concave lens with the same focal length but a negative value of f . The separation distance (Δz) between the separated (+) and (-) focal planes agreed with Eq. (7.6), in which f_{obj} is the working distance (focal length) of the applied objective. When using a 10 \times objective (0.3 NA, Nikon), $f_{obj} = 16mm$.

$$\gamma(x, y) = 2\pi[(x - r)^2 + (y - r)^2] / 4f\lambda \quad (7.5)$$

$$\Delta z = \frac{2f_{obj}^2}{f^2 - f_{obj}^2} \quad (7.6)$$

The second harmonic generation (SHG) signals from z-cut quartz were used as an indicator to localize the axial position of the focal volume. The μ RA was inserted in the back aperture of the objective. With the same horizontally polarization, the measured SHG intensity from the z-cut quartz was plotted in *Figure 7.2(A)* as a function of z-position under different wavelength illumination. When the applied wavelength approached the designed wavelength as 1064 nm, the

(0) focal plane shifted to the separated (+) and (-) focal planes with the separation distance Δz . The measured intensity ratio between I_0 and I_+ is plotted in *Figure 7.2(C)* with a good agreement with the theoretical prediction (dash line). To generate three equally distributed focal planes, the designed retardance was $\delta = \cos^{-1}(-1/3)$ to the applied wavelength. For the demonstrated μ RA, the target applied wavelength for three equal powered focal planes is predicted as 764.5 nm based on Eq. (7.4).

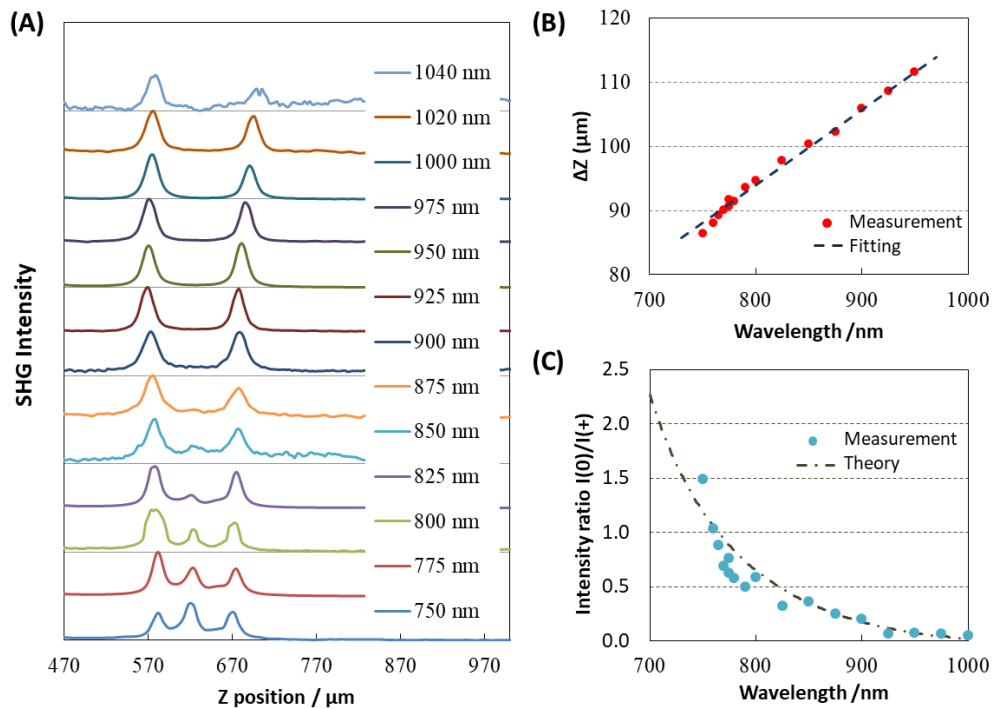


Figure 7.2 The power distribution and separation distance among the multiple focal planes when using different illumination wavelengths. (A) The z-scan SHG intensity under different wavelength incident light. (B) The separation distance (Δz) between (+) and (-) focal planes under different wavelength illuminations. Dash line: the linear fitting. (C) The theoretical (dash line) and measured (dots) intensity ratio between (+) focus and (0) focal planes under different wavelength illuminations.

Based on predictions from Eq. (7.6), when the designed μ RA is inserted in the beam path with the fast axis of the central pixel is oriented at 0° , the separation distance between the (+) and (-) focal planes should be independent to the applied wavelength. However, as plotted in *Figure 7.2(B)*, the separation distance is linearly related to the applied wavelength. One possible reason is that when the μ RA is orientated at a nonzero angle γ_0 , a different phase shift is applied on the

RCP and LCP components as the offset γ_0 was added on the wavefront shaping from the μ RA, as shown in Eq. (7.7).

$$\gamma'(x, y) = \gamma_0 + \gamma(x, y) \quad (7.7)$$

As a result, an optical path difference with a global phase shift as $\pm 2\gamma_0$ is induced into the two circular polarized components, respectively, leading to a linear offset term regarding wavelength λ in the actual separation distance $\Delta z'$ as shown in Eq. (7.8).

$$\Delta z' = \frac{\gamma_0}{\pi} \cdot \lambda + \Delta z \quad (7.8)$$

Another possible reason for the linear relationship between the separation distance and applied wavelength is that the actual working distance of the objective is wavelength-dependent. A proposed experiment to confirm the two hypotheses is to repeat the measurements with μ RA rotated at different angels.

7.2.3 Polarization modulation for changing the power distribution

In order to facilitate demultiplexing of the signals from the three focal planes, an electro-optical modulator (EOM) was introduced to provide polarization modulation of the incident light. The Jones vector of the incident light with the EOM rotated an angle α is given by the following expression with a horizontally polarized fundamental.

$$\bar{e}_{in} = \begin{bmatrix} \cos \alpha & -\sin \alpha \\ \sin \alpha & \cos \alpha \end{bmatrix} \begin{bmatrix} e^{-i\frac{\Delta(\tau)}{2}} & 0 \\ 0 & e^{i\frac{\Delta(\tau)}{2}} \end{bmatrix} \begin{bmatrix} \cos \alpha & \sin \alpha \\ -\sin \alpha & \cos \alpha \end{bmatrix} \begin{bmatrix} 1 \\ 0 \end{bmatrix} \quad (7.9)$$

When the EOM is rotated at 45° , as $\alpha = \pi/4$, the incident polarization state before the designed wavefront shaping optics is described as Eq. (7.10).

$$\bar{e}_{in} = \begin{bmatrix} \cos \frac{\Delta(\tau)}{2} \\ -i \cdot \sin \frac{\Delta(\tau)}{2} \end{bmatrix} \quad (7.10)$$

As a result, the Jones vectors presenting the overall electric field for the three axially-offset focal planes are described as Eq. (7.11).

$$\begin{aligned}
\bar{e}_+ &= -i \cdot \sin \frac{\delta}{2} \cdot \frac{e^{i2\gamma}}{2} \cdot \left(\cos \frac{\Delta(\tau)}{2} + \sin \frac{\Delta(\tau)}{2} \right) \cdot \begin{bmatrix} 1 \\ i \end{bmatrix} \\
\bar{e}_0 &= \cos \frac{\delta}{2} \cdot \begin{bmatrix} \cos \frac{\Delta(\tau)}{2} \\ -i \cdot \sin \frac{\Delta(\tau)}{2} \end{bmatrix} \\
\bar{e}_- &= -i \cdot \sin \frac{\delta}{2} \cdot \frac{e^{-i2\gamma}}{2} \cdot \left(\cos \frac{\Delta(\tau)}{2} - \sin \frac{\Delta(\tau)}{2} \right) \cdot \begin{bmatrix} 1 \\ -i \end{bmatrix}
\end{aligned} \tag{7.11}$$

After the incident wavelength is determined, the retardance of the incident light relative to the design wavefront shaping optics (δ) is a constant number. In this case, two constant variables are defined as follows.

$$D_1 = -i \cdot \sin \frac{\delta}{2}; D_2 = \cos \frac{\delta}{2} \tag{7.12}$$

The detected intensity is determined as the sum of the intensity from the three components as $I_{total} = I_+ + I_0 + I_-$, in which I_+ , I_0 , and I_- are calculated by Eq. (7.13). When all light is collecting from the three focal planes, signals from the residual polarization part have a constant value, while the signals from + and – focal planes are changing oppositely. In the absence of the sample, the overall intensity at the detector will be the sum of the three components as a constant value.

$$\begin{aligned}
I_+ &= |\bar{e}_+|^2 \propto \frac{|D_1|^2}{2} \cdot [\sin \Delta(\tau) + 1] \\
I_0 &= |\bar{e}_0|^2 \propto |D_2|^2 \\
I_- &= |\bar{e}_-|^2 \propto \frac{|D_1|^2}{2} \cdot [1 - \sin \Delta(\tau)]
\end{aligned} \tag{7.13}$$

When detecting the horizontally polarized state, the signals from the three focal planes are expressed using Eq. (7.14), so that it is possible to extract information from the three focal planes based on their different response modulations

$$\begin{aligned}
I_{+H} &\propto \frac{|D_1|^2}{4} \cdot [\sin \Delta(\tau) + 1] \\
I_{0H} &\propto \frac{|D_2|^2}{2} \cdot [\cos \Delta(\tau) + 1] \\
I_{-H} &\propto \frac{|D_1|^2}{4} \cdot [1 - \sin \Delta(\tau)]
\end{aligned} \tag{7.14}$$

7.3 Discussion

The volumetric imaging instrumentation is easily achieved on a former polarization dependent second harmonic generation (SHG) microscope³ with the designed μ RA inserted just before the objective. As a result, an image set with 10 different incident polarization states is obtained. When projected along the 10 images as one, information from three focal planes is included as shown in *Figure 7.3*. According to Eq. (7.14), when detecting the horizontally polarization, there are four components with different modulation patterns, as labeled in *Figure 7.3*. One potential strategy is that blank area is selected to recover the $\Delta(\tau)$, followed with a per-pixel linear fit to assign each pixel into different focal planes. It is easy to notice that when the feature is thick enough that exist in all the three focal planes, it can only be assigned as a (0) focal plane since signals from the same feature canceled from (+) and (-) focal planes. In order word, this volumetric imaging strategy is predicted more suitable for the sparse sample. However, when the nonlinear optical process was used, such as SHG or two-photon excited fluorescence (TPEF), different intensity relationship can be addressed based on the polarization state at each focal plane and the sample.

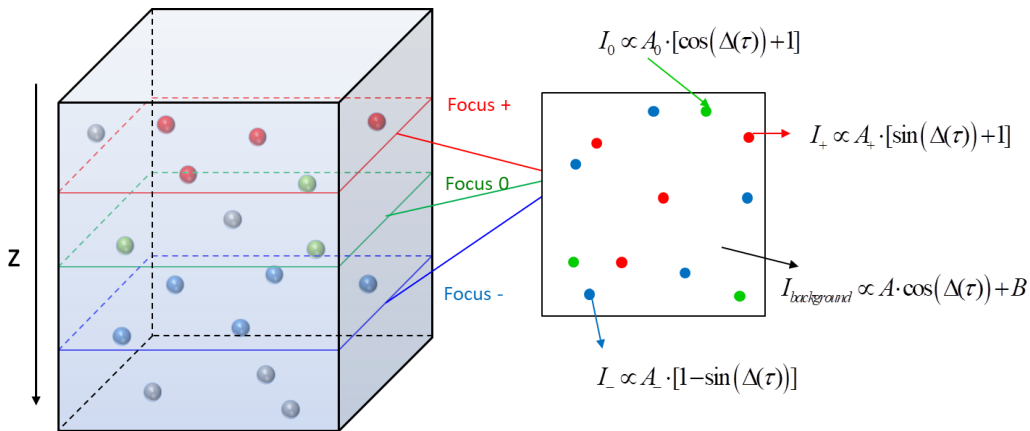


Figure 7.3 Schematic for volumetric images stacks recovered from the measured data.

7.4 Conclusion

The possibility of using polarization wavefront shaping with modulated polarization illumination to enable rapid multi-focus imaging is proven theoretically. As shown in the

preliminary results, multiple focal planes were generated at different z planes with different polarization by adding a μ RA before the objective in a microscope. The separation distance of the three focal planes is tunable mostly by varying the designed pattern of μ RA, and slightly by tuning the applied wavelength. In addition, the intensity distribution among the three focal planes is controlled by both the illumination wavelength and the polarization state. With a fast polarization modulation on the incident light, the intensity delivered to the three focal planes is simultaneously modulated with different modes. Demultiplexing of the original data has the possibility to recover a stack of three independent images from different z positions with up to 15 volumes per second for full 512×512 frame acquisitions. Based on the predictions from this Chapter, the scope of the following experiment and research will demonstrate volumetric imaging in model tissue sections or fluorophore spheres to assess the strengths and limitations of the approach relative to conventional 3D imaging methods.

7.5 References

1. Lin, Y.-H.; Wang, Y.-J.; Reshetnyak, V., Liquid crystal lenses with tunable focal length. *Liquid Crystals Reviews* **2017**, 5 (2), 111-143.
2. Suyama, S.; Date, M.; Takada, H. J. J. o. A. P., Three-dimensional display system with dual-frequency liquid-crystal varifocal lens. **2000**, 39 (2R), 480.
3. Dow, X. M. Y.; DeWalt, E. L.; Sullivan, S. Z.; Schmitt, P. D.; Simpson, G. J., Nonlinear optical Stokes ellipsometric (NOSE) microscopy for imaging the nonlinear susceptibility tensors of collagen. *Multiphoton Microscopy in the Biomedical Sciences Xvi* **2016**, 9712.

CHAPTER 8. SPATIAL/SPECTRAL MULTIPLEXING FOR VIDEO-RATE HYPERSPECTRAL IMAGING

A version of this chapter has been published by *Optics Express*. Reprint permission from Fengyuan Deng, Changqin Ding, Jerald C. Martin, Nicole M. Scarborough, Zhengtian Song, Gregory S. Eakins, Garth J. Simpson. Spatial-spectral multiplexing for hyperspectral multiphoton fluorescence imaging. *Optics Express*. 2017, 25(26), 32243-32253, copyright © 2017 Optical Society of America under the terms of the OSA Open Access Publishing Agreement.

A spatial/spectral multiplexing hyperspectral two-photon excited fluorescence (TPEF) imaging system was demonstrated. This system achieved image acquisition with up to 17 frames per second rate and over 2000 effective spectral channels in a 200 nm wavelength window. In this method, spectra from different positions in the field of view in the sample were shifted across a 16-channel photon multiplier tube (PMT) array due to the nature of beam scanning system, which enabled spatial/spectral multiplexing. The multiplexed spectral information along with the spatial information was analyzed with a novel iterative spectral retrieval and classification algorithm. The high spectral resolution of this system made it possible to distinguish fluorophores with similar emission spectra accurately comparing to conventional filter based fluorescence microscope, enabled studies of various complex samples and process. The high imaging speed of this system made it suitable for surface dynamic study or biological samples such as fluorescent *C. elegans*. This system required addition of a grating and a detector array to most commercial beam-scanning microscope, making it accessible in a wide number of research facilities as a powerful tool for hyperspectral dynamic studies.

8.1 Introduction

Fluorescence hyperspectral imaging is a powerful tool for biological studies as it provides an additional dimension of information^{1, 2} with the expansion in the spectral domain. Hyperspectral imaging enables accurate classification and quantitative analysis of multiple spectrally overlapping components in biological structures for studying complex biological processes^{3, 4} and clinical diagnoses.^{5, 6} Traditional hyperspectral imaging techniques populate the 3 dimensional data structure (x, y, λ) through spatial scanning^{7, 8} or spectral scanning.^{9, 10} Spatial

scanning interrogates the emission profile (λ) of a single pixel or line scanned across the field of view (FoV) to construct the 3D data cube. Spectral scanning methods image the entire FoV (x, y) on a 2D area detector and probe a single wavelength (λ) of emission at a time. The speed of the above acquisition is typically limited by the mechanical movement of the dispersive optics and integration time for the detector array, introducing $1/f$ noise into the measurements. However, capturing inherent dynamics of living systems such as Ca^{2+} oscillations associated with neuron firing typically requires a frame rate at around 20 Hz.^{11, 12} Furthermore, significant motion blur from cardiovascular motion degrades resolution for *in vivo* imaging.¹³ The bandwidth of current computer I/O interfaces also bottlenecks the achievable frame rate for uncompressed hyperspectral imaging. For a system with 2000 fluorescence channels, 16 bits per channel, 512×512 images at 20 frames per second (fps) speed, the overall data throughput is about 20.97 GB/s compared to the theoretical limit of a modern PCI-E 3.0 $\times 16$ interface at 15.76 GB/s. The write speed of a commercially available storage device is typically less than a few gigabytes per second, representing a practical limit on data throughput.

Recently, several snapshot hyperspectral imaging systems are developed to improve the image acquisition speed while maintaining reasonable data throughput rates.¹⁴⁻¹⁷ Coded aperture snapshot spectral imager (CASSI) directly images the projection of a rotated data cube and reconstructs the hyperspectral images using sparse sampling algorithm.¹⁶ Image mapping spectrometers (IMS) spatially offset the data cube layer by layer and projects them onto a large area detector.^{17, 18} Both of these methods provide innovative strategies to overcome the scanning mechanism and bandwidth limitation. However, most of the existing snapshot methods are not directly compatible with multi-photon excited fluorescence microscopy, which significantly increases the depth of penetration for *in vivo* imaging. Furthermore, images captured using focal plane array detectors generally introduce trade-offs between spatial and spectral resolution, as both sets of information must be encoded on the same fixed number of imaging channels.

In this chapter, an experimentally simple approach is introduced for video-rate TPEF hyperspectral imaging through non-de-scan spatial/spectral multiplexing (NDSSM) without degraded the spatial resolution. A 16-channel photomultiplier tube (PMT) array (Hamamatsu, H12311-40) was used as spatial-spectral multiplexing detector with fast single photon response time (ns), and paired with a 16-channel digital oscilloscope card (AlazarTech, ATS9416) for fast digitization. Spatial-spectral multiplexing was achieved as the projecting position of the spectra

illuminated onto the PMT array varied as a function of beam's scan position. Demultiplexing allowed recovery of spectra with over 2000 fluorescence channels at video rate (17 frames per second for frame size of 512×512 pixels). The data throughput for the 16-channel digital oscilloscope was compressed at 2.24 GB/s with the multiplexing, as opposed to 336 GB/s without compression. Since all the spectral information is contained in the orthogonal spectral axis accessed by the excitation positions in the PMT array, hyperspectral images in NDSSM are acquired without sacrificing in spatial resolution or image quality.

8.2 Methods

8.2.1 *Experimental instrumentation*

The NDSSM hyperspectral imaging system was built based on a traditional beam scan microscope as shown in *Figure 8.1*. In brief, a tunable 80 MHz Ti:Sapphire femtosecond laser (Spectra-Physics, Mai Tai) was used for excitation. For spectral calibration, the laser was tuned in a range of 800 - 1000 nm with powers at the sample around 40 - 100 mW. For TPEF hyperspectral imaging, the laser was tuned at 800 nm. The beam was scanned across the sample using a resonant scanning mirror at 8.8 kHz (EOPC) for the fast-scan axis and a galvanometer mirror (Cambridge-Tech) for the slow-scan. The beam was focused with a 10×0.3 NA objective (Nikon) as the fluorescence signal was collected in the epi direction. A dichroic mirror and a band pass filter (Chroma, 350 – 700 nm) were used to isolate the fluorescence signals. A 4f lens pair was used to direct the collimated fluorescence onto the center of a transmission diffraction grating (Wasatch Photonics, WP-600/600-25.4). The spectrally separated beam was focused on to a 16 channel PMT array (Hamamatsu, H12311-40). The 16 channel PMT array were custom built to reduce the single photon electronics response time by two orders of magnitude over the original design. The circuit for each channel consisted of a two-stage high-speed operational amplifier circuit connected directly to the output of each element on the PMT array. The output was AC-coupled into a 50Ω impedance micro-strip through a custom printed circuit board (PCB) trace in order to provide impedance matching to the output transmission line. Responses of the PMT array were digitized synchronously with the laser pulses by using a 16 channel PCI-E digital oscilloscope card and reshaped into sixteen 512×512 images via custom software (MATLAB).

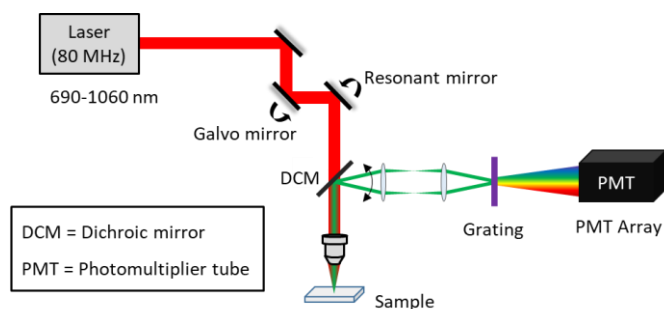


Figure 8.1 Instrument schematic of the hyperspectral imaging system.

8.2.2 Sample preparation

Fluorescein, coumarin 6, sodium dodecyl sulfate, and chloroform were purchased from Sigma-Aldrich, while eFluor™ 450 was obtained from Thermo Fisher. All aqueous solutions were prepared with Milli-Q water ($18.2 \text{ M}\Omega \text{ cm}^{-1}$). Stock solutions of $5 \mu\text{M}$ fluorescein in water and $50 \mu\text{M}$ coumarin 6 in chloroform were prepared separately. The two stock solutions were mixed equally in amount with $\sim 1\text{mg}$ of sodium dodecyl sulfate for emulsion mixture with two components. The mixture was shaken by hand to produce a stable emulsion mixture for imaging. For emulsion mixture with three components, stock solutions of fluorescein in water, coumarin 6 in chloroform, and eFluor™ 450 in chloroform were made separately with a concentration of $50 \mu\text{M}$ for each. Then two two-component emulsion mixtures were prepared separately for eFluor™ 450 / fluorescein and coumarin 6 / fluorescein system based on the procedure above, and the two two-component emulsion mixtures were mixed in equal parts to produce a three-component emulsion mixture.

As a living sample, genetically modified nematodes (*C. elegans*) strains were cultured on agar plates seeded with *Escherichia coli* at $20 \text{ }^\circ\text{C}$. For imaging, *C. elegans* strains were sealed between two glass coverslips immersed in 0.9 % NaCl physiological saline.

8.2.3 Spectral reconstruction and component classification

As the incident angle of the beam onto the diffraction grating varied during the beam scanning, each set of the 16 images from different channels was correlated spatially and spectrally for the same FoV. For each frame, pixels with the same galvanometer mirror position

shared the same spectral projection pattern on the PMT array, as shown in *Figure 8.2(A)*. Therefore, spectrum can be generated by integrating all signals from the same fluorophore along the resonant mirror axis while the galvanometer axis contained wavelength information, as shown in *Figure 8.2(B)*.

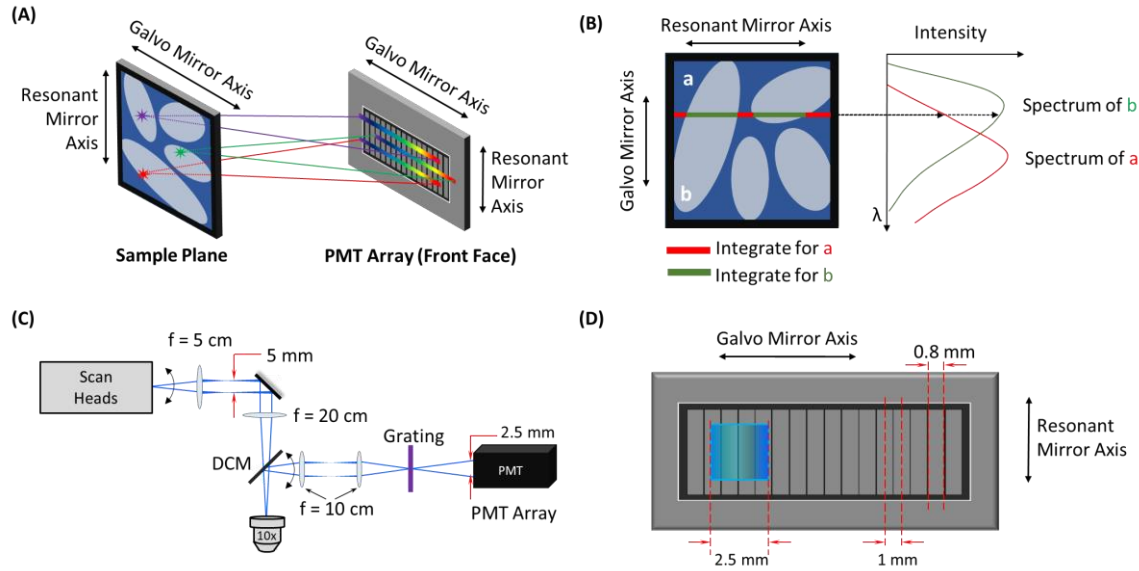


Figure 8.2 Schematic of the spatial-spectral multiplexing. (A) Illustration of spectra projected on the PMT array from different pixels in one image plane. (B) Spectral reconstruction from a single channel image for two components with different spectra. (C) Beam scanning path (not the beam path). (D) The projection of a single wavelength emission spectrum on the PMT array.

For an emission spectrum $s^0(\lambda)$ from one fluorophore (i.e., all locations of identical classification), the detected spectrum from a single PMT channel $s^{meas}(\lambda)$ can be described in Eq. (8.1), in which L is the spectral bandwidth of the PMT channel for a given galvanometer position. The measured spectral intensity $s_j^{meas}(\lambda)$ for a given measurement centered about the wavelength j is limited by L , which is equivalent to the entrance slit size of a spectrometer.

$$s_j^{meas} = \int s_j^0(\lambda) d\lambda \cong \sum_{l=-L/2}^{L/2} s_{j+l}^0 \delta\lambda \quad (8.1)$$

In Eq. (8.1), $\delta\lambda$ corresponds the bandwidth of a single pixel in the final recovered spectrum, which is generally significantly smaller than the bandwidth dictated by the physical dimensions of the PMT L , and s_j^0 corresponds to the ground truth spectrum at the position j . Extending this

analysis to each pixel in the image and the corresponding center position of the spectrum upon beam-scanning along the x -axis (galvo), the mathematical relationship described by summation in Eq. (8.1) corresponds to convolution of the ground truth spectrum with a rectangle function of width L .

$$\bar{s}^{meas} = \bar{s}^0 \otimes \text{rect}(L) \quad (8.2)$$

Significant signal to noise enhancement in the measured spectrum arises through integration of all the similarly classified locations along the orthogonal y -axis (resonant mirror). For a $\delta\lambda$ corresponding to each x -axis position in the image, a single detector can produce a spectrum with up to 512 elements for a 512×512 image. Meanwhile, the spectral overlap between channels provided references for channel sensitivity calibration and enabled spectral stitching. In the design, each single PMT channel had a width of 0.8 mm with 0.2 mm gap between channels. As the beam scan path shown in *Figure 8.3(C)*, a single wavelength emission generated a square shape at the detector array, as shown in *Figure 8.3(D)*. For a FoV of $500 \mu\text{m} \times 500 \mu\text{m}$, 512×512 pixels with a $10\times$ objective, the narrow band emission was scanned across three adjacent PMT channels with the size of $2.5 \text{ mm} \times 2.5 \text{ mm}$, inducing $\sim 2/3$ overlap between the spectral windows for each PMT channel. The significant spectral overlap illustrated in *Figure 8.3(C)* enables spectral stitching, in which minimization of the squared deviations in the overlapping regions serves to calibrate the relative sensitivity of adjacent detectors.

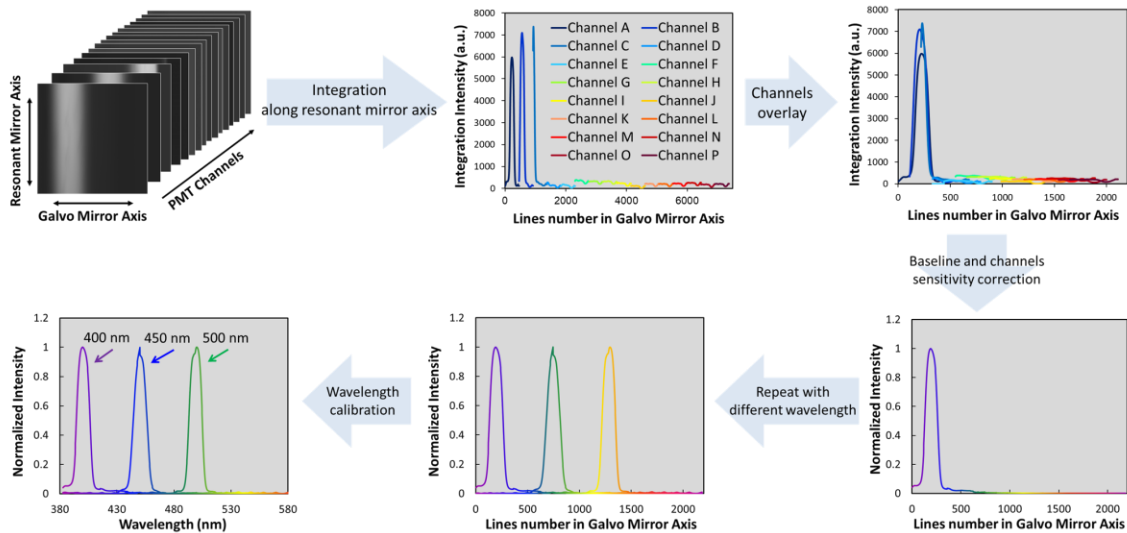


Figure 8.3 Spectral window calibration with SHG from a doubling crystal and spectrum recovery.

In reality, the second harmonic generation (SHG) from a doubling crystal was used as the narrow band emission source for spectral window calibration. As shown in *Figure 8.3*, the detected narrow band emission at a single PMT channel had a width around 170 pixels along the galvo axis. After stitching and sensitivity calibration, ~2200 independent spectral channels were recovered in the whole 200 nm spectral window.

To classify components distribution in the same FoV, an iteration algorithm was developed based on the spectrum recovery process, as shown in *Figure 8.4*. In brief, a threshold was first set to identify signal pixels from the background. The initial guess of the component spectrum was produced from the ensemble average of all pixels containing signal in the entire FoV, which served as the initial reference spectrum for a preliminary binary classification. Then Euclidean angle method as shown in Eq. (8.3) was selected for per-pixel fluorescence spectra classification¹⁹, primarily to minimize the analysis time. As in Eq. (8.3), $\bar{s}_{x,y}$ was the 16-element measured spectral vector for a single pixel at the position (x, y) , while \bar{s}_{ref} was the 16-element spectral vector extracted from the obtained initial guess (n) spectrum based on the position of the pixel as the reference.

$$\cos(\theta) = \frac{\bar{s}_{ref} \cdot \bar{s}_{x,y}}{|\bar{s}_{ref}| \cdot |\bar{s}_{x,y}|} \quad (8.3)$$

Pixels with large Euclidean angles relative to the known reference spectra (\bar{s}_{ref}) [$\cos(\theta) < 0.99$] were collectively classified as an “other” component. As a result, discrete masks for each of the second ($n+1$) components were generated. Spectra of different components were then extracted based on the new discrete classification masks. This process was iterated until 99% of the pixels in the FoV were classified as the same component with the previous iteration. Following classification, spectral recovery for each class was performed as described in the preceding paragraph, with the process iteratively performed until convergence was achieved in both the spectra recovered and the spatial classifications. For video analysis, the number of components and their spectra recovered from the first frame was used as the reference for the rest of the frames to reduce the spectral data analysis time. The computation time was dependent on the initial guess and the assumed number of components. For a two-component system, processing a single frame took about 20 to 50 seconds on a 4th generation hexa-core Intel[®] Core[™] i7 processor running in MATLAB.

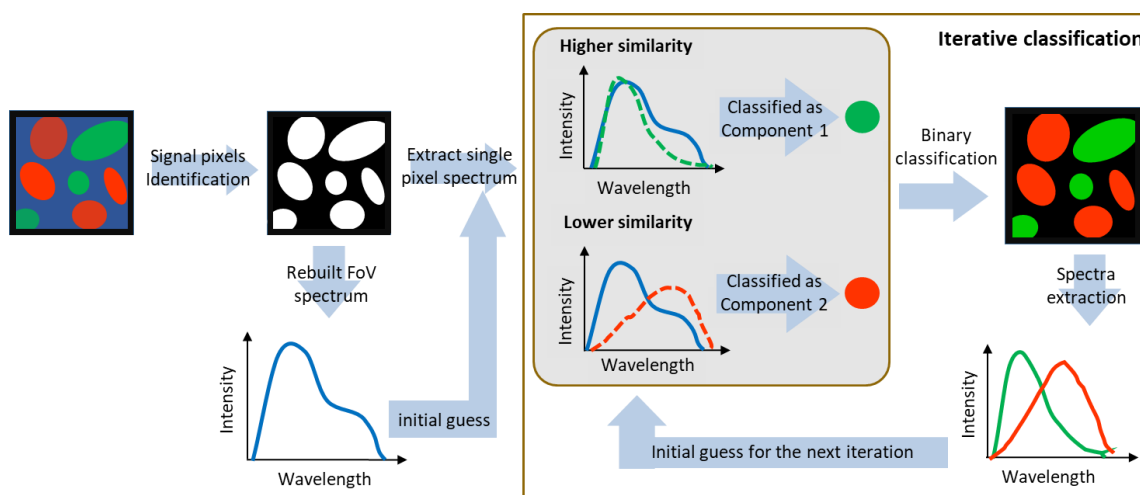


Figure 8.4 Flowchart for the iterative classification algorithm.

8.3 Results and discussion

8.3.1 *Heterogeneous mixtures of fluorescent dye droplets*

A fluorescein/coumarin 6 fluorescent dye mixture was used to assess the spectral imaging of the system and the accuracy of the classification algorithm. *Figure 8.5(A)* showed a TPEF image from the integrated intensity of all 16 channels under an 800 nm excitation. A two-component classification produced the image in *Figure 8.5(B)*, with one component labeled in green (component *a*) and another in blue (component *b*). It is worth noting that the recovered spectra of the two components were highly overlapping [*Figure 8.5(B)* insert], making them difficult to confidently discriminate using a filter-based fluorescence microscope. The recovered spectra of this hyperspectral imaging system were overlaid with independent measurements from a benchtop fluorimeter (FLS1000, Edinburgh Instruments) with a 400 nm excitation [*Figure 8.5(D) and (E)*]. All spectra were normalized to the maximum intensity. The good agreement between the recovered spectra and the fluorimeter measurements was consistent that component *a* composed primarily of fluorescein in water and component *b* primarily coumarin 6 in chloroform, which agreed with their anticipated respective solubility in water and chloroform.

While the recovered fluorescence emission spectra were in good qualitative agreement with those obtained from independent measurements with a fluorimeter, statistically significant

deviations were present for both coumarin and fluorescein. In particular, the measurements obtained in the water/chloroform suspensions exhibited broader peaks than those interrogated in pure solutions. The increase in width for the suspensions is attributed to a combination of two effects; i) convolution of the emission spectrum with a rectangle function (vide supra) results in spectral broadening, and ii) the inhomogeneity of the environment in the water/chloroform suspension results in additional inhomogeneous broadening. Given the measured response of narrow band emission, the contributions from convolution are insufficient to account for the observed differences in peak shapes. Therefore, the primary origin of the deviations observed between the emission spectra in *Figure 8.5(D)* and *(E)* are attributed to spectral broadening associated with inhomogeneity from the diversity of environments available for partitioning.

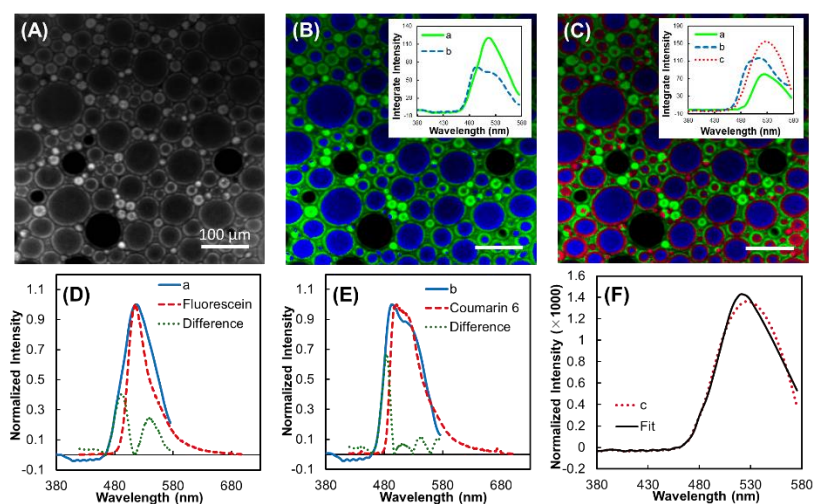


Figure 8.5 Fluorescence images and classification results of fluorescent dye droplets with the recovered spectrum. (A) Integrated total fluorescence of a dye mixture ($5\mu\text{M}$ fluorescein in water and $50\mu\text{M}$ coumarin 6 in chloroform). (B) Classification under the assumption of two components (a in green and b in blue). Insert: recovered spectra of component a and b . (C) Classification under the assumption of three components (a in green, b in blue and c in red). Insert: recovered spectra for component a , b and c . (D) Overlay of recovered spectrum of component a with the fluorescein emission spectrum from a benchtop fluorimeter, and the difference between them. (E) Overlay of recovered spectrum of component b with the coumarin 6 emission spectrum, and the difference between them. Both plotted spectra were averaged over all the spatial positions of the same classified component. (F) Spectrum of the third component (red dotted line) fitted as a linear combination (black solid line) of the first two components.

To study the distributions of fluorophores at the water-chloroform interface, classification analysis was repeated assuming a maximum number of three components. Under this case, the boundary of the chloroform droplets was identified as a third component, as marked in red in

Figure 8.5(C). The recovered spectrum for the third components (component *c*) was shown in *Figure 8.5(F)*. The spectrum of component *c* (red dot line) was fitted as a linear combination of component *a* and component *b* as shown in solid line in *Figure 8.5(F)* with $R^2 = 0.99$. Based on this fitting, component *a* (fluorescein in water) was weighted at 60.6% in the boundary between water and chloroform and component *b* (coumarin 6 in chloroform) was weighted at 39.1%. This method could provide new strategies for the study of surface interaction between different solvent.

8.3.2 Photobleaching of fluorescent dye droplets

The high speed of NDSSM enabled fluorescence photobleaching detection for TPEF with dynamic multicomponent mixtures. The three-component system was prepared by mixing eFluor™ 450 (chloroform), coumarin 6 (chloroform), and fluorescein (water). *Video 8.1* shows the dye droplets movements along with the photobleaching. *Figure 8.6(A)* and *(B)* showed two frames at different time from the video. The color of green, blue and violet indicated fluorescein, coumarin 6 and eFluor™ 450, respectively. One target droplet of coumarin 6 was circled in red to track the photobleaching behavior. Frame 55 was set as the start of the dynamic analysis (0 s), corresponding to 3.2 s in the video. After 21.8 s, the coumarin 6 fluorescence was almost lost due to photobleaching as plot in *Figure 8.6(C)*. As the result, the target droplet was misclassified as ‘eFluor™ 450’ by the classification algorithm, as circled in *Figure 8.6(B)*. The total number of excitations driving photobleaching was plotted *Figure 8.6(D)*. In brief, the single-photon peak height distribution of the PMT was measured through a histogram analysis of a time-trace. The voltages acquired during imaging were converted to absolute mean numbers of photons by using mean voltage per photon as a calibration, followed by conversion to the total number of excitations per unit time by using the previously measured quantum efficiency of coumarin 6²⁰ based on the solid angle of collection through the objective. Red line in *Figure 8.6(D)* indicated the exponential decay fit to the total number of excitation with a time constant of 5.16 ± 0.08 s, consistent with the previous observations in photobleaching.²¹

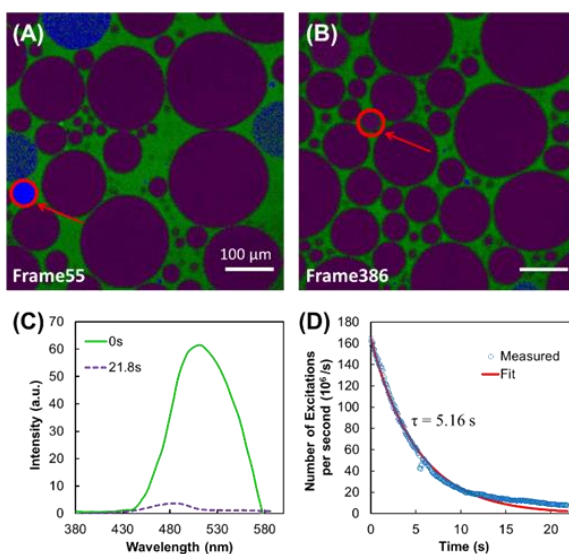


Figure 8.6 Dye mixture with three fluorophores: fluorescein (green) in water, coumarin 6 (blue) and eFluor™ 450 (violet) in chloroform separately. Target droplet with coumarin 6 in chloroform (circled in red) was tracked from its first appearance in frame 55, set as 0 s (A) and final misclassification in frame 386 with during time 21.8 s (B). (C) Spectra recovered from the target droplet at 0 s (green solid line) and 21.8 s (purple dash line). (D) Photobleaching curve of coumarin 6 in the target droplet (blue dot) with the exponential fit (red line).

8.3.3 *In vivo* imaging of genetically modified *C. elegans*

Genetically modified fluorescent nematodes (*C. elegans*) obtained from the Caenorhabditis Genetics Center were used as a living sample. The *C. elegans* variant are labeled with green and red fluorescence at the same time with different gene modifications: green fluorescence in the body wall muscle nuclei (*ccIs4251*, green fluorescence protein (GFP)), green fluorescence in the pharyngeal muscle (*mIs12*, GFP), red fluorescence in the epidermis (*frIs7*, DsRed), and red fluorescence in pharyngeal muscle (*uls69*, mCherry). Video 8.2 was acquired for the *C. elegans* with 17 frames per second, 512×512 pixels under the 800 nm excitation. A two-component classification was applied since only GFP and DsRed generate TPEF with 800 nm excitation. The two components were labeled in red and green separately as shown in Figure 8.7(A, B) with the recovered spectra shown in Figure 8.7(C). As a comparison, a single-photon excited fluorescence image was shown in Figure 8.7(D) using a conventional fluorescence microscope (Olympus BX-51) with an excitation filter at 460 - 490 nm. Similar distributions of the two structures labeled with different fluorescence colors were observed that the outside epidermis of the *C. elegans* was red and the pharyngeal muscle in the head was green. Compared to one

photon excited fluorescence image, TPEF significantly reduced the out of plane fluorescence. The recovered spectra remained consistent for the two components between the different frames, in which component 1 and component 2 were identified to be predominantly GFP and DsRed, respectively. In *Video 8.2*, an injury was observed in the mitotic region of the *C. elegans* with the increased green fluorescence signal. This phenomenon was consistent with the literature that green fluorescence due to *frIs7* mutation was preferentially enhanced by surface infection, injury, or osmotic stress.^{22, 23}

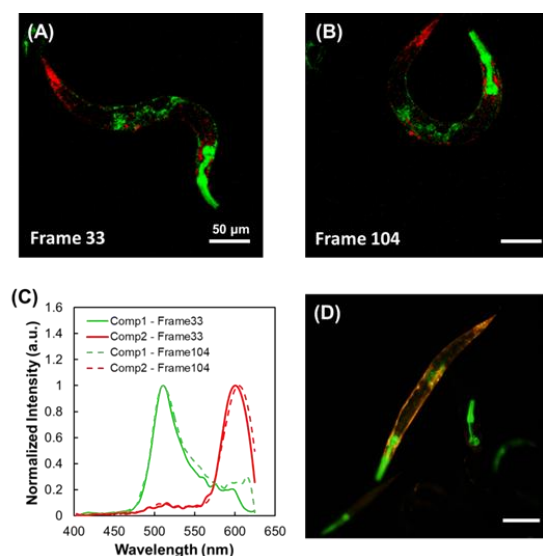


Figure 8.7 Two-photon fluorescence image of gene coded *C. elegans* analyzed without knowing the emission spectra of the fluorophores as a priori. (A) and (B) were frame 33 and 104 from *Video 8.2*. Pseudo-color based on different components recovered from custom classification algorithm with green for component 1 and red for component 2. (C) Recovered spectra for component 1 (green) and 2 (red) for both frame 33 (solid lines) and frame 104 (dash lines). Both plotted spectra were averaged over all the spatial positions of the same classified component. (D) Fluorescence image of gene coded *C. elegans* with conventional fluorescence microscope under 460 - 490 nm excitation.

8.4 Conclusion

A spatial-spectral multiplexing hyperspectral two-photon fluorescence microscope was developed with over 2000 effective spectral data points in a 200 nm wavelength window and an imaging acquisition rate up to 17 frames per second. Iterative demultiplexing enabled classification and recovery of emission spectra with no prior knowledge of the sample. The

recovered spectra showed good agreements with those obtained independently from a commercial fluorimeter. The large number of spectral data points of this system made it possible to distinguish fluorophores with highly similar emission spectra. The high imaging speed made it successful in study for highly dynamic multicomponent systems and live biological samples.

8.5 References

1. Gao, L.; Smith, R. T., Optical hyperspectral imaging in microscopy and spectroscopy - a review of data acquisition. *J Biophotonics* **2015**, *8* (6), 441-56.
2. Cutrale, F.; Trivedi, V.; Trinh, L. A.; Chiu, C. L.; Choi, J. M.; Artiga, M. S.; Fraser, S. E., Hyperspectral phasor analysis enables multi-plexed 5D in vivo imaging. *Nat Methods* **2017**, *14* (2), 149-152.
3. Lansford, R.; Bearman, G.; Fraser, S. E., Resolution of multiple green fluorescent protein color variants and dyes using two-photon microscopy and imaging spectroscopy. *J Biomed Opt* **2001**, *6* (3), 311-8.
4. Bertani, F. R.; Botti, E.; Ferrari, L.; Mussi, V.; Costanzo, A.; D'Alessandro, M.; Cilloco, F.; Selci, S., Label-free and non-invasive discrimination of HaCaT and melanoma cells in a co-culture model by hyperspectral confocal reflectance microscopy. *J Biophotonics* **2016**, *9* (6), 619-25.
5. Arrigoni, S.; Turra, G.; Signoroni, A., Hyperspectral image analysis for rapid and accurate discrimination of bacterial infections: A benchmark study. *Comput Biol Med* **2017**, *88*, 60-71.
6. Rink, C. L.; Wernke, M. M.; Powell, H. M.; Tornero, M.; Gnyawali, S. C.; Schroeder, R. M.; Kim, J. Y.; Denune, J. A.; Albury, A. W.; Gordillo, G. M.; Colvin, J. M.; Sen, C. K., Standardized Approach to Quantitatively Measure Residual Limb Skin Health in Individuals with Lower Limb Amputation. *Adv Wound Care (New Rochelle)* **2017**, *6* (7), 225-232.
7. Sinclair, M. B.; Haaland, D. M.; Timlin, J. A.; Jones, H. D., Hyperspectral confocal microscope. *Appl Opt* **2006**, *45* (24), 6283-91.
8. Luthman, A. S.; Dumitru, S.; Quiros-Gonzalez, I.; Joseph, J.; Bohndiek, S. E., Fluorescence hyperspectral imaging (fHSI) using a spectrally resolved detector array. *Journal of Biophotonics* **2017**, *10* (6-7), 840-853.
9. Morris, H. R.; Hoyt, C. C.; Treado, P. J., Imaging Spectrometers for Fluorescence and Raman Microscopy - Acoustooptic and Liquid-Crystal Tunable Filters. *Appl Spectrosc* **1994**, *48* (7), 857-866.
10. Kasili, P. M.; Vo-Dinh, T., Hyperspectral imaging system using acousto-optic tunable filter for flow cytometry applications. *Cytom Part A* **2006**, *69a* (8), 835-841.

11. Nobauer, T.; Skocek, O.; Pernia-Andrade, A. J.; Weilguny, L.; Traub, F. M.; Molodtsov, M. I.; Vaziri, A., Video rate volumetric Ca²⁺ imaging across cortex using seeded iterative demixing (SID) microscopy. *Nat Methods* **2017**, *14* (8), 811-818.
12. Prevedel, R.; Yoon, Y. G.; Hoffmann, M.; Pak, N.; Wetzstein, G.; Kato, S.; Schrodell, T.; Raskar, R.; Zimmer, M.; Boyden, E. S.; Vaziri, A., Simultaneous whole-animal 3D imaging of neuronal activity using light-field microscopy. *Nat Methods* **2014**, *11* (7), 727-730.
13. Sullivan, S. Z.; Muir, R. D.; Newman, J. A.; Carlsen, M. S.; Sreehari, S.; Doerge, C.; Begue, N. J.; Everly, R. M.; Bouman, C. A.; Simpson, G. J., High frame-rate multichannel beam-scanning microscopy based on Lissajous trajectories. *Opt Express* **2014**, *22* (20), 24224-34.
14. Dwight, J. G.; Tkaczyk, T. S., Lenslet array tunable snapshot imaging spectrometer (LATIS) for hyperspectral fluorescence microscopy. *Biomed Opt Express* **2017**, *8* (3), 1950-1964.
15. Elliott, A. D.; Gao, L.; Ustione, A.; Bedard, N.; Kester, R.; Piston, D. W.; Tkaczyk, T. S., Real-time hyperspectral fluorescence imaging of pancreatic beta-cell dynamics with the image mapping spectrometer. *J Cell Sci* **2012**, *125* (Pt 20), 4833-40.
16. Cull, C. F.; Choi, K.; Brady, D. J.; Oliver, T., Identification of fluorescent beads using a coded aperture snapshot spectral imager. *Appl Opt* **2010**, *49* (10), B59-70.
17. Gao, L.; Kester, R. T.; Hagen, N.; Tkaczyk, T. S., Snapshot Image Mapping Spectrometer (IMS) with high sampling density for hyperspectral microscopy. *Opt Express* **2010**, *18* (14), 14330-44.
18. Gao, L.; Wang, L. H. V., A review of snapshot multidimensional optical imaging: Measuring photon tags in parallel. *Phys Rep* **2016**, *616*, 1-37.
19. Garini, Y.; Gil, A.; Bar - Am, I.; Cabib, D.; Katzir, N. J. C. T. J. o. t. I. S. f. A. C., Signal to noise analysis of multiple color fluorescence imaging microscopy. **1999**, *35* (3), 214-226.
20. Reynolds, G.; Drexhage, K. H. J. O. C., New coumarin dyes with rigidized structure for flashlamp-pumped dye lasers. **1975**, *13* (3), 222-225.
21. Pujol, N.; Cypowyj, S.; Ziegler, K.; Millet, A.; Astrain, A.; Goncharov, A.; Jin, Y.; Chisholm, A. D.; Ewbank, J. J. J. C. B., Distinct innate immune responses to infection and wounding in the *C. elegans* epidermis. **2008**, *18* (7), 481-489.
22. Pujol, N.; Cypowyj, S.; Ziegler, K.; Millet, A.; Astrain, A.; Goncharov, A.; Jin, Y.; Chisholm, A. D.; Ewbank, J. J., Distinct innate immune responses to infection and wounding in the *C. elegans* epidermis. *Curr Biol* **2008**, *18* (7), 481-9.
23. Pujol, N.; Zugasti, O.; Wong, D.; Couillault, C.; Kurz, C. L.; Schulenburg, H.; Ewbank, J. J., Anti-fungal innate immunity in *C. elegans* is enhanced by evolutionary diversification of antimicrobial peptides. *PLoS Pathog* **2008**, *4* (7), e1000105.

VITA

Changqin Ding was born in Yantai, Shandong, China on February 3rd, 1990. She graduated from Tongji University, Shanghai, China, with B.S. in applied chemistry in 2012. Between her sophomore and junior year, she worked on the CO involved Plauson-Khand reactions and intramolecular cycloaddition reactions in Dr. Liyan Fan's group. In 2011, she joined Dr. Yang Tian's group and continued working as a graduate research assistant from 2012 to 2015. During this time, she accumulated experience in the method development for fluorescence biological analysis using nanoparticle or small molecular sensor. Changqin started her graduate research in Dr. Garth Simpson's group at Purdue University in 2015. Throughout her time in the lab, she has worked on the instrumentation and method development for video rate polarization-dependent optical imaging, quantitative phase contrast imaging, three-dimension imaging, and fluorescence spectral imaging.

PUBLICATIONS

1. **Changqin Ding**, Chen Li, Fengyuan Deng, Garth J. Simpson, Axially-Offset differential interference contrast microscopy via polarization wavefront shaping. *Optics Express. Optics Express.* **2019**, 27(4), 3837-3850.
2. James R. W. Ulcickas, **Changqin Ding**, Fengyuan Deng, Garth J. Simpson, Spatially encoded polarization dependent nonlinear optics. *Optics Letter.* **2018**, 43 (24), 5973-5976.
3. **Changqin Ding**, James R. W. Ulcickas, Fengyuan Deng, Garth J. Simpson. Second harmonic generation of unpolarized light. *Phys. Rev. Lett.* **2017**, 119(19), 193901.
4. Fengyuan Deng, **Changqin Ding**, Jerald C. Martin, Nicole M. Scarborough, Zhengtian Song, Gregory S. Eakins, Garth J. Simpson. Spatial-spectral multiplexing for hyperspectral multiphoton fluorescence imaging. *Optics Express.* **2017**, 25(26), 32243-32253.
5. Jingni Fu, **Changqin Ding**, Anwei Zhu, Yang Tian. A stable dual-emission core-shell fluorescent silica nanoprobe for detecting pH in living cells. *Analyst*, **2016**, 141, 4766-4771.
6. **Changqin Ding**, Yang Tian. Gold nanocluster-based fluorescence biosensor for targeted imaging in cancer cells and ratiometric determination of intracellular pH. *Biosens. Bioelectron.*, **2015**, 65, 183-190.
7. Yingying Han, **Changqin Ding**, Jie Zhou, Yang Tian. A single probe for imaging and biosensing of pH, Cu^{2+} ions, and pH/ Cu^{2+} in live cells with ratiometric fluorescence signals. *Anal. Chem.*, **2015**, 87, 5333-5339.
8. Jun Ma, **Changqin Ding**, Jie Zhou, Yang Tian. 2D ratiometric fluorescent pH sensor for tracking of cells proliferation and metabolism. *Biosens. Bioelectron.*, **2015**, 70, 202-208.
9. Fang Liu, **Changqin Ding**, Ming Jin, Yang Tian. A highly selective two-photon fluorescent probe for the determination of mercury ions. *Analyst.*, **2015**, 140, 3285-3289.
10. **Changqin Ding**, Anwei Zhu, Yang Tian. Functional surface engineering of C-dots for fluorescent biosensing and in vivo bioimaging. *Acc. Chem. Res.*, **2014**, 47(1), 20-30.
11. Xiang Gao, **Changqin Ding**, Anwei Zhu, Yang Tian. Carbon-dot-based ratiometric fluorescent probe for imaging and biosensing of superoxide anion in live cells. *Anal. Chem.* **2014**, 86(14):7071-7078.
12. Mei Zhuang, **Changqin Ding**, Anwei Zhu, Yang Tian. Ratiometric fluorescence probe for monitoring hydroxyl radical in live cells based on gold nanoclusters. *Anal. Chem.* **2014**, 86(3):1829-1836.

13. Anwei Zhu, Zongqian Luo, **Changqin Ding**, Bo Li, Shuang Zhou, Rong Wang, Yang Tian. A two-photon "turn-on" fluorescent probe based on carbon nanodots for imaging and selective biosensing of hydrogen sulfide in live cells and tissues. *Analyst*. **2014**, 139(8), 1945-1952.
14. Yan Fu, **Changqin Ding**, Anwei Zhu, Zifeng Deng, Yang Tian, Ming Jin. Two-photon ratiometric fluorescent sensor based on specific biomolecular recognition for selective and sensitive detection of copper ions in live cells. *Anal. Chem.* **2013**, 85(24), 11936-11943.
15. Anwei Zhu, **Changqin Ding**, Yang Tian. A two-photon ratiometric fluorescence probe for cupric ions in live cells and tissues. *Sci. Rep.*, **2013**, 3, DOI: 10.1038/srep02933.
16. Biao Kong, Anwei Zhu, **Changqin Ding**, Xiaoming Zhao, Bo Li, Yang Tian. Carbon dot-based inorganic-organic nanosystem for two-photon imaging and biosensing of pH variation in living cells and tissues. *Adv. Mater.*, **2012**, 24, 5844-5848.

Second Harmonic Generation of Unpolarized Light

Changqin Ding, James R. W. Ulcickas, Fengyuan Deng, and Garth J. Simpson

Department of Chemistry, Purdue University, 560 Oval Drive, West Lafayette, Indiana 47907, USA

(Received 14 August 2017; published 9 November 2017)

A Mueller tensor mathematical framework was applied for predicting and interpreting the second harmonic generation (SHG) produced with an unpolarized fundamental beam. In deep tissue imaging through SHG and multiphoton fluorescence, partial or complete depolarization of the incident light complicates polarization analysis. The proposed framework has the distinct advantage of seamlessly merging the purely polarized theory based on the Jones or Cartesian susceptibility tensors with a more general Mueller tensor framework capable of handling partial depolarized fundamental and/or SHG produced. The predictions of the model are in excellent agreement with experimental measurements of z-cut quartz and mouse tail tendon obtained with polarized and depolarized incident light. The polarization-dependent SHG produced with unpolarized fundamental allowed determination of collagen fiber orientation in agreement with orthogonal methods based on image analysis. This method has the distinct advantage of being immune to birefringence or depolarization of the fundamental beam for structural analysis of tissues.

DOI: 10.1103/PhysRevLett.119.193901

Second harmonic generation (SHG) is a second order nonlinear optical (NLO) process allowed for structures without an inversion center. The polarization dependence of SHG provides rich information on orientation and arrangement of local structures, as demonstrated for characterization of biostructures [1–4], protein crystals [5], and active pharmaceutical ingredients [5,6]. However, structural information is routinely lost in measurements designed to take advantage of the increased penetration depth of nonlinear optical interactions. In beam-scanning instruments, image contrast in SHG is generally retained in turbid media for much greater depths than analogous linear interactions [7–9]. However, the native turbidity and/or birefringence of biological media have the potential to complicate polarization dependent measurements through partial or complete depolarization of the incident and/or detected light.

Several studies have considered the effects of partial depolarization in polarization-dependent NLO imaging via the cumulative effects of scattering, birefringence, and linear or circular dichroism [3,4,10]. Optical clearing mitigates the effects of scattering by refractive index matching [11]. Careful bookkeeping of polarization-state changes has been used to remove bias in recovered tensor elements from polarization resolved SHG microscopy at tissue depths of 100 μm [3,4,10]. However, such methods do not account for the influence of depolarization arising from heterogeneity within the sample during propagation to the object plane. More recently, Mueller tensor methods have been introduced for quantitatively understanding and correcting for depolarization effects in nonlinear optical measurements. Barzda and co-workers have introduced the Stokes-Mueller framework for the theoretical description of nonlinear optical polarimetry based on a “super-Mueller

matrix” approach originally developed by Mclain and Shi [12–14]. This approach has been used to study crystalline and collagen fibril organization for polarization dependent measurements [15,16]. However, a large number of observables with many different incident polarization states are required in order to populate all 36 unique elements of the super-Mueller matrix. In a recent complementary framework [17], the Mueller tensors in partially depolarizing assemblies were greatly simplified by directly bridging Jones and Mueller tensors. The role of partial depolarization can in principle be incorporated by a single additional adjustable parameter relative to analogous measurements in nondepolarizing assemblies.

In principle, linear optical interactions can be used to describe much of the depolarization effects in nonlinear optics. In SHG microscopy of turbid media, the collective process can be conceptually broken down into three key steps: (i) propagation of the fundamental beam through the turbid matrix to the object plane, (ii) production of SHG by the object of interest by the Mueller tensor $M^{(2)}$, and (iii) propagation of the frequency-doubled light to the far-field detector. In steps (i) and (iii), partial depolarization of the incident and detected beams can, in principal, be handled by conventional linear Mueller matrices. Step (ii) cannot be described by either linear Mueller matrix transformations or considerations of conventional nonlinear polarizability based on Jones and/or Cartesian tensors.

In this Letter, the process of SHG driven by unpolarized light was considered both theoretically and experimentally, then applied to recover both polar and azimuthal orientation of collagen fibrils. In a model system, predictions from a mathematical framework connecting Jones and Mueller tensors [17] were compared with observations for z-cut

quartz. With this framework in place, polarization-dependent SHG from partial or complete depolarization of the incident beam can be quantitatively described using the intuitive Jones tensor.

In the simplest model for partial depolarization, the fundamental light reaching the object plane is considered as a linear combination of a purely depolarized fraction and a residual purely polarized component. The purely polarized fundamental surviving to the focal plane can be related to the corresponding purely polarized SHG produced locally ($\vec{e}^{-2\omega}$) by a Jones tensor formalism. The Jones vector can be connected to the more general Stokes vector with a transformation matrix A , such that $\vec{s}^{-2\omega} = A \cdot (\vec{e}^{-2\omega} \otimes \vec{e}^{-2\omega})$.

In linear optics, connecting the Mueller matrices to Jones matrices provides an intuitive framework for interpreting polarization propagation. Using the preceding relationship allows the 4×4 Mueller matrix M to be written in terms of the 2×2 Jones matrix J : $M = A \cdot (J \otimes J) \cdot A^{-1}$.

In the theoretical framework developed previously [17], these connections between Mueller and Jones matrices in linear optics were shown to be directly extendable to nonlinear optics, in which the elements of the $4 \times 4 \times 4$ Mueller tensor describing SHG $M^{(2)}$ driven by partially or fully depolarized incident light are connected back to combinations of simpler $2 \times 2 \times 2$ Jones tensor elements $\chi_J^{(2)}$ using the matrix A [Eq. (1) and Supplemental Material, Eqs. (S6)–(S9) [18]] [17,19].

$$M^{(2)} = A \cdot (\chi_J^{(2)*} \otimes \chi_J^{(2)}): A^{-1}A^{-1}. \quad (1)$$

The detected Stokes vector depends on 16 products of Jones tensor elements, which are combinations of Jones tensor elements contributing to the SHG produced with unpolarized incident light. The Stokes vector for the fraction of SHG produced from a fully depolarized beam maps onto four Mueller tensor elements: M_{000} , M_{110} , M_{200} , and M_{300} [Supplemental Material Eqs. (S1)–(S5) [18]]. As shown in Eq. (2), the nonzero Jones tensor elements can be written in four groups, with the first index in each of the χ_{ijk} tensor elements corresponding to the electric field component produced by the nonlinear optical process [Supplemental Material, Eqs. (S10–S14) [18]]. Zero indicates the laboratory horizontal axis and 1 indicates the laboratory vertical axis (Sec. II.2 of the Supplemental Material [18]).

$$\begin{bmatrix} s_0 \\ s_1 \\ s_2 \\ s_3 \end{bmatrix}^{-2\omega} = \frac{1}{4} \begin{bmatrix} 1 & 0 & 0 & 1 \\ 1 & 0 & 0 & -1 \\ 0 & 1 & 1 & 0 \\ 0 & i & -i & 0 \end{bmatrix} \cdot \begin{bmatrix} \chi_{000}^* \chi_{000} + \chi_{001}^* \chi_{001} + \chi_{010}^* \chi_{010} + \chi_{011}^* \chi_{011} \\ \chi_{000}^* \chi_{100} + \chi_{001}^* \chi_{101} + \chi_{010}^* \chi_{110} + \chi_{011}^* \chi_{111} \\ \chi_{100}^* \chi_{000} + \chi_{101}^* \chi_{001} + \chi_{110}^* \chi_{010} + \chi_{111}^* \chi_{011} \\ \chi_{100}^* \chi_{100} + \chi_{101}^* \chi_{101} + \chi_{110}^* \chi_{110} + \chi_{111}^* \chi_{111} \end{bmatrix}. \quad (2)$$

The nonzero Jones tensor elements can be further reduced by considering the symmetry within the local-frame systems. For the specific case of collagen (or any uniaxial assembly), the nonzero elements within the local frame are $\chi_{z'z'z'}$, $\chi_{z'x'x'} = \chi_{z'y'y'}$, $\chi_{x'x'z'} = \chi_{x'z'z'}$ and $\chi_{x'y'y'} = \chi_{x'z'z'} = -\chi_{y'x'z'} = -\chi_{y'z'x'}$, with the z' axis defined as the unique fiber axis. From quantum chemical calculations, the chiral terms are predicted to be relatively weak in collagen performed far from resonance, and disappear by symmetry for fibers aligned within the field of view (FOV) [4,20].

The Jones-Mueller connection enables quantitative prediction of the SHG produced from depolarized light using the knowledge of SHG originating for pure polarization states. If it is initially assumed for illustrative purposes that the local-frame z' axis of the collagen fiber axis is oriented coparallel with the laboratory Jones frame horizontal (0) axis and the x' axis is coparallel with the laboratory vertical (1) axis, the following nonzero elements remain in the laboratory-frame Jones tensor: $\chi_{000} = \chi_{z'z'z'}$, $\chi_{011} = \chi_{z'x'x'}$, and $\chi_{110} = \chi_{101} = \chi_{x'x'z'}$. For purely polarized incident light, the z' -polarized SHG is given by the coherent combination of contributions from χ_{000} and χ_{011} , the relative magnitudes and phases of which depend on the incident polarization state. Similarly, the x' -polarized component scales with the χ_{101} driven by the component of the incident light with both x' and z' polarizations.

For unpolarized incident light, the SHG can be considered as arising from the incoherent summation of these three contributions [given by the corresponding entries in the rightmost matrix in Eq. (2)]. Introduction of rotation matrices enables analysis of fibers oriented an arbitrary azimuthal angle (ϕ). Equation (2) can be rewritten as Eq. (3), which is a simplified form of Eq. (S14). The rotation operations can be applied to either the Mueller tensor as shown in Eq. (3) or to the Kronecker product of Jones tensors (detailed in Supplemental Material [18]).

$$\begin{bmatrix} s_0 \\ s_1 \\ s_2 \\ s_3 \end{bmatrix}^{-2\omega} = \frac{1}{4} \begin{bmatrix} 1 & 1 & 1 \\ \cos(2\phi) & \cos(2\phi) & -\cos(2\phi) \\ -\sin(2\phi) & -\sin(2\phi) & \sin(2\phi) \\ 0 & 0 & 0 \end{bmatrix} \begin{bmatrix} |\chi_{z'z'z'}|^2 \\ |\chi_{z'x'x'}|^2 \\ 2|\chi_{x'x'z'}|^2 \end{bmatrix}. \quad (3)$$

Consistent with previous reports [3–5,15] for z -cut quartz and collagen far from resonance, Eq. (3) can be simplified by making the approximation of $|\chi_{z'x'x'}| \cong |\chi_{x'x'z'}|$ and rewritten with two parameters: the azimuthal rotation angle ϕ and a defined ratio $\rho \equiv \chi_{z'z'z'}/\chi_{z'x'x'}$.

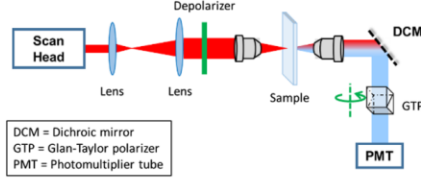


FIG. 1. SHG transmittance microscope capable of delivering both a purely polarized and a depolarized fundamental beam.

$$\begin{bmatrix} s_0 \\ s_1 \\ s_2 \\ s_3 \end{bmatrix}^{2\omega} = \frac{|\chi_{z'x'x'}^2|}{4} \begin{bmatrix} 1 & 1 & 1 \\ \cos(2\phi) & \cos(2\phi) & -\cos(2\phi) \\ -\sin(2\phi) & -\sin(2\phi) & \sin(2\phi) \\ 0 & 0 & 0 \end{bmatrix} \begin{bmatrix} |\rho|^2 \\ 1 \\ 2 \end{bmatrix}. \quad (4)$$

While Eqs. (3) and (4) are derived under the assumption that the sample is aligned within the FOV with polar tilt angle of $\pi/2$ and ρ equal to the local frame ratio given above, the same tensor elements are also present for collagen with tilt angles other than $\pi/2$ (neglecting relatively weak chiral-specific contributions). In those cases, ρ equals to the ratio of projected $\chi_{z'z'z'}$ and $\chi_{z'x'x'}$ within the FoV, defined as χ_{xxx}/χ_{yyy} (detailed in Supplemental Material [18]). To avoid confusion in the later discussion, ρ_l is defined as the local frame tensor ratio with tilt angle $\theta = \pi/2$, and ρ as the measured laboratory-frame ratio χ_{xxx}/χ_{yyy} for any arbitrary tilt angle θ .

The detected SHG intensity after a postsample polarizer at angle ϕ_{pol} can be calculated based on the Stokes vector, with s_0 normalized to unity through the proportionality constant C ,

$$I^{2\omega}(\phi_{\text{pol}}) = \frac{C}{2} [s_0 + s_1 \cos(2\phi_{\text{pol}}) - s_2 \sin(2\phi_{\text{pol}})]. \quad (5)$$

Combining Eqs. (4) and (5), the measured laboratory-frame ratio ρ can be determined by a linear fit to the measured intensities based on Eq. (6).

$$I^{2\omega}(\phi_{\text{pol}}) = \frac{C}{8} [(|\rho|^2 + 3) + (|\rho|^2 - 1) \cos(2\phi_{\text{pol}} - 2\phi)]. \quad (6)$$

To evaluate this theory, SHG measurements were performed with a custom-built microscope described in detail previously [5]. For measurements of SHG generated from a depolarized incident beam, a depolarizer (DPP-25B, Thorlabs) was placed in the collimated path (Fig. 1). A Glan-Taylor polarizer was inserted in a rotation stage in front of the detector. SHG intensity was recorded following mechanical rotation of the polarizer from 0 to π rad (ϕ_{pol})

with 60 intervals illuminated with both a purely polarized and a depolarized incident beam.

SHG produced from z -cut quartz was measured to assess the predictions for a model system with well-established nonlinear optical properties exhibiting no birefringence for light propagating parallel to the z axis. Polarized SHG produced by z -cut quartz from purely vertically polarized incident light was shown in Fig. 2. The SHG intensities integrated over the whole FOV was fit to Eq. (7) (detailed in the Supplemental Material [18] with Ref. [21]), relating to the detected polarization angle [ϕ_{pol} , Fig. 2(a)] or the quartz orientation angle [azimuthal angle ϕ , Fig. 2(b)]. Good agreement between the fitted curve (green lines) and experiment SHG intensity (blue markers) was observed, with the threefold higher periodicity in azimuthal angle in Fig. 2(b) is a consequence of the threefold rotational symmetry of z -cut quartz,

$$I^{2\omega}(\phi, \phi_{\text{pol}}) = C \sin^2(3\phi - \phi_{\text{pol}}). \quad (7)$$

For SHG produced by z -cut quartz for a depolarized incident beam, the ratio $\rho = -1$ by symmetry, such that Eq. (5) predicts the production of SHG intensity that is completely independent of both the polarizer rotation angle ϕ_{pol} and quartz orientation angle ϕ . This outcome is consistent with the production of entirely unpolarized SHG from z -cut quartz, with intensity equal to half the amplitude observed from the purely polarized source. The theoretical result is shown in purple lines in Fig. 2, together with the experimental observations (red dots) as ϕ_{pol} is varied. The predictions are in excellent agreement with the theoretical prediction. It is worth emphasizing that the theoretical trace is not a fit to the unpolarized data, but rather the predicted behavior with no adjustable parameters based on the observed trends for a polarized source. Analogous measurements performed as a function of ϕ

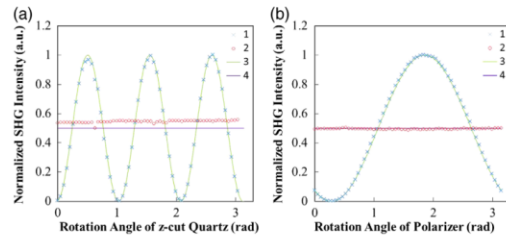


FIG. 2. (a) Polarization dependent measurement of SHG signal from z -cut quartz at an arbitrary angle under (1) vertically polarized and (2) depolarized incident light overlay with theoretical (3) fitting and (4) prediction. (b) Measurements of horizontally polarization SHG signals from z -cut quartz at different azimuthal angle under (1) vertically polarized and (2) depolarized incident light, with theoretical (3) fitting and (4) prediction.

with a fixed detector polarization rotation angle ϕ_{pol} and z-cut quartz rotation showed similar agreement between theory and experiments [Fig. 2(b)]. Although the depolarized result yields a slight offset from predictions based on the polarized measurements, the overall independence of the SHG measured through a fixed polarizer as a function of the quartz rotation angle was consistent with the expectations from the theoretical predictions. The observed offset was tentatively attributed to uncertainty in the amplitude determined from the fits of the traces observed with a purely polarized input. The excellent overall agreement between theory and experiment generally supports the validity of the mathematical framework and its approximations for describing the coherent process of SHG driven by partially or wholly depolarized light.

SHG produced from collagen within a longitudinally sectioned mouse tail was also analyzed with depolarized incident light. The local fiber orientations (ϕ) and tensor ratios (ρ) were then retrieved for every SHG-active pixel by fitting the intensity trend as a function of ϕ_{pol} described in Eq. (6). From the per-pixel fitting, the azimuthal angle of collagen was determined at a per-pixel basis for each location exhibiting sufficient signal to noise to allow statistically significant polarization analysis [Fig. 3(a)]. Unlike the case for z-cut quartz, the polarization-dependent SHG produced from a depolarized fundamental beam generally exhibited SHG with strong polarization preferences, consistent with Eq. (6) for $|\rho| \neq 1$. A representative fit is shown in Fig. 3(d).

The local azimuthal orientations of the collagen fibers were also independently determined by ORIENTATIONJ, a plugin for image directional analysis for IMAGEJ [22,23]. Figure 3(a) demonstrates the intensity-weighted orientation map retrieved via pixel-by-pixel nonlinear fit, contrasted with the orientation map recovered by ORIENTATIONJ in Fig. 3(b). Good agreement between the two methods was observed for local azimuthal orientations. Figure 3(c) shows an overlay of histogram of orientation angles recovered via both methods. Notably, ORIENTATIONJ assigns orientation based entirely on image analysis relying on context from adjacent pixels. As such, the two methods for determining azimuthal orientation (single pixel polarization analysis and contextual image analysis) are orthogonal methods yielding comparable outcomes.

Several possible explanations may account for the subtle but nonzero deviations between fiber orientation angles determined by polarization analysis versus image analysis (ORIENTATIONJ). First, the depolarizer functions by imposing a sinusoidal modulation of the polarization state across the physical expanse of the collimated beam. Upon passing this beam through the objective, the spatial Fourier transform of a sinusoidal modulation results in a horizontally offset dual-spot point spread function within the FOV, which in turn produces a double image. The SHG produced from a depolarized source should contain equal

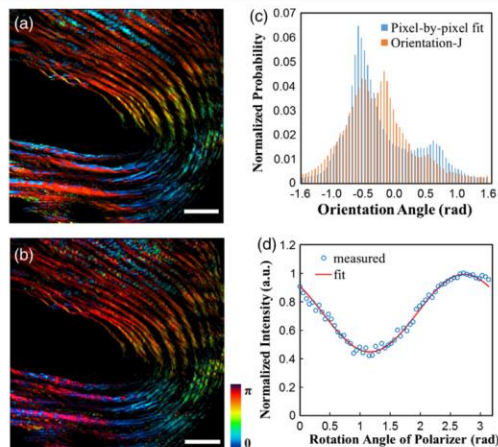


FIG. 3. Orientation images of the azimuthal angle for a single FOV of mouse tail section from (a) the pixel-by-pixel nonlinear fit analysis and (b) ORIENTATIONJ. Scale bar: 100 μm . (c) The histogram of the orientation distribution achieved from pixel-by-pixel fit and ORIENTATIONJ. (d) Nonlinear fitting results of depolarized light excitation SHG for signal random pixel.

contributions from both foci in order to be considered as genuinely depolarized. Spatial variation across the FOV may significantly influence the validity of this assumption, given that the fiber thickness is generally small relative to the displacement. Polarization analysis performed for both vertically and horizontally aligned collagen regions were compared to assess the potential impact of the double beam in polarization analysis. Given that the offset is solely along the horizontal axis, perturbations from the double focus should be significantly more pronounced for vertically oriented fibers. From inspection of the images, comparable deviations were observed for both horizontally and vertically aligned fibers, suggesting the absence of obvious systematic bias from the particular manner in which the beam was rendered unpolarized in the present study.

In addition to recovering the azimuthal angle, the polarization-dependent SHG generated from an unpolarized source also allows recovery of the measured laboratory-frame ratio ρ through Eq. (6), with representative images shown in Fig. 4(a). The modal value of $\rho = 1.69$ [Fig. 4(c)] is consistent with several other previous reports [4,24] for mouse tail and other collagenous assemblies such as chicken wing and human dermis. Deviations between polarization analysis and image analysis may arise from the implicit assumption that the fibers exhibit polar tilt angles of $\pi/2$, such that the fibers are assumed to lie flat within the FOV. In practice, any thin section is generally expected to transect a given fiber at a nonzero polar angle θ . Whereas image analysis methods such as ORIENTATIONJ can independently inform azimuthal orientation, polar tilt remains a

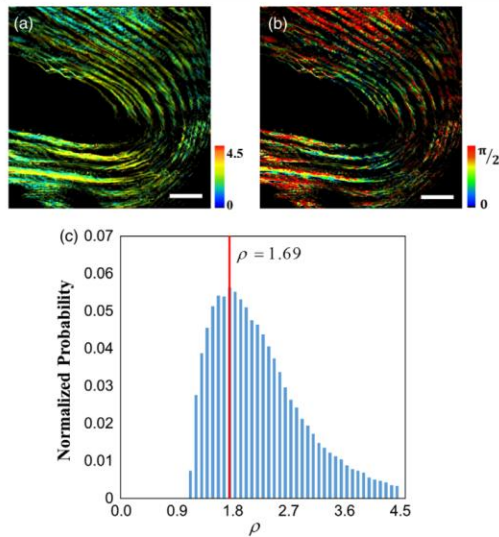


FIG. 4. (a) The measured laboratory-frame ratio ρ images for a single FOV of mouse tail section from the per-pixel fit analysis. (b) The polar tilt angle θ image recovered from the measured laboratory-frame ratio ρ for the same FOV with $\rho_l = 1.7$. (c) The distribution of the ratio ρ , with the maximum peak marked at 1.69. Scale bar: 100 μm .

challenge. Fortunately, the polarization-dependent SHG may provide a route for accessing polar tilt angle, provided the value of ρ can be independently measured or assumed.

Using literature values for the local-frame ratio ρ_l (i.e., relative to the long axis of an individual collagen fiber), a mathematical relation between measured laboratory-frame ratio (ρ), the local-frame ratio ρ_l , and the polar tilt angle (θ) was derived in Eq. (8) by projecting local tensor element onto the lab frame [25] (detailed in the Supplemental Material [18]),

$$\theta = \arcsin\left(\sqrt{\frac{\rho-3}{\rho_l-3}}\right). \quad (8)$$

A per-pixel fit was performed to recover a map of polar tilt angle θ with the assumption of a local-frame hyperpolarizability ratio $\rho_l = 1.7$ based on previously reported values in which the range of the polar tilt angle at each pixel was determined experimentally [4,15]. This value of the local-frame ratio for collagen fibers is quite similar to the most probable ratio observed experimentally [Fig. 4(c)], consistent with an assembly in which the most probable collagen orientation is lying flat within the field of view. With the assumption of $\rho_l = 1.7$, the observed values of ρ were used to recover the polar tilt angle at each pixel through Eq. (8). The recovered map of polar tilt angle θ was

shown in Fig. 4(b). A significant portion of collagen fibers was tilted out of the detection plane (i.e., $\theta \neq \pi/2$). This phenomenon was more obvious in the region where collagen fibers bend. The measurements likely contain an implicit bias against tilt angles of $\theta \cong 0$, as fibers aligned parallel with the optical access are symmetry forbidden for production of coherent SHG. The results shown in Fig. 4 are largely insensitive to the particular assumed value of ρ_l , yielding qualitatively similar results when assuming $\rho_l = 1.4$ (consistent with other reports for the local-frame tensor element ratio) [4,15].

In summary, the results of this study have intriguing implications on polarization analysis of depolarizing systems. A Mueller tensor framework was utilized to predict the polarization of SHG stimulated with depolarized light. This framework has been verified experimentally with z -cut quartz and collagenous tissue under depolarized incident light. From a practical standpoint, the intentional use of depolarized incident light has the distinct advantage of providing measurements that are immune to subsequent depolarization of the fundamental beam. Despite the loss of information from scrambling of the incident polarization, analysis of collagenous tissue with depolarized SHG still allowed determination of both collagen azimuthal and polar orientation from the laboratory-frame tensor elements. The use of unpolarized incident light may significantly simplify polarization analysis in thick tissue sections for measurement in transmission.

The authors gratefully acknowledge support from the NIH Grants No. R01GM-103401, and No. R01GM-103910 from the NIGMS.

- [1] P. J. Campagnola and L. M. Loew, *Nat. Biotechnol.* **21**, 1356 (2003).
- [2] P. Stoller, K. M. Reiser, P. M. Celliers, and A. M. Rubenchik, *Biophys. J.* **82**, 3330 (2002).
- [3] I. Gusachenko, V. Tran, Y. Goulam Houssen, J. M. Allain, and M. C. Schanne-Klein, *Biophys. J.* **102**, 2220 (2012).
- [4] X. Y. Dow, E. L. DeWalt, S. Z. Sullivan, P. D. Schmitt, J. R. Ulcickas, and G. J. Simpson, *Biophys. J.* **111**, 1361 (2016).
- [5] E. L. DeWalt, S. Z. Sullivan, P. D. Schmitt, R. D. Muir, and G. J. Simpson, *Anal. Chem.* **86**, 8448 (2014).
- [6] P. D. Schmitt, E. L. DeWalt, X. Y. Dow, and G. J. Simpson, *Anal. Chem.* **88**, 5760 (2016).
- [7] T. Petralli-Mallow, T. M. Wong, J. D. Byers, and H. I. Yee, *J. Phys. Chem.* **97**, 1383 (1993).
- [8] F. Tiaho, G. Recher, and D. Rouede, *Opt. Express* **15**, 12286 (2007).
- [9] I. Amat-Roldan, S. Psilodimitrakopoulos, P. Loza-Alvarez, and D. Artigas, *Opt. Express* **18**, 17209 (2010).
- [10] I. Gusachenko, G. Latour, and M. C. Schanne-Klein, *Opt. Express* **18**, 19339 (2010).
- [11] O. Nadiarnykh and P. J. Campagnola, *Opt. Express* **17**, 5794 (2009).

- [12] M. Samim, S. Krouglov, and V. Barzda, *Phys. Rev. A* **93**, 013847 (2016).
- [13] Y. M. Shi, W. M. McClain, and R. A. Harris, *Chem. Phys. Lett.* **205**, 91 (1993).
- [14] Y. M. Shi, W. M. McClain, and R. A. Harris, *Phys. Rev. A* **49**, 1999 (1994).
- [15] M. Burke, A. Golaraei, A. Atkins, M. Akens, V. Barzda, and C. Whyne, *J. Struct. Biol.* **199**, 153 (2017).
- [16] R. Cisek, D. Tokarz, M. Steup, I. J. Tetlow, M. J. Emes, K. H. Hebelstrup, A. Blennow, and V. Barzda, *Biomed. Opt. Express* **6**, 3694 (2015).
- [17] G. J. Simpson, *J. Phys. Chem. B* **120**, 3281 (2016).
- [18] See Supplemental Material at <http://link.aps.org/supplemental/10.1103/PhysRevLett.119.193901> for detailed mathematical derivation.
- [19] R. M. A. Azzam and N. M. Bashara, *Ellipsometry and Polarized Light* (Elsevier, Amsterdam, 1987).
- [20] M. de Wergifosse, J. de Ruyck, and B. Champagne, *J. Phys. Chem. C* **118**, 8595 (2014).
- [21] X. Y. Dow, E. L. DeWalt, J. A. Newman, C. M. Dettmar, and G. J. Simpson, *Biophys. J.* **111**, 1553 (2016).
- [22] C. A. Schneider, W. S. Rasband, and K. W. Eliceiri, *Nat. Methods* **9**, 671 (2012).
- [23] Z. Puspoki, M. Storath, D. Sage, and M. Unser, *Adv Anat. Embryol Cell Biol* **219**, 69 (2016).
- [24] W. Chen, T. Li, P. Su, C. Chou, P. T. Fwu, S. Lin, D. Kim, P. T. C. So, and C. Dong, *Appl. Phys. Lett.* **94**, 183902 (2009).
- [25] A. J. Moad and G. J. Simpson, *J. Phys. Chem. B* **108**, 3548 (2004).

Supplemental Material

Second Harmonic Generation of Unpolarized Light

Changqin Ding, James R. W. Ulcickas, Fengyuan Deng, Garth J. Simpson

Department of Chemistry, Purdue University, 560 Oval Drive, West Lafayette, IN, 47907, United States

1. Experimental Methods

Polarization-dependent SHG measurements were performed on z-cut quartz (500 μm thickness) using a 10 \times , 0.3 NA objective for theoretical validation. Measurements of polarization-dependent SHG from collagen were performed using a 20 \times , 0.4 NA Nikon objective with mouse tails gifted from Prof. Philip Low (Purdue University, West Lafayette, IN). Mouse tails were first decalcified in the solution of 23% formic acid, 4% formalin, and 1% methanol for 2 hours, then sectioned longitudinally to ensure that sections were retrieved from the central region of the tail. For the SHG imaging, the mouse tail section was then fixed in 10% formalin and embedded in paraffin prior to microtoming into 4 μm thick slides.

SHG measurements were performed with a custom-built microscope.[1] Briefly, an 80 MHz 100 fs Mai Tai Ti:sapphire laser (SpectraPhysics) at 800 nm was used as incident light source. The beam was scanned across the sample using a resonant scanning mirror at 8.8 kHz (EOPC) for the fast-scan axis synchronized to the laser, and a galvanometer mirror (CambridgeTech) for the slow-scan. Then the beam was expanded through a pair of lens and focused with various objectives (10 \times , 0.3 NA; and 20 \times , 0.4 NA; Nikon) with average power between 40 - 80 mW on the sample. For depolarized incident light, a depolarizer (DPP-25B, Thorlabs) was placed in the collimated path after the beam expansion and before the excitation objective (*Scheme 1*). SHG from the sample was collected through a 10 \times , 0.3 NA OPTEM condenser and separated from the fundamental light using a dichroic mirror in the transmitted direction. A Glan-Taylor polarizer was placed in a rotation stage before a photomultiplier tubes (PMT, Hamamatsu H12310-40) with bandpass filters (HQ 400/20m-2p; Chroma Technology) for the SHG detection. Polarization dependent SHG

measurements were conducted via mechanical rotation of the polarizer from 0 to 180 degrees with 3 degree intervals.

1. Theoretical foundation.

1.1. Stokes Vector and Jones Tensor for detected SHG.

In the most general manner, the rank three Mueller tensor $M^{(2)}$ describing SHG in the presence of partial depolarization can be written in the following form.

$$\bar{s}_{det}^{2\omega} = \mathbf{M}_{det}^{(2)} : \bar{s}^\omega \bar{s}^\omega \quad (S1)$$

In Eq.(S1), the Stokes vector describing the detected SHG is given by the tensor product of the Mueller tensor and the incident Stokes vector \bar{s}^ω . The tensor product can be rewritten using a vectorized form of the Mueller tensor, as described in previous work.[2] It can be rewritten as Eq.(S2), in which I_4 is a 4×4 identity matrix and \bar{M} is the 64-element ascending vectorized form of the Mueller tensor, and the symbol \otimes indicates a Kronecker product.

$$\bar{s}_{det}^{2\omega} = \left[I_4 \otimes (\bar{s}^\omega)^T \otimes (\bar{s}^\omega)^T \right] \cdot \bar{M}_{det} \quad (S2)$$

In SHG microscopy of a turbid sample, partial depolarization of the incident and detected beams can be in principal handled by conventional linear Mueller matrices.

$$\bar{s}_{det}^{2\omega} = M^{2\omega} \cdot \bar{s}_{obj}^{2\omega} = M^{2\omega} \cdot \mathbf{M}_{obj}^{(2)} : (M^\omega \cdot \bar{s}^\omega) (M^\omega \cdot \bar{s}^\omega) \quad (S3)$$

The two sets of linear Mueller matrices can be combined with the underlying Mueller tensor of the object $\mathbf{M}_{obj}^{(2)}$ to describe the net observed Mueller tensor.

$$\mathbf{M}_{det}^{(2)} = (M^{2\omega} \cdot \mathbf{M}_{obj}^{(2)} : M^\omega M^\omega) \quad (S4)$$

In the simplest model for partial depolarization, we consider the fundamental light reaching the object plane as a simple linear combination of a fully depolarized fraction (α) and a residual purely polarized component ($1-\alpha$). For depolarized component of the incident light, s_0 is the only nonzero entry in the Stokes vector for the fundamental. Upon making this substitution, only a subset of 4 elements within the Mueller tensor contribute to the Stokes vector produced from a depolarized source: M_{000} , M_{100} , M_{200} , and M_{300} (respectively

corresponding to the decimal positions of 0, 16, 32, and 48 in the vectorized tensor). In this case, the Stokes vector for the SHG maps directly onto those four Mueller tensor elements.

$$\begin{bmatrix} S_0 \\ S_1 \\ S_2 \\ S_3 \end{bmatrix}_{obj}^{2\omega} = \alpha \cdot \bar{s}_{depol}^{2\omega} + (1-\alpha) \cdot \bar{s}_{pol}^{2\omega} = \alpha \cdot \begin{bmatrix} M_{000} \\ M_{100} \\ M_{200} \\ M_{300} \end{bmatrix}_{depol} + (1-\alpha) \cdot \mathbf{M}_{pol}^{(2)} : \bar{s}_{in}^\omega \bar{s}_{in}^\omega \quad (S5)$$

The purely polarized component scaled by $(1-\alpha)$ can be handled in the conventional way by switching to a Jones tensor description for SHG with purely polarized inputs, such that $\bar{e}_{obj}^{-2\omega} = \chi_{obj}^{(2)} : \bar{e}_{obj}^{-\omega} \bar{e}_{obj}^{-\omega}$ and $\bar{s}_{pol}^{2\omega} = A \cdot \left(\bar{e}_{obj}^{-2\omega} \otimes \bar{e}_{obj}^{-2\omega} \right)$. As such, the first term is arguably more interesting to consider in greater detail. In brief, it describes the Stokes vector produced by the fully depolarized component of the fundamental beam at the object plane, which raises conceptual and mathematical questions regarding prediction of the anticipated output.

The elements of the Mueller tensor describing SHG driven by partially or fully depolarized incident light were connected back to combinations of simpler Jones tensor elements. The expression bridging the two formalisms was derived in earlier work.[2]

$$M^{(2)} = A \cdot \left(\chi_J^{(2)*} \otimes \chi_J^{(2)} \right) : A^{-1} A^{-1} \quad (S6)$$

The matrix A is the well-established transformation matrix connecting the Jones and Stokes vectors for purely polarized light.[2,3]

$$\bar{s} = \begin{bmatrix} 1 & 0 & 0 & 1 \\ 1 & 0 & 0 & -1 \\ 0 & 1 & 1 & 0 \\ 0 & i & -i & 0 \end{bmatrix} \cdot \begin{pmatrix} \bar{e}_0^* \bar{e}_0 \\ \bar{e}_0^* \bar{e}_1 \\ \bar{e}_1^* \bar{e}_0 \\ \bar{e}_1^* \bar{e}_1 \end{pmatrix} = A \cdot \left(\bar{e}^* \otimes \bar{e} \right) \quad (S7)$$

Eq.(S6) can be rewritten in vectorized form.

$$\bar{M} = \left[A \otimes (A^{-1})^T \otimes (A^{-1})^T \right] \cdot \overline{\left(\chi_J^{(2)*} \otimes \chi_J^{(2)} \right)} \quad (S8)$$

The corresponding Stokes vector describing the SHG is given by substitution into Eq. (S7).

$$\bar{s}^{2\omega} = \left[I_4 \otimes (\bar{s}^\omega)^T \otimes (\bar{s}^\omega)^T \right] \cdot \left[A \otimes (A^{-1})^T \otimes (A^{-1})^T \right] \cdot \overline{\left(\chi_J^{(2)*} \otimes \chi_J^{(2)} \right)} \quad (S9)$$

This form now allows identification of the nonzero combinations of Jones tensor elements contributing to the SHG produced with unpolarized incident light.

1.2. Connecting the Stokes Vector and Jones Tensor for Depolarized Light.

Taking advantage of the identity relationship $(A \otimes B) \cdot (C \otimes D) = (A \cdot B) \otimes (C \cdot D)$ allows Eq. (S9) to be rewritten in the following form.

$$\bar{s}^{2\omega} = (I_4 \cdot A) \otimes \left[(\bar{s}^\omega)^T \otimes (\bar{s}^\omega)^T \cdot (A^{-1})^T \otimes (A^{-1})^T \right] \cdot \overline{(\chi_J^{(2)*} \otimes \chi_J^{(2)})} \quad (\text{S10})$$

Since any matrix commutes with the identity matrix, Eq. (S10) can be rewritten inverting the order of I_4 and A . Regrouping with the associative properties of Kronecker products allows rearrangement to the following form.

$$\bar{s}^{2\omega} = A \cdot \left\{ (I_4) \otimes \left[(\bar{s}^\omega)^T \otimes (\bar{s}^\omega)^T \cdot (A^{-1})^T \otimes (A^{-1})^T \right] \right\} \cdot \overline{(\chi_J^{(2)*} \otimes \chi_J^{(2)})} \quad (\text{S11})$$

The transpose operation can be more conveniently evaluated over the entire set of terms within brackets, using the equality $B^T \cdot C^T = (C \cdot B)^T$.

$$\bar{s}^{2\omega} = A \cdot \left\{ I_4 \otimes (A^{-1} \otimes A^{-1}) \cdot (\bar{s}^\omega \otimes \bar{s}^\omega) \right\}^T \cdot \overline{(\chi_J^{(2)*} \otimes \chi_J^{(2)})} \quad (\text{S12})$$

Again, using the identity $(A \otimes B) \cdot (C \otimes D) = (A \cdot B) \otimes (C \cdot D)$ allows regrouping.

$$\bar{s}^{2\omega} = A \cdot \left\{ I_4 \otimes (A^{-1} \cdot \bar{s}^\omega) \otimes (A^{-1} \cdot \bar{s}^\omega) \right\}^T \cdot \overline{(\chi_J^{(2)*} \otimes \chi_J^{(2)})} \quad (\text{S13})$$

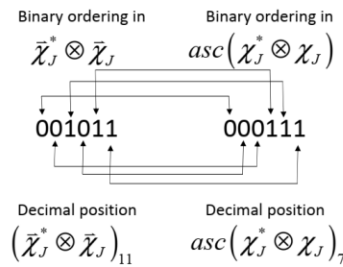
The 4-element vector $A^{-1} \cdot \bar{s}^\omega$ contains only two nonzero entries for depolarized light.

$$A^{-1} \cdot \bar{s}^\omega = \frac{1}{2} \begin{bmatrix} 1 \\ 0 \\ 0 \\ 1 \end{bmatrix} \quad (\text{S14})$$

The Kronecker product of $(A^{-1} \cdot \bar{s}^\omega) \otimes (A^{-1} \cdot \bar{s}^\omega)$ produces a 16-element vector with the following nonzero entries: 0, 3, 12, 15, which in binary correspond to 000000, 000011, 001100, 001111, respectively. Following an additional Kronecker product by the identity matrix, this same set of four entries exclusively contributes to $s_0^{2\omega}$, the set 010000, 010011,

011100, and 011111 (corresponding to indices 16, 19, 28, and 31, respectively) contribute exclusively to $s_1^{2\omega}$, etc.

In addition to clarifying the underlying patterns, expressing the entries in binary notation has some practical advantages. Most notably, only a small subset of the entries within the product $\overline{(\chi_J^{(2)*} \otimes \chi_J^{(2)})}$ contributes to the measured Stokes vector, with binary notation aiding in their identification. As described in previous work[3], the specific combinations of tensor elements within the vector $\overline{(\chi_J^{(2)*} \otimes \chi_J^{(2)})}$ can be generated by re-ordering of the 0 and 1 entries in the binary number.



Using the first four entries to illustrate this process, the binary number 000000 corresponds to the combination of Jones tensor element $\chi_{000}^* \chi_{000}$, the number 000011 corresponds to $\chi_{001}^* \chi_{001}$, the number 001100 corresponds to $\chi_{010}^* \chi_{010}$, and the number 001111 corresponds to $\chi_{011}^* \chi_{011}$. Since only these four elements contribute to $s_0^{2\omega}$, explicit evaluation of the term in curly brackets in Eq. (S13) multiplied by the vectorized tensor element products yields the first row of the right-most vector in Eq. (2). An analogous set of operations allows population of the remaining three rows in that same right-most vector in Eq. (2).

1.3. Connecting Local and Laboratory Frames.

Symmetry within the local-frame system can significantly reduce the number of nonzero Jones tensor elements. In the case of collagen aligned along the horizontal laboratory-frame axis, the nonzero elements within the collagen frame are $\chi_{z'z'z'}$, $\chi_{z'x'x'}$, $\chi_{x'x'z'} = \chi_{x'z'x'}$, and $\chi_{x'y'z'} = \chi_{x'z'y'} = -\chi_{y'x'z'} = -\chi_{y'z'x'}$. In most practical instances, the chiral terms can be neglected, since they are predicted to be relatively weak in collagen and disappear by symmetry for fibers

aligned within the field of view. If the local-frame z' -axis is coparallel with the laboratory-frame horizontal (0) axis and the x' -axis is coparallel with the laboratory vertical (1) axis, inspection of Eq. (2) indicates that only the following four tensor element products will contribute to the detected Stokes vector for the SHG: $|\chi_{000}|^2$, $|\chi_{011}|^2$, $|\chi_{101}|^2$, and $|\chi_{110}|^2$. For the z' -axis oriented coparallel with the laboratory horizontal axis in the laboratory Jones frame, the only two of the four nonzero elements in the Jones tensor describing collagen remained as: $\chi_{000} = \chi_{z'z'z'}$, $\chi_{011} = \chi_{z'x'x'}$, and $\chi_{110} = \chi_{101} = \chi_{x'x'z'}$. Substitution into Eq. (2) yields the following expression for the Stokes vector produced for an unpolarized input beam.

$$\begin{bmatrix} S_0 \\ S_1 \\ S_2 \\ S_3 \end{bmatrix}^{2\omega} = \frac{1}{4} \begin{bmatrix} |\chi_{z'z'z'}|^2 + |\chi_{z'x'x'}|^2 + 2|\chi_{x'x'z'}|^2 \\ |\chi_{z'z'z'}|^2 + |\chi_{z'x'x'}|^2 - 2|\chi_{x'x'z'}|^2 \\ 0 \\ 0 \end{bmatrix}_{\phi=0} \quad (S15)$$

The subscript $\phi = 0$ in Eq. (S15) indicates a collagen fiber axis coparallel with the horizontal laboratory-frame axis, corresponding to an azimuthal rotation angle ϕ of zero (i.e., in which the local frame and laboratory frame have a specific correspondence). This expression can be generalized to include arbitrary azimuthal rotation by introduction of rotation matrices.

In general, the collagen principal axis will not be oriented exclusively along either the vertical or horizontal axes. Two equivalent strategies can be taken: i) generate the Mueller tensor for a uniaxial assembly in the local frame, then project onto the laboratory frame coordinates, or ii) generate the Jones tensor for a uniaxial assembly, then project onto the laboratory frame. The equivalence of these two approaches can be demonstrated as follows. The vectorized form for the laboratory frame Mueller tensor is connected to the vectorized local-frame Mueller tensor by a rotation operation.[2]

$$\bar{M}_L = (\mathcal{R}_\phi \otimes \mathcal{R}_\phi \otimes \mathcal{R}_\phi) \cdot \bar{M}_l' \quad (S16)$$

The prime on the local-frame Mueller tensor indicates that all 64 elements are included in the vectorized form, many of which will be zero-valued by the assumption of local uniaxial symmetry. The rotation matrix \mathcal{R}_ϕ is given by Eq.(S17), where R_ϕ is the rotation matrix for a Jones vector described in Eq.(S18).

$$\mathcal{R}_\phi = A \cdot (R_\phi \otimes R_\phi) \cdot A^{-1} \quad (S17)$$

$$R_\phi = \begin{bmatrix} \cos \phi & \sin \phi \\ -\sin \phi & \cos \phi \end{bmatrix} \quad (\text{S18})$$

Substitution of the rotated tensor expression in Eq. (S16) into Eq. (S2) yields the following expression for the Stokes vector describing SHG.

$$\bar{s}^{2\omega} = \left[I_4 \otimes (\bar{s}^\omega)^T \otimes (\bar{s}^\omega)^T \right] \cdot (\mathcal{R}_\phi \otimes \mathcal{R}_\phi \otimes \mathcal{R}_\phi) \cdot \bar{M}_l' \quad (\text{S19})$$

The Stokes vector can be connected back to the elements of the Jones vector by substitution of the relation in Eq. (S8) using the complete set of local-frame tensor elements.

$$\bar{s}^{2\omega} = \frac{1}{4} \left[I_4 \otimes (\bar{s}^\omega)^T \otimes (\bar{s}^\omega)^T \right] \cdot (\mathcal{R}_\phi \otimes \mathcal{R}_\phi \otimes \mathcal{R}_\phi) \cdot \left[A \otimes (A^{-1})^T \otimes (A^{-1})^T \right] \cdot \overline{(\chi_l^{(2)*} \otimes \chi_l^{(2)})} \quad (\text{S20})$$

Rearrangement of the middle terms can be done as follows.

$$(\mathcal{R}_\phi \otimes \mathcal{R}_\phi \otimes \mathcal{R}_\phi) \cdot \left[A \otimes (A^{-1})^T \otimes (A^{-1})^T \right] = \left[(\mathcal{R}_\phi \cdot A) \otimes (\mathcal{R}_\phi \cdot (A^{-1})^T) \otimes (\mathcal{R}_\phi \cdot (A^{-1})^T) \right] \quad (\text{S21})$$

Connecting the Mueller and Jones rotation matrices allows the following substitution.

$$\mathcal{R}_\phi A = \left[A \cdot (R_\phi \otimes R_\phi) \cdot A^{-1} \right] A = A \cdot (R_\phi \otimes R_\phi) \quad (\text{S22})$$

Substitution into Eq. (S9) yields the following simplification.

$$\begin{aligned} & (\mathcal{R}_\phi \otimes \mathcal{R}_\phi \otimes \mathcal{R}_\phi) \cdot \left[A \otimes (A^{-1})^T \otimes (A^{-1})^T \right] \\ &= \left[A \otimes (A^{-1})^T \otimes (A^{-1})^T \right] \cdot \left[R_\phi \otimes R_\phi \otimes R_\phi \otimes R_\phi \otimes R_\phi \right] \end{aligned} \quad (\text{S23})$$

The Stokes vector is given by an expression similar to the one in Eq.(S9), but with a rotated reference frame for the local-frame Jones tensors.

$$\begin{aligned} \bar{s}^{2\omega} &= \frac{1}{4} \left[I_4 \otimes (\bar{s}^\omega)^T \otimes (\bar{s}^\omega)^T \right] \cdot \left[A \otimes (A^{-1})^T \otimes (A^{-1})^T \right] \\ &\quad \cdot \left[R_\phi \otimes R_\phi \otimes R_\phi \otimes R_\phi \otimes R_\phi \right] \cdot \overline{(\chi_l^{(2)*} \otimes \chi_l^{(2)})} \end{aligned} \quad (\text{S24})$$

For an achiral assembly with local uniaxial symmetry, only four nonzero tensor elements remain for SHG; $\chi_{z'z'z'}$, $\chi_{z'x'x'}$, $\chi_{x'z'x'}$, and $\chi_{x'x'z'}$. These collectively produce 16 nonzero combinations in the Kronecker product in Eq.(S24), which map to the laboratory frame tensor elements in Eq. (2).

$$\begin{aligned}
& \begin{bmatrix} \chi_{000}^* \chi_{000} + \chi_{001}^* \chi_{001} + \chi_{010}^* \chi_{010} + \chi_{011}^* \chi_{011} \\ \chi_{000}^* \chi_{100} + \chi_{001}^* \chi_{101} + \chi_{010}^* \chi_{110} + \chi_{011}^* \chi_{111} \\ \chi_{100}^* \chi_{000} + \chi_{101}^* \chi_{001} + \chi_{110}^* \chi_{010} + \chi_{111}^* \chi_{011} \\ \chi_{100}^* \chi_{100} + \chi_{101}^* \chi_{101} + \chi_{110}^* \chi_{110} + \chi_{111}^* \chi_{111} \end{bmatrix} \\
& = \begin{bmatrix} \cos^2 \phi & \cos^2 \phi & \sin^2 \phi & \sin^2 \phi \\ \sin \phi \cos \phi & \sin \phi \cos \phi & -\sin \phi \cos \phi & -\sin \phi \cos \phi \\ \sin \phi \cos \phi & \sin \phi \cos \phi & -\sin \phi \cos \phi & -\sin \phi \cos \phi \\ \sin^2 \phi & \sin^2 \phi & \cos^2 \phi & \cos^2 \phi \end{bmatrix} \cdot \begin{bmatrix} |\chi_{z'z'z'}|^2 \\ |\chi_{z'x'x'}|^2 \\ |\chi_{x'z'x'}|^2 \\ |\chi_{x'x'z'}|^2 \end{bmatrix} \quad (S25)
\end{aligned}$$

Substitution of this equality into Eq. (2) and evaluation of the multiplication by A yields the following:

$$\begin{bmatrix} s_0 \\ s_1 \\ s_2 \\ s_3 \end{bmatrix}^{2\omega} = \frac{1}{4} \begin{bmatrix} 1 & 1 & 1 & 1 \\ \cos^2 \phi - \sin^2 \phi & \cos^2 \phi - \sin^2 \phi & \sin^2 \phi - \cos^2 \phi & \sin^2 \phi - \cos^2 \phi \\ 2 \sin \phi \cos \phi & 2 \sin \phi \cos \phi & 2 \sin \phi \cos \phi & 2 \sin \phi \cos \phi \\ 0 & 0 & 0 & 0 \end{bmatrix} \cdot \begin{bmatrix} |\chi_{z'z'z'}|^2 \\ |\chi_{z'x'x'}|^2 \\ |\chi_{x'z'x'}|^2 \\ |\chi_{x'x'z'}|^2 \end{bmatrix} \quad (S26)$$

Combining trigonometric identities $2 \sin \phi \cos \phi = \sin(2\phi)$ and $\cos^2 \phi - \sin^2 \phi = \cos(2\phi)$ together with the equality $|\chi_{x'x'z'}|^2 = |\chi_{z'z'x'}|^2$ for SHG yields the simplified form of the equation given in Eq. (3).

The measured intensity in the laboratory frame can be calculated by combining the first two elements in the laboratory-frame Stoke vector \bar{s}_L using Eq. (S27).

$$\begin{aligned}
I_H^{2\omega} &= \frac{1}{2} [s_{0,L} + s_{1,L}] \\
s_{0,L} &= I_H + I_V \\
s_{1,L} &= I_H - I_V
\end{aligned} \quad (S27)$$

The measured intensity for polarizer at an arbitrary angle ϕ_{pol} can similarly be obtained by projecting the laboratory frame Stokes vector \bar{s}_L onto the reference frame of the polarizer given by \bar{s}_{pol} , given in Eq.(S28).[2]

$$\bar{s}_{pol} = \begin{bmatrix} 1 & 0 & 0 & 0 \\ 0 & \cos(2\phi_{pol}) & -\sin(2\phi_{pol}) & 0 \\ 0 & \sin(2\phi_{pol}) & \cos(2\phi_{pol}) & 0 \\ 0 & 0 & 0 & 1 \end{bmatrix} \cdot \bar{s}_L \quad (S28)$$

Combining Eq. (S27) and (S28) yields the expression in Eq. (5).

1.4. Measurements acquired with polarized incident light.

The laboratory-frame Jones tensor describing the NLO properties of a uniaxial assembly with the unique axis lying within the field of view is given by Eq.(S29).[4]

$$\begin{bmatrix} \chi_{HHH} \\ \chi_{HHV} \\ \chi_{H VH} \\ \chi_{HVV} \\ \chi_{VHH} \\ \chi_{VHV} \\ \chi_{V VH} \\ \chi_{VVV} \end{bmatrix} = \begin{bmatrix} 2g & g & i \\ f-h & -h & h \\ f-h & -h & h \\ -2g & i & g \\ -2h & f & h \\ i-g & -g & g \\ i-g & -g & g \\ 2h & h & f \end{bmatrix} \cdot \begin{bmatrix} \chi_{x'x'z'} \\ \chi_{z'x'x'} \\ \chi_{z'z'z'} \end{bmatrix} \cdot \begin{pmatrix} f = \sin^3 \phi \\ g = \sin^2 \phi \cos \phi \\ h = \sin \phi \cos^2 \phi \\ i = \cos^3 \phi \end{pmatrix} \quad (S29)$$

In Eq.(S29), ϕ is the rotation angle of the primary sample z' -axis relative to the laboratory horizontal axis. The Jones vector describing the polarization-dependent SHG is linked to the Jones tensor and the rotation angle γ of the incident polarization through the following expression.

$$\bar{e}_L^{2\omega} = \begin{bmatrix} \cos^2 \gamma & \sin \gamma \cos \gamma & \sin \gamma \cos \gamma & \sin^2 \gamma & 0 & 0 & 0 & 0 \\ 0 & 0 & 0 & 0 & \cos^2 \gamma & \sin \gamma \cos \gamma & \sin \gamma \cos \gamma & \sin^2 \gamma \end{bmatrix} \cdot \begin{bmatrix} \chi_{HHH} \\ \chi_{HHV} \\ \chi_{H VH} \\ \chi_{HVV} \\ \chi_{VHH} \\ \chi_{VHV} \\ \chi_{V VH} \\ \chi_{VVV} \end{bmatrix} \quad (S30)$$

The SHG intensity detected through a polarizer rotated an angle ϕ_{pol} is given by the following expression.

$$\begin{aligned}
I^{2\omega}(\phi_{pol}) &\propto \begin{bmatrix} 1 & 0 \\ 0 & 0 \end{bmatrix} \begin{bmatrix} \cos \phi_{pol} & \sin \phi_{pol} \\ -\sin \phi_{pol} & \cos \phi_{pol} \end{bmatrix} \begin{bmatrix} e_H^{2\omega} \\ e_V^{2\omega} \end{bmatrix}^2 \\
&\propto \left| e_H^{2\omega} \cos \phi_{pol} + e_V^{2\omega} \sin \phi_{pol} \right|^2
\end{aligned} \tag{S31}$$

In the case of vertically polarized incident light, the combination of Eqs. (S30) and (S31) yields the following simplified expression.

$$I^{2\omega}(\phi_{pol})^2 \propto \left| \chi_{HVV} \cos \phi_{pol} + \chi_{VTV} \sin \phi_{pol} \right|^2 \tag{S32}$$

Substitution of the relations in Eq. (S29) followed by trigonometric simplification yields Eq.(S33).

$$I^{2\omega}(\phi_{pol}) \propto \left[\chi_{x'x'z'} \sin(2\phi) \cos(\phi - \phi_{pol}) + \sin(\phi - \phi_{pol}) \left[\chi_{z'x'x'} \cos^2 \phi + \chi_{z'z'z'} \sin^2 \phi \right] \right]^2 \tag{S33}$$

In the specific case of z-cut quartz, the following equalities emerge by symmetry:

$\chi_{z'z'z'} = -\chi_{z'x'x'} = -\chi_{x'x'z'}$. Substitution of this equality into Eq. (S33) yields the simple two-parameter expression for the anticipated SHG produced for a z-cut quartz sample rotated an angle ϕ_0 driven by horizontally polarized incident light given in Eq. (7).

1.5. Derivation of tilt angle θ .

In order to illustrate the effect of polar tilt angle of collagen fiber, a mathematical relation between measured laboratory frame ratio (ρ), local frame ratio (ρ) and polar tilt angle (θ) was derived by projecting local tensor element onto the lab frame.[5] The projected laboratory frame tensors χ_{XXX} and χ_{XYX} are shown in Eqs. (S34) and (S35) respectively, where $\chi_{z'z'z'}$ and $\chi_{z'x'x'}$ are local frame tensors.

$$\chi_{XXX} = \chi_{z'z'z'} \cdot \sin^3 \theta + 3\chi_{x'x'z'} \cdot \sin \theta \cdot \cos^2 \theta \tag{S34}$$

$$\chi_{XYX} = \chi_{x'x'z'} \cdot \sin \theta \tag{S35}$$

The laboratory frame tensor ratio (ρ) is defined as $\rho \equiv \chi_{XXX} / \chi_{XYX}$, which can be described as Eq. (S36).

$$\rho = \frac{\chi_{XXX}}{\chi_{XYX}} = \frac{\chi_{z'z'z'} \cdot \sin^3 \theta + 3\chi_{z'x'x'} \cdot \sin \theta \cdot \cos^2 \theta}{\chi_{z'x'x'} \cdot \sin \theta} \quad (\text{S36})$$

Since the local frame tensor ratio is defined as $\rho_l \equiv \chi_{z'z'z'} / \chi_{z'x'x'}$. Calculations of tilt angle θ for a specific chromophore can be simplified as Eq. (S37), leading to Eq. (7).

$$\sin^2 \theta = \frac{\rho - 3}{\rho_l - 3} \quad (\text{S37})$$

REFERENCES

- [1] E. L. DeWalt, S. Z. Sullivan, P. D. Schmitt, R. D. Muir, and G. J. Simpson, *Anal. Chem.* **86**, 8448 (2014).
- [2] G. J. Simpson, *J. Phys. Chem. B.* **120**, 3281 (2016).
- [3] R. M. A. Azzam and N. M. Bashara, *Ellipsometry and Polarized Light* (Elsevier, Amsterdam, 1987).
- [4] X. Y. Dow, E. L. DeWalt, J. A. Newman, C. M. Dettmar, and G. J. Simpson, *Biophys. J.* **111**, 1553 (2016).
- [5] A. J. Moad and G. J. Simpson, *J. Phys. Chem. B.* **108**, 3548 (2004).



Axially-offset differential interference contrast microscopy via polarization wavefront shaping

CHANGQIN DING,¹ CHEN LI,¹ FENGYUAN DENG,^{1,2} AND GARTH J. SIMPSON^{1,*}

¹Department of Chemistry, Purdue University, 560 Oval Drive, West Lafayette, Indiana 47907, USA

²Current address: Department of Electrical and Computer Engineering, Boston University, 8 St. Mary's Street, Boston, MA 02215, USA

*gsimpson@purdue.edu

Abstract: Sample-scan phase contrast imaging was demonstrated by producing and coherently recombining light from a pair of axially offset focal planes. Placing a homogeneous medium in one of the two focal planes enables quantitative phase imaging using only common-path optics, recovering absolute phase without halo or oblique-illumination artifacts. Axially offset foci separated by 70 μm with a 10x objective were produced through polarization wavefront shaping using a matched pair of custom-designed microretarder arrays, compatible with retrofitting into conventional commercial microscopes. Quantitative phase imaging was achieved by two complementary approaches: i) rotation of a half wave plate, and ii) 50 kHz polarization modulation with lock-in amplification for detection.

© 2019 Optical Society of America under the terms of the [OSA Open Access Publishing Agreement](#)

1. Introduction

Phase-sensitive microscopy, including Zernike phase contrast and Nomarski differential interference contrast (DIC), allows visualization of weakly scattered samples with low contrast in conventional bright field microscopy [1–3]. Zernike phase contrast produces intensity contrast dependent on spatial interference between light patterned with annular rings, effectively highlighting phase differences between relatively tightly focused and relatively gently focused beams. Nomarski DIC instead produces contrast from interference between laterally offset locations within the field of view. In DIC, a Nomarski prism splits linearly polarized incident light to two orthogonally polarized components with a slight angle offset. By recombining the two components using a matched Nomarski prism, the resulting interferogram at a particular position within the field of view scales with the phase difference between that location and an adjacent spatially offset position. DIC microscopy has been actively used in biological research since the 1970s, including observing neurons in unstained tissue slices [4], studying kinesin-driven movement [5], visualizing microtubule-related motility in cells [6], etc. In both Nomarski and Zernike phase contrast imaging, artifacts related to the interference between locations within the field of view complicate image interpretation. Specifically, Zernike images generally produce orientation-independent “halo” artifacts and Nomarski orientation-dependent “side lighting” artifacts. Furthermore, both phase contrast microscopy and DIC microscopy lack the capability to quantitatively retrieve the absolute phase information from the recorded images without careful calibration [7].

To achieve artifact-free quantitative phase imaging (QPI), Gabor suggested the use of interferometry to quantitatively recover the complex optical field [8], in which a beam is split and recombined at an angle such that the focal plane array records an interferogram [9–12]. Based on the same physical principles, many other interferometric QPI approaches were developed recently [7,13,14]. Although the abovementioned QPI methods can provide

quantitative phase information with high precision, these dual-path interferometric approaches face the common problem of being vulnerable to environmental perturbations such as mechanical vibrations and temperature changes since the reference beam does not pass through the same optical path as the light coming from the object. In addition, the requirement of a long coherence-length reference beam increases the complexity of these QPI systems making them incompatible with retrofitting into existing microscopy systems. Finally, phase retrieval in dual-path QPI is performed by image analysis relative to a background, which can be challenging in complex samples for which a background reference is not trivially available.

Recent developments have helped address the limitations of dual-path interferometry for QPI. In work by Popescu and associates, a diffraction grating and spatial filter were used to produce interference from the 0th and 1st order of diffraction from the same microscope output, suppressing the phase instability in dual-path QPI microscopy [15–17]. However, these interference approaches are still inherently underdetermined; both phase and intensity must be inferred by image reconstruction rather than directly and independently measured at each pixel. As an alternative, Fourier ptychography [18], phase retrieval with designed periphery [19], using patterned illumination [20] or spatial light modulation for image shifting [21], and coherent diffraction imaging [22] recover the absolute relative phase information from adjacent objects without a reference beam. However, these methods are based on assumptions on the beam passing through the object and mathematically inferred a reference wavefront, complicating both the image acquisition and the post-processing. Therefore, an approach capable of independently recovering absolute phase at every pixel using common path optics may have distinct advantages in phase recovery for complex objects with low spatial correlation. Additionally, architectures that are compatible with retrofitting into existing microscopes rather than requiring custom designs have the potential to greatly expand the broader use and access to artifact-free QPI.

In the present work, axially-offset differential interference contrast (ADIC) microscopy for QPI was developed via polarization wavefront shaping using a matched pair of micro-retarder arrays (μ RAs). The μ RA is a custom optic enabling patterning of the retardance and fast axis orientation of a liquid crystal on a per-pixel basis. Polarization wavefront shaping using the μ RA to produce a polarization-dependent pattern expected from the combination of orthogonally polarized divergent and convergent beams. For linearly polarized incident light and half-wave retardance in every pixel in the μ RA, the polarization wavefront is identical to that produced by the interference between a slightly diverging right circularly polarized (RCP) plane wave and a slightly converging left circularly polarized (LCP) plane wave. After passing through a 10x objective, each of the orthogonal polarization components focus to separate focal planes separated by 70 μ m (~5.6 times the depth of field), serving as sample and reference planes. Two strategies, including half wave plate (HWP) rotation and lock-in amplified (LIA) detection, were adopted in ADIC microscopy for simultaneous retrieval of transmittance (real component of the image) and quantitative phase (imaginary component) images. The recovered quantitative phase (QP) images agreed well between the two strategies with a phase range from $-\pi$ to π and a detection limit of 0.033 radian. Silica microbeads were used to investigate the refractive index with an agreement between the measurement and the refractive index of amorphous bulk silica. QP images in tissue section samples were measured by using ADIC microscopy.

2. Methods

2.1 Sample preparation

Two separate samples were prepared for analysis by ADIC: silica beads and mouse tail sections. Silica beads sized in diameter of 8 μ m were donated by Prof. Mary Wirth (Purdue University, West Lafayette, IN). For quantitative phase imaging, the silica beads were

dispersed by ultrasonication in a commercially available nitrocellulose matrix with a high vapor pressure solvent plasticizer (Sally Hanson nail polish, Hardener) before sealing between a cover slip and a glass slide, followed by solvent evaporation. Mouse tail sections were provided by Prof. Philip Low (Purdue University, West Lafayette, IN). Mouse tails were first decalcified in the solution of 23% formic acid, 4% formalin, and 1% methanol for 2 hours, followed by sectioning longitudinally to ensure that sections were retrieved from the central region of the tail. The mouse tail section was then fixed in 10% formalin and embedded in paraffin prior to microtoming into 4 μm thick slides. After sectioning, the mouse tail was stained by hematoxylin and eosin.

2.2 Principles of polarization wavefront shaping by μRA

A linearly polarized incident beam can be viewed as a coherent combination of two orthogonally polarized components. In standard DIC, linearly polarized incident light is split into horizontally polarized and vertically polarized light using Nomarski prism [23]. In the more general case, the polarization state of light at any position on the Poincaré sphere can also be defined by a coherent combination of two orthogonally polarized components, such as RCP and LCP light.

While most conventional optics affect the polarization state of the entire beam identically, waveplate arrays, such as liquid crystal polymer waveplates, allow the tailoring of the polarization state of light on a per pixel basis. The geometrical phase modulation can be achieved by orientation modulation of liquid crystal polymers on thin polymer substrates. Waveplate arrays have been developed for adaptable lenses [24,25], grating prisms [26,27], spiral phase retarders [28–30], etc. Wavefront shaping has been used to split beam into beamlets of orthogonally polarized light focused or defocused depending on the handedness of polarization of the beam [31]. In the present work, a retardance pattern of concentric rings with a quadratic spacing was designed to produce an orthogonally polarized pair of converging and diverging beams.

The pattern necessary to produce this beam pair is most intuitively understood by first considering the anticipated polarization-dependent pattern produced by the interference of orthogonally polarized converging and diverging plane waves. The overlay of converging right circular and diverging left circularly polarized beams produces linearly polarized light with the axis of polarization rotated in a radial pattern as shown in Fig. 1(A), which has similarities to a Fresnel zone plate. Designing a μRA to produce this pattern for a linearly polarized incident beam therefore generates diverging and converging components, which can be recombined using a paired μRA in transmission. For linearly polarized incident light with the plane of polarization given by the angle γ , decomposition into the RCP and LCP contributions yields the expression shown in Eq. (1).

$$\begin{pmatrix} \cos(\gamma) \\ \sin(\gamma) \end{pmatrix} = \frac{1}{2} \cdot e^{-i\gamma} \cdot \begin{pmatrix} 1 \\ i \end{pmatrix} + \frac{1}{2} \cdot e^{i\gamma} \cdot \begin{pmatrix} 1 \\ -i \end{pmatrix} \quad (1)$$

In this work, μRAs were designed with the pattern of half-wave retardance of 532 nm light at every position varying spatially in the azimuthal orientation of the fast-axis with a 60 $\mu\text{m} \times 60 \mu\text{m}$ pixel size per entry and an active radius of 12 mm. The azimuthal orientation θ as a function of x, y position agrees to the relationship $\theta(x, y) = 2\pi[(x-r)^2 + (y-r)^2]/4f\lambda$, in which r is the active radius, f is focal length designed as 6.28 m and λ is the targeting wavelength as 532 nm. The azimuthal orientation was then wrapped in the range of $[0, \pi]$. The designed μRA was then custom produced by Thorlabs. No artifacts from the periodicity inherent in the μRA design were detectable in either the measured intensity patterns shown in Fig. 1(A) or in the resulting QP images. Unlike Nomarski DIC, in which the split beams are offset laterally within the sample plane [Fig. 1(B)], the decomposed converging LCP and diverging RCP light after the μRA were offset axially after the same objective, such that the

reference beam was defocused within the sample plane [Fig. 1(C)]. Axially offsetting the two focal planes allowed the use of a homogeneous medium (e.g. glass, solvent, air) as a reference. In the absence of a sample, a paired identical μ RA in transmittance coherently recombined the two orthogonal components to recover a plane wave with the original polarization state of the incident light. Phase contrast imaging can be performed by placing a polarizer in the quadrature position, with shifts in phase between the sample and reference planes resulting in changes in polarization states, and correspondingly, changes in detected intensity. Modulating the polarization states of the incident light allows for signal to noise enhancement through LIA detection.

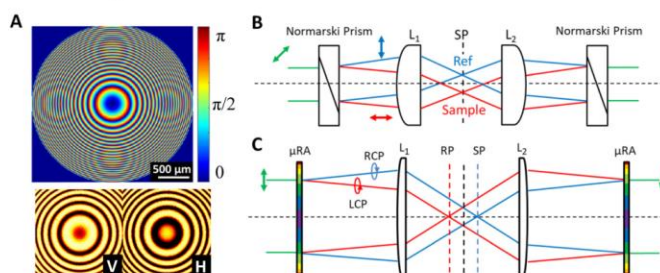


Fig. 1. (A) The design of μ RA as half-wave retardance with spatially varied azimuthal orientation of the fast-axis targeted for 532 nm light. Scale bar: 500 μ m. Bottom: part of the measured different intensity distribution with horizontal (H) and vertical (V) polarization detection when horizontally polarized light passing through the μ RA. (B) The working principle of traditional Nomarski phase contrast microscope. (C) The working principle of ADIC microscope. L1 and L2: lens; RP: reference plane; SP: sample plane.

2.3 Instrumentation for ADIC microscopy

ADIC microscope was constructed based on a bright field microscope frame with the addition of several polarizing optics (Fig. 2). In brief, a 532 nm continuous laser (Millenia Vs J) was used for illumination with initial horizontal polarization, followed with a half wave plate (HWP) inserted in a rotation stage for linearly polarization modulation of the incident light. The beam was expanded to 15 mm in diameter to fill approximately half the area of the μ RA and the full aperture of a 10x objective (0.3 NA, Nikon). The average laser power on the sample was around 5 mW. An identical 10x 0.3 NA objective was used as a condenser in transmittance, followed by passage through a paired μ RA, positioned and oriented to recover an identical polarized plane wave in the absence of a sample. A sample scanning stage (Mad city labs Nano-Bio300) was driven by two phase-locked function generators (Tektronix AFG2021 and Agilent 33220A) for image acquisition with a frame rate of 20 s with a field of view (FoV) of 250 μ m \times 250 μ m. Horizontally polarized transmittance was detected by passing the beam through a polarizer (LPNIRE100-B, Thorlabs) and a photodiode (DET-10A, Thorlabs). Signals were digitized at 20 kHz using a PCI-E digitizer oscilloscope cards (AlazarTech ATS-9462) and remapped into 200 \times 200 images via custom software (MATLAB), giving a pixel size of 1.25 μ m/pixel. Polarization modulation measurements were conducted via mechanical rotation of the HWP from 0 to 90 degrees with 3-degree intervals. For the fast polarization modulation coupled with LIA (Stanford Research Systems SR810) detection, a photoelastic modulator (PEM, Hinds instrument PEM-90M) was inserted between HWP and a quarter waveplate (QWP). PEM is made of isotropic optical materials and introduce retardance [$\Delta(\tau)$] to the incident light as a function of time when driven at a resonant frequency. It has two electric TTL outputs with one has the modulation frequency (1f) and the other has the doubled frequency (2f) of the sinusoidal driven electric field. The

fast axis of the HWP, PEM and QWP were rotated to 22.5° , 0° and 45° , respectively, for modulation of the linearly polarized light before entering the μ RA, as detailed in Eqs. (7) and (8) (Section 2.4). The PEM was operating at its resonance frequency of 50 kHz, with both $1f$ (50 kHz) and $2f$ (100 kHz) outputs delivered as the reference signals to the LIA. Both the quadrature and in-phase components of the LIA output were acquired simultaneously. The per-pixel integration time of the LIA was 30 μ s. The same setup was used for both the investigation experiment of the dual-foci and the later QPI experiments.

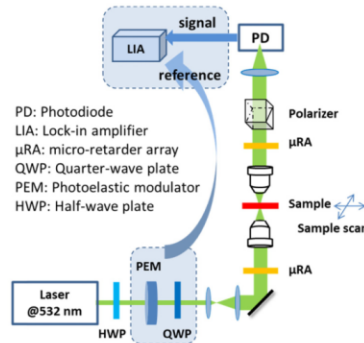


Fig. 2. Experiment set-up for QPI with a 10x objective to recover both bright field images and QP images. Blue circled optics: add-in parts for LIA detection.

2.4 QP image recovery

In the absence of a sample, the identity matrix produced by the sequential combination of the matched ADIC optics can be decomposed as a linear combination of Hermitian Pauli matrices as shown in Eq. (2). The decomposed matrices can describe the Jones matrices corresponding to the two foci with orthogonal polarized components.

$$\vec{e}^0 = \begin{pmatrix} 1 & 0 \\ 0 & 1 \end{pmatrix} \cdot \vec{e}^0 = \frac{1}{2} \left\{ \left[\begin{pmatrix} 1 & 0 \\ 0 & 1 \end{pmatrix} + \begin{pmatrix} 0 & i \\ -i & 0 \end{pmatrix} \right] + \left[\begin{pmatrix} 1 & 0 \\ 0 & 1 \end{pmatrix} + \begin{pmatrix} 0 & -i \\ i & 0 \end{pmatrix} \right] \right\} \cdot \vec{e}^0 \quad (2)$$

When a sample-induced phase shift is introduced in either focal plane, the Jones vector describing the signal electric field (\vec{e}^{det}) after the sample can be expressed by Eq. (3). The complex-valued amplitude transmittances t^+ and t^- describe the field detected following interaction in the two foci separately. The phase change δ induced by the sample at a given location is defined to be the phase shift between the two orthogonally polarized focal planes (sample and reference planes). In the absence of a sample, $|t^+| = |t^-| = 1$ and $\delta = 0$, resulting in $\vec{e}^{\text{tot}} = \vec{e}^0$ that the detecting signals are identical to the incident light.

$$\vec{e}^{\text{tot}} = \frac{1}{2} \left(|t^+| \cdot \begin{bmatrix} 1 & i \\ -i & 1 \end{bmatrix} \cdot e^{i\frac{\delta}{2}} + |t^-| \cdot \begin{bmatrix} 1 & -i \\ i & 1 \end{bmatrix} \cdot e^{-i\frac{\delta}{2}} \right) \cdot \vec{e}^0 \quad (3)$$

The (+) and (-) focal planes produced by the μ RA are orthogonally polarized relative to each other and 90 degrees phase-shifted relative to the incident polarization state (e.g., for linearly polarized light, the polarization states of the (+) and (-) focal planes are RCP and LCP, respectively, while for RCP incident light, the (+) and (-) focal planes are horizontally and vertically polarized light, respectively). In the case of half wave plate rotation strategy

describing horizontally polarized light passing through a half wave plate with fast axis rotated to angle γ , the Jones vector describing the incident light is given by the following expression:

$$\overline{e^0(\gamma)} = \begin{bmatrix} \cos 2\gamma & \sin 2\gamma \\ \sin 2\gamma & -\cos 2\gamma \end{bmatrix} \cdot \begin{bmatrix} 1 \\ 0 \end{bmatrix} \quad (4)$$

The detected intensity through a polarizer rotated to angle ϕ_{pol} is given by Eq. (5).

$$\overline{e^{det}(\gamma)} = \begin{bmatrix} \cos \phi_{pol} & -\sin \phi_{pol} \\ \sin \phi_{pol} & \cos \phi_{pol} \end{bmatrix} \begin{bmatrix} 1 & 0 \\ 0 & 0 \end{bmatrix} \begin{bmatrix} \cos \phi_{pol} & \sin \phi_{pol} \\ -\sin \phi_{pol} & \cos \phi_{pol} \end{bmatrix} \cdot \overline{e^{tot}(\gamma)} \quad (5)$$

$$I(\phi_{pol}, \gamma) \propto \left| \overline{e^{det}(\gamma)} \right|^2 \quad (6)$$

when detecting the horizontally polarized component ($\phi_{pol} = 0$), combining the expressions in Eqs. (3), (4), (5) and (6) followed by simplification yields Eq. (7), in which γ is the rotated angle of the incident HWP.

$$I(\gamma) \propto |t^+|^2 + |t^-|^2 + 2|t^+||t^-| \cdot \cos(\delta + 4\gamma) \quad (7)$$

For the LIA detection, the PEM and the QWP were placed between the HWP and pair of lenses for beam expansion, and the fast axis of HWP and QWP were rotated to 22.5° and 45° , respectively, as shown in Fig. 2. The Jones vector describing the incident light is given by the following Eq. (8), in which $\Delta(\tau)$ is the retardance modulation introduced by the PEM as a function of time (τ) with a modulation amplitude of $2A$, as defined in Eq. (9). It can be seen that with a horizontally polarized incident light, a linearly polarized light was generated after HWP, PEM and QWP to pass through the μ RA. The retardance modulation frequency for the PEM was $f = 50$ kHz.

$$\overline{e^0(\tau)} \propto \begin{bmatrix} 1 & -i \\ -i & 1 \end{bmatrix} \cdot \begin{bmatrix} e^{-i\Delta(\tau)/2} & 0 \\ 0 & e^{i\Delta(\tau)/2} \end{bmatrix} \cdot \begin{bmatrix} 1 & 1 \\ 1 & -1 \end{bmatrix} \cdot \begin{bmatrix} 1 \\ 0 \end{bmatrix} = \sqrt{2}(1-i) \begin{bmatrix} \sin\left(\frac{\Delta(\tau)}{2} + \frac{\pi}{4}\right) \\ \cos\left(\frac{\Delta(\tau)}{2} + \frac{\pi}{4}\right) \end{bmatrix} \quad (8)$$

$$\Delta(\tau) = 2A \cdot \sin(2\pi f \tau) \quad (9)$$

The time-dependent detected signal intensity of the horizontally polarized component measured in transmission is given by combining Eqs. (3), (5), (8) and (9).

$$I(\tau) \propto |t^+|^2 + |t^-|^2 + 2|t^+||t^-| \cdot \sin(\Delta(\tau) - \delta) \quad (10)$$

when A is relatively small, a Taylor series expansion of Eq. (10) with respect to τ shown in Eq. (11) converges rapidly.

$$I(\tau) \propto 2(|t^+|^2 + |t^-|^2) + 2|t^+||t^-| \cdot \left[\left[\left(2A - A^3 + \frac{A^5}{6} - \frac{A^7}{72} + \dots \right) \cdot \sin(2\pi f \tau) + \left(\frac{A^3}{3} - \frac{A^5}{12} + \frac{A^7}{120} + \dots \right) \cdot \sin(3 \cdot 2\pi f \tau) + \dots \right] \cdot \cos \delta \right. \\ \left. - \left[\left(1 - A^2 + \frac{A^4}{4} - \frac{A^6}{36} + \dots \right) + \left(A^2 - \frac{A^4}{3} + \frac{A^6}{24} + \dots \right) \cdot \cos(2 \cdot 2\pi f \tau) + \left(\frac{A^4}{12} - \frac{A^6}{60} + \dots \right) \cdot \cos(4 \cdot 2\pi f \tau) + \dots \right] \cdot \sin \delta \right] \quad (11)$$

According to Eq. (11), the quadrature components (sine) only map to the odd harmonics of the Taylor series, while the in-phase components (cosine) terms are only present in the even

harmonics. The proportionality in Eq. (11) evaluated at seventh order will result in negligible errors for the PEM modulation for $A < \pi/2$. In our experiments, the modulation amplitude of the PEM was set as $A = 0.3\pi$, consistent with the range indicated. Retaining the first seven terms of the expansion, the quadrature components (sine, Y) of the first harmonic ($1f$) and the in-phase components (cosine, X) of the second harmonic ($2f$) LIA detection are written as Eqs. (12) and (13), respectively.

$$1f_Y \approx 2|t^+||t^-| \cdot \left(2A - A^3 + \frac{A^5}{6} - \frac{A^7}{72} \right) \cdot \cos \delta \quad (12)$$

$$2f_X \approx -2|t^+||t^-| \cdot \left(A^2 - \frac{A^4}{3} + \frac{A^6}{24} \right) \cdot \sin \delta \quad (13)$$

Combining Eqs. (12) and (13), one can recover values of $\cos \delta$ and $\sin \delta$ regarding $1f_Y$, $2f_X$, and the PEM modulation A . Then δ can be achieved through Eq. (14) in a range of $[-\pi, \pi]$.

$$\delta = \text{Im}[\text{In}(\cos \delta + i \sin \delta)] \quad (14)$$

Unlike the HWP rotation strategy, the transmittance image recovered from the LIA detection is defined as $|t^+||t^-|$. It is noteworthy that both the HWP and PEM polarization rotation strategies recover phase values in the range of $[-\pi, \pi]$.

3. Results

3.1 Experimental evidence of axially-offset dual-foci produced by μ RA

Experimental measurements of a 1951 USAF resolution test chart were performed to assess the change in 3D point spread function induced by the μ RA, the results of which are shown in Fig. 3. From the images, the radial extent of the point spread function was evaluated based on edge analysis, in which the derivative of the intensity profile was fit to a Gaussian function to recover the RMS (root mean square) beam width. Plots of the recovered Gaussian beam cross-section are shown in Fig. 3 for multiple z-positions of the test grid in order to map the beam profile in all three dimensions assuming cylindrical symmetry. For an object (e.g., the test grid) initially in the focal plane of the microscope, addition of the μ RA resulted in a slight blurring. However, crisp images were recoverable upon axial translation of either $\pm 35 \mu\text{m}$. Consistent with this observation, analysis of the images shown in Fig. 3(A) generated by the wavefront shaping of the μ RA produced two foci separate by $70 \mu\text{m}$ symmetrically distributed about the original focal plane [Fig. 3(B)]. Due to analysis of the results summarized in Fig. 3, the cross-sections of the axially offset foci are statistically indistinguishable from the original focus, indicating no substantial perturbation to the point spread function upon addition of the μ RA. Comparison of the point-spread functions between Figs. 3(A) and 3(B) indicates that the spatial resolution ($\sim 2 \mu\text{m}$) is unchanged by the addition of the μ RAs. The introduction of the large spatial offset between the two foci (roughly 1/4 of the $250 \mu\text{m} \times 250 \mu\text{m}$ FoV) makes it possible to create a stable and uniform reference plane positioned within a homogeneous medium (e.g., glass, air, or solution) immediately adjacent to the sample plane, removing imaging artifacts arising from the use of sample and reference locations cohabitating in the focal plane as in Nomarski and Zernike phase contrast microscopy.

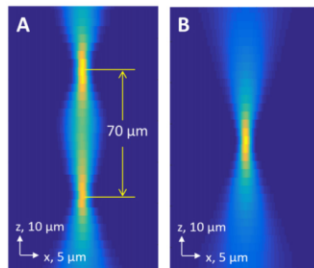


Fig. 3. Measured point spread functions in the x-z plane with (A) and without (B) the μ RA installed in the beam path.

3.2 QPI through HWP rotation

To retrieve the QP images from ADIC imaging using the HWP rotation strategy, a whole set of images was collected with the HWP rotating through a 90-degree range, with the horizontally polarized transmitted beam detected using a photodiode. The whole set of images with HWP at different angles can be found in [Visualization 1](#), Supplementary Materials. Then a pixel-by-pixel nonlinear fit was applied to the intensity trace as a function of the HWP rotation angle γ referring to Eq. (3) to recover images of phase (δ) and transmittance [$(|t^+| + |t^-|)^2$]. Figures 4(A) and 4(B) show the recovered transmittance and QP image from a stained mouse tail section. The areas with larger magnitude phase shift [red and blue areas in Fig. 4(B)] highlight the detailed spatial distribution of the fibrils in mouse tail tissues, which produced low contrast in the retrieved transmittance image. The average intensities of the blank (no sample) areas in the raw ADIC image were used to calibrate the detector sensitivity and the HWP rotation angle used in Eq. (3) as shown in Fig. 4(C). The measured intensity trace and fitted results show excellent agreement, supporting the validity of this calibration strategy. The $\sim 6^\circ$ phase shift in the HWP rotation angle corresponding to the minimum transmitted intensity of the blank is attributed to uncertainty in the μ RA orientations, which were not in precision rotation stages. Fits for quantitative phase retrieval for two representative pixels in the image are shown in Fig. 4(D), with good agreement between the measurements (dots and stars) and fits (lines). The mean of the sum of squared errors of prediction (SSE) and the coefficient of determination (R^2) for the nonlinear fit for the whole FoV were 0.0018 and 0.9164, respectively. These results confirm the degree of statistical confidence with which the phase angle can be recovered by nonlinear fitting.

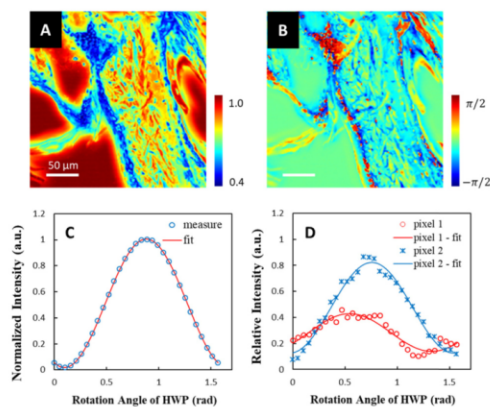


Fig. 4. Transmittance image (A) and QP images (B) recovered with half wave rotation measurement of a single FoV of mouse tail section. (C) Overlay of the measured intensity of background (dots) with its nonlinear fit result (solid line). (D) Overlay of the measured intensity of random pixels (dots) with its nonlinear fit result (solid line) to recover transmittance image and phase contrast image. Scale bar: 50 μm .

3.3 QPI through LIA detection

For LIA detection, both the pure-tone $1f$ (50 kHz) and $2f$ (100 kHz) signals generated by the PEM were used as references for the LIA. The raw images (cosine components and sine components) collected from $1f$ and $2f$ LIA measurements were shown in Figs. 5(A)-5(D) for the same FoV of a mouse tail section. Figures 5(A) and 5(B) share the same image contrast settings, as did Figs. 5(C) and 5(D). Consistent with the predictions from Eq. (11), the cosine components of $1f$ and the sine components of $2f$ produced negligible contrast. The transmittance bright field image [Fig. 5(E)] and QP image [Fig. 5(F)] were calculated using Eqs. (12)-(14). Similarities were qualitatively clear between the transmittance bright field image and the sine components of $1f$ LIA detection, as well as between the QP image and cosine components of $2f$ LIA detection. According to Eqs. (12) and (13), the sine components from $1f$ and the cosine components from $2f$ converge to the bright field image and QP image, respectively, in the limit of low phase shifts δ . It can also be seen that the QP image revealed more detailed structures and exhibited higher contrast for those areas with higher transmittance, such as the fibrils shown in the circle in Figs. 5(E) and 5(F).

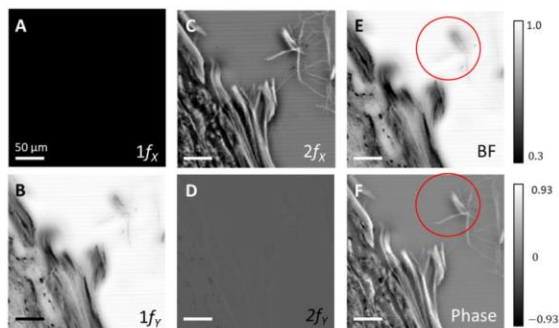


Fig. 5. Images measured from LIA detection with $1f$ (A, B) and $2f$ (C, D) as reference, and the recovered transmittance bright field image (E) and quantitative phase contrast image (F) of a single FoV of mouse tail section. Color bar unit: (E) transmittance percentage, (F) phase shift in radian. Scale bar: $50 \mu\text{m}$.

The agreement between the two QPI strategies applied to the ADIC microscopy, HWP rotation and LIA detection were tested by imaging the same FoV of a mouse tail section as shown in Fig. 6. The transmittance bright field images [Fig. 6(A)] was recovered by nonlinear fitting through the HWP rotation strategy. To compare the retrieved QP images with different approaches [Fig. 6(B) and 6(C)], same image contrast settings were applied. Agreement between the retrieved results from the two strategies provides cross-validation of both approaches. The difference image in phase shift obtained from the two strategies was shown in Fig. 6(D). It can be seen that most differences between the two methods arise at the pixels with larger absolute phase shift values. These differences could be attributed to the phase wrapping issue that is sensitive to spherical structures and phase retrieval strategies.

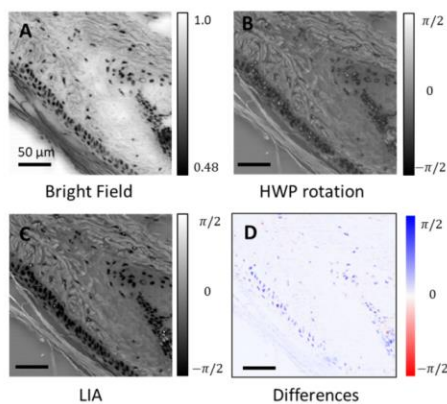


Fig. 6. Transmittance and quantitative phase contrast images recovered from HWP rotation (A, B) and LIA detection (C) strategies of a single FoV of mouse tail section. (D) Differences images of the phase shift calculated from the two strategies. Color bar unit: (A) transmittance percentage, (B-D) phase shift in radian. Scale bar: $50 \mu\text{m}$.

4. Discussion

4.1 Separation distance between the dual-foci for QPI

The separation distance between the two foci depends on the designed periods of the centric polarization rotation pattern of our μ RAs. With smaller periods of the centric modulation pattern in μ RA, larger separation is expected. When the separation distance is much smaller, the setup converges to a result qualitatively analogous to Zernike phase contrast, in which only a single ring is included, and the reference plane is so close to the sample plane that the contrast is simply a halo (i.e., the negligible displacement limit). The upper limit for separating the two foci is ultimately dictated by the manufacturing precision of the μ RAs; a higher density of fringes at the extrema of the array corresponds to a larger separation between foci. Manufacture with the maximum stated manufacturing resolution of $30\ \mu\text{m}$ corresponds to a maximum fringe period of $60\ \mu\text{m}$ (with Nyquist sampling), producing a theoretical separation distance of $360\ \mu\text{m}$ for a $10\times$ objective. In this work, a longer maximum period was used to reduce the potential for artifacts from the discretization effects at the extrema, giving a separation distance of $70\ \mu\text{m}$. By enabling such a large axial offset between the two focal planes, the reference beam is significantly defocused in the sample plane to a spot size of $\sim 44\ \mu\text{m}$ in diameter. As such, the phase shift induced at a given $\sim 3\ \mu\text{m}^2$ location within the sample plane is interfered with the average phase within a $\sim 1500\ \mu\text{m}^2$ area comprising the cross-sectional area of the reference beam within the sample plane. While not serving as an entirely independent reference as in dual-path QPI, the reference effectively spans the optical phase averaged over an area in the field of view ~ 500 -fold larger than the focal volume using common-path optics. For sparse, well-separated objects such as recorded herein, the phase-bias in the reference path induced by the sample is negligible and two conditions converge.

4.2 Limit of detection (LoD) of ADIC-QPI

The images produced by ADIC are free of halo and side-lighting artifacts routinely encountered in Zernike and Nomarski phase contrast methods, respectively. The absence of these artifacts arises from the spherical symmetry of the interference condition coupled with the relatively large area within the field of view serving as a phase reference for the sample plane. The limits of detection for the phase shift calculation from the two strategies were investigated by analyzing the QP images obtained from ADIC microscopy in absence of samples. The measured standard deviation (σ) of each phase image retrieved by the HWP rotation and LIA detection strategies was $0.003\ \text{rad}$ and $0.011\ \text{rad}$, respectively. Thus the LoD (3σ) of each QPI approach was deduced to be $0.009\ \text{rad}$ and $0.033\ \text{rad}$. Considering a thin film of lipid ($n = 1.50$) [32–34] in an aqueous environment ($n = 1.33$) measured using ADIC microscopy, the smallest optical path length that could be determined with the two strategies is $4.5\ \text{nm}$ and $16.4\ \text{nm}$, respectively. Note the self-calibration of the nonlinear fitting could reduce the $1/f$ noise arising from the long acquisition time in the HWP rotation strategy (about $10\ \text{min}$ for a whole set of 90 -degree rotation with 6 -degree intervals, corresponding to integration time of $480\ \mu\text{s}$ for each pixel). However, the pixel-by-pixel nonlinear fitting leads to the time-consuming data analysis process. Due to the limit capability of the LIA used in our experiments, the $1f$ and $2f$ ADIC raw images were acquired separately with different reference signals. In addition, the LIA integration time used in our experiments were limited to $30\ \mu\text{s}$ (3 modulation periods). The ~ 3 -fold improvement in the phase uncertainty using HWP rotation is attributed to the ~ 16 -fold increase in per-pixel measurement time relative to the PEM measurement. Significant improvements are reasonable to expect using longer integration times with simultaneous LIA detection of the $1f$ and $2f$ signals.

4.3 Recovery of refractive index of microspheres

Silica beads 8 μm in diameter were used for quantitative phase imaging and to calculate the refractive index of the silica beads. Figure 7 shows the QP images for the same FoV of 8 μm silica beads retrieved from both HWP rotation and LIA strategies. Great agreement can be seen between the results of the two strategies [Figs. 7(A) and (B)], as mentions in Section 3.3. The refractive index of silica microbeads was calculated based on the measured phase shift and bead size. The phase shift line profile of a single bead [insets of Figs. 7(A) and 7(B)] obtained from both strategies are plotted in Fig. 7(C). The phase shift (δ) in the center of the measured 7.3 μm silica bead was 2.53 radian. Statistical analysis of silica microspheres in Fig. 7 allows us to calculate the difference between the refractive indices of silica bead and nitrocellulose matrix: $\Delta n = \delta\lambda/2\pi D = 0.0293 \pm 0.0007$. Given the refractive index of nitrocellulose is 1.505 at 543.5 nm [35], the refractive index of silica bead is calculated as 1.4757 ± 0.0007 at 532 nm. Although there is no report on the optical constants of silica microparticles, our result is consistent with the refractive index of amorphous bulk silica as 1.461 [36].

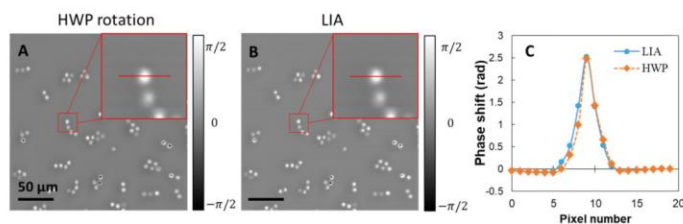


Fig. 7. Quantitative phase contrast images of the same FoV of 8 μm silica beads recovered from both HWP rotation (A) and LIA detection (B) strategies. Color bar unit: phase shift in radian. Scale bar: 50 μm . Inserts: zoom-in for one single bead. (C) Phase shift line profiles of the cross line in the insets retrieved from the HWP rotation (blue dots) and LIA detection (orange squares) approach.

5. Conclusion

A quantitative phase contrast microscope was developed by ADIC imaging through polarization wavefront shaping via a matched pair of μRAs . HWP rotation and LIA detection strategies enabled simultaneous recovery of both transmittance and QP images, with good agreement observed between the recovered QP images from both the strategies. The smallest detectable phase shift was determined to be 0.009 radian in HWP rotation strategy with integration time of 480 μs for each pixel and 0.033 radian in LIA detection strategy with an integration time of 30 μs for each pixel. Proof of concept studies with tissue samples and silica beads indicated excellent agreements between the quantitative phase shift analysis by both HWP rotation and LIA detection strategies, as well as with the theoretical predictions. The μRAs can be customized for particular wavelengths and axial offsets between foci, supporting design for application-specific imaging. ADIC was enabled by the addition of two fixed thin optics within an otherwise standard optical path, suggesting broad compatibility for retrofitting into existing commercial microscopes. In ongoing work, the ADIC is being extended into a wide field quantitative phase contrast imaging using a broadband and spatially incoherent LED illumination source. In addition, another autocorrelation method is also under development using ADIC principle for retrievable of quantitative phase information and the particle size distribution, which can be utilized to calculate the absolute refractive index of nanoparticles.

Funding

National Institutes of Health (NIH) (R01GM-103401).

Acknowledgments

C.L. gratefully acknowledges support from the Purdue Research Foundation. The authors acknowledge Mary Wirth for the contribution of fused silica beads and Philip Low for the mouse tail sections.

Disclosures

The authors declare that there are no conflicts of interest related to this article.

References

1. F. Zernike, "Phase contrast, a new method for the microscopic observation of transparent objects part II," *Physica* **9**(10), 974–986 (1942).
2. F. Zernike, "How I discovered phase contrast," *Science* **121**(3141), 345–349 (1955).
3. N. Georges, "Interferential polarizing device for study of phase objects," US patent, US2924142A (1960).
4. H.-U. Dodt and W. Ziegler, "Visualizing unstained neurons in living brain slices by infrared DIC-video microscopy," *Brain Res.* **537**(1-2), 333–336 (1990).
5. J. Gelles, B. J. Schnapp, and M. P. Sheetz, "Tracking kinesin-driven movements with nanometre-scale precision," *Nature* **331**(6155), 450–453 (1988).
6. R. D. Allen, N. S. Allen, and J. L. Travis, "Video-enhanced contrast, differential interference contrast (AVEC-DIC) microscopy: a new method capable of analyzing microtubule-related motility in the reticulopodial network of *Allogromia laticollaris*," *Cell Motil.* **1**(3), 291–302 (1981).
7. T. Ikeda, G. Popescu, R. R. Dasari, and M. S. Feld, "Hilbert phase microscopy for investigating fast dynamics in transparent systems," *Opt. Lett.* **30**(10), 1165–1167 (2005).
8. D.-I. D. Gabor, "Microscopy by reconstructed wave-fronts," *Proc. R. Soc. Lond. A Math. Phys. Sci.* **197**(1051), 454–487 (1949).
9. T. Zhang and I. Yamaguchi, "Three-dimensional microscopy with phase-shifting digital holography," *Opt. Lett.* **23**(15), 1221–1223 (1998).
10. C. Mann, L. Yu, C.-M. Lo, and M. Kim, "High-resolution quantitative phase-contrast microscopy by digital holography," *Opt. Express* **13**(22), 8693–8698 (2005).
11. M. K. Kim, "Digital holographic microscopy," in *Digital Holographic Microscopy* (Springer, 2011), pp. 149–190.
12. L. Miccio, A. Finizio, R. Puglisi, D. Balduzzi, A. Galli, and P. Ferraro, "Dynamic DIC by digital holography microscopy for enhancing phase-contrast visualization," *Biomed. Opt. Express* **2**(2), 331–344 (2011).
13. J. W. Goodman and R. W. Lawrence, "Digital image formation from electronically detected holograms," *Appl. Phys. Lett.* **11**(3), 77–79 (1967).
14. Z. Wang, L. Millet, M. Mir, H. Ding, S. Unarunotai, J. Rogers, M. U. Gillette, and G. Popescu, "Spatial light interference microscopy (SLIM)," *Opt. Express* **19**(2), 1016–1026 (2011).
15. G. Popescu, T. Ikeda, R. R. Dasari, and M. S. Feld, "Diffraction phase microscopy for quantifying cell structure and dynamics," *Opt. Lett.* **31**(6), 775–777 (2006).
16. B. Bhaduri, H. Pham, M. Mir, and G. Popescu, "Diffraction phase microscopy with white light," *Opt. Lett.* **37**(6), 1094–1096 (2012).
17. B. Bhaduri, C. Edwards, H. Pham, R. Zhou, T. H. Nguyen, L. L. Goddard, and G. Popescu, "Diffraction phase microscopy: principles and applications in materials and life sciences," *Adv. Opt. Photonics* **6**(1), 57–119 (2014).
18. G. Zheng, R. Horstmeyer, and C. Yang, "Wide-field, high-resolution Fourier ptychographic microscopy," *Nat. Photonics* **7**(9), 739–745 (2013).
19. A. Jesacher, W. Harn, S. Bernet, and M. Ritsch-Marte, "Quantitative single-shot imaging of complex objects using phase retrieval with a designed periphery," *Opt. Express* **20**(5), 5470–5480 (2012).
20. L. Tian and L. Waller, "3D intensity and phase imaging from light field measurements in an LED array microscope," *Optica* **2**(2), 104–111 (2015).
21. T. J. McIntyre, C. Maurer, S. Fassi, S. Khan, S. Bernet, and M. Ritsch-Marte, "Quantitative SLM-based differential interference contrast imaging," *Opt. Express* **18**(13), 14063–14078 (2010).
22. H. N. Chapman and K. A. Nugent, "Coherent lensless X-ray imaging," *Nat. Photonics* **4**(12), 833–839 (2010).
23. J. S. Hartman, R. L. Gordon, and D. L. Lessor, "Nomarski differential interference contrast microscopy for surface slope measurements: an examination of techniques," *Appl. Opt.* **20**(15), 2665–2669 (1981).
24. S. Sato, "Liquid-Crystal Lens-Cells with Variable Focal Length," *Jpn. J. Appl. Phys.* **18**(9), 1679–1684 (1979).
25. H. Ren, D. W. Fox, B. Wu, and S.-T. Wu, "Liquid crystal lens with large focal length tunability and low operating voltage," *Opt. Express* **15**(18), 11328–11335 (2007).

26. H. Ren, Y.-H. Fan, and S.-T. Wu, "Prism grating using polymer stabilized nematic liquid crystal," *Appl. Phys. Lett.* **82**(19), 3168–3170 (2003).
27. J. Sun, S. Xu, H. Ren, and S.-T. Wu, "Reconfigurable fabrication of scattering-free polymer network liquid crystal prism/grating/lens," *Appl. Phys. Lett.* **102**(16), 161106 (2013).
28. R. Yamaguchi, T. Nose, and S. Sato, "Liquid crystal polarizers with axially symmetrical properties," *Jpn. J. Appl. Phys.* **28**(9), 1730–1731 (1989).
29. Y. Morita, J. E. Stockley, K. M. Johnson, E. Hanelt, and F. Sandmeyer, "Active liquid crystal devices incorporating liquid crystal polymer thin film waveplates," *Jpn. J. Appl. Phys.* **38**(Part 1, No. 1A), 95–100 (1999).
30. S. J. Woltman, G. D. Jay, and G. P. Crawford, "Liquid-crystal materials find a new order in biomedical applications," *Nat. Mater.* **6**(12), 929–938 (2007).
31. S. V. Serak, D. E. Roberts, J.-Y. Hwang, S. R. Nersisyan, N. V. Tabiryan, T. J. Bunning, D. M. Steeves, and B. R. Kimball, "Diffractive waveplate arrays [Invited]," *J. Opt. Soc. Am. B* **34**(5), B56–B63 (2017).
32. S. Ohki, "Dielectric constant and refractive index of lipid bilayers," *J. Theor. Biol.* **19**(1), 97–115 (1968).
33. W. Huang and D. G. Levitt, "Theoretical calculation of the dielectric constant of a bilayer membrane," *Biophys. J.* **17**(2), 111–128 (1977).
34. J. M. Tiffany, "Refractive index of meibomian and other lipids," *Curr. Eye Res.* **5**(11), 887–889 (1986).
35. Y. Cui and R. M. A. Azzam, "Determination of the refractive index and thickness of transparent pellicles by use of the polarization-independent absentee-layer condition," *Appl. Opt.* **35**(25), 5040–5043 (1996).
36. I. H. Malitson, "Interspecimen comparison of the refractive index of fused silica," *J. Opt. Soc. Am.* **55**(10), 1205–1209 (1965).